IEKP-KA/2014-17

Karlsruher Institut für Technologie

Study of Orbitally Excited $B_{(s)}$ Mesons and Evidence for a New $B\pi$ Resonance with the CDF II Detector

Manuel Kambeitz

Zur Erlangung des akademischen Grades eines

Doktors der Naturwissenschaften

von der Fakultät für Physik des
Karlsruher Instituts für Technologie (KIT)

genehmigte

Dissertation

von

Dipl.-Phys. Manuel Kambeitz
aus Karlsruhe

Tag der mündlichen Prüfung:	5. Dezember 2014
Referent:	Prof. Dr. M. Feindt
Korreferent:	Prof. Dr. Th. Müller

Contents

1. Introduction

When particle physicists investigated the substructure of protons in the 1960s, they discovered point-like constituents, today known as quarks and gluons. This discovery made it possible to formulate the Standard Model of particle physics, describing all elementary particles and their fundamental interactions, except gravity, in the 1970s. Bound-quark states, of which mesons are the simplest realization, are described in the Standard Model by quantum chromodynamics (QCD). At the energy scale of these states, QCD faces the problem that its coupling constant is in the order of one, thus making predictions about their properties very complex. Several approaches to this problem have been invented and experimental tests will help to better understand QCD.

To study mesons and their dominating binding interaction, namely the strong interaction described by QCD, the energy spectra of their excitations can be investigated. This approach has been successfully used to study the electromagnetic interaction in great detail on the basis of hydrogen spectroscopy. An analog system to the hydrogen atom are B and B_s mesons, described in chapter 2 of this thesis. Both systems consist of two particles with very different masses.

A frequently used approach to describe mesons is an expansion making use of the large mass of heavy quarks. The heaviest quark forming bound states is the bottom quark, so $B_{(s)}$ mesons provide the best system realized in nature for this approach. However, the production of their excitations is so difficult, that the excitations of D mesons, containing a lighter charm instead of a bottom quark, have been studied in much more detail. Eight excitations of D mesons are known. In contrast, for $B_{(s)}$ mesons only three such states have been observed before the beginning of this thesis. Therefore, further study is in order and new states are expected to be discovered, like the $B(5970)$ state first observed in this thesis.

Many particle-physics experiments are performed at particles accelerators, where particle collisions at high energy allow to study phenomena at very small scales and new particles like excited $B_{(s)}$ mesons can be produced in accordance to the mass-energy equivalence. The data used for this thesis originate from the Tevatron, where protons and antiprotons were collided with a center-of-mass energy of 1.96 GeV. Until the Tevatron was superseded by the LHC as the highest-energy collider, it was the most important device for $B_{(s)}$-meson spectroscopy. The particle collisions have been recorded by the CDF II detector, described in chapter 3. The analysis of the data requires several statistical methods like multivariate analysis and Monte Carlo simulations, which are explained in chapter 4.

This thesis presents an analysis of excited states of B^0, B^+ and B_s^0 mesons, decaying to B mesons while emitting a pion or kaon. They are reconstructed from their decay products and a selection is performed to discard wrongly reconstructed $B_{(s)}$ mesons with the multivariate analysis software NeuroBayes, as described in chapter 5. In the training process, the ${}_s\mathcal{P}lot$ method and measured and simulated data are used. Chapter 6 describes how the properties of excited $B_{(s)}$ are determined by an unbinned maximum likelihood fit to their mass spectra. The systematic uncertainties determined in this analysis are described in chapter 7. The results of this thesis are presented in chapter 8 and a conclusion is given in chapter 9. The results shown in this thesis have been published before in [1].

2. Theoretical Overview

The theoretical framework describing the phenomena analyzed in this work is given by the Standard Model of particle physics (SM), it is discussed in section 2.1. The phenomenology of excited $B_{(s)}$ mesons is shown in section 2.2 and the history of their research is discussed in section 2.3 and 2.4.

2.1. The Standard Model of Particle Physics

The Standard Model [2, 3] is the established theory to describe all known elementary particles and their interactions through the electromagnetic, weak and strong interactions. As it is a theory, it can be used to make predictions about future measurements and observations. The most recent accomplishments of the Standard Model comprise the prediction of the existence of the the top quark and the Higgs boson. Its predictions have been confirmed many times by a wide variety of experimental results. The Standard Model has 19 parameters. They cannot be predicted, but they have to be measured.

2.1.1. Elementary Particles

Particles without a substructure in the Standard Model are called elementary particles. They can be classified into fermions with half-integer spin and bosons with integer spin. Particles carry different types of charges that determine in which interactions they participate.

Fermions

The fermions in the Standard Model with color charge are called quarks, those without color charge are called leptons. There are six types of quarks, half of them carrying electric charge $+2/3\,e$ and the other half carrying the charge $-1/3\,e$. There are six types of leptons, three of them carrying electric charge e and three of them carrying charge 0. Neutral leptons are named neutrinos. There exists an antiparticle for each of the mentioned fermions, having same mass and opposite charge. Only for neutrinos it is currently not proven, whether they can be distinguished from their antiparticle. All mentioned fermions have spin $1/2$.

Bosons

Forces are described in the Standard Model by the exchange of gauge bosons. All of them have spin 1. The chargeless and massless photon mediates the electromagnetic interaction. The bosons of the weak interaction are the W^-, W^+ and Z^0 bosons. They are among the heaviest elementary particles. While W bosons carry electric charge, the Z boson is neutral. The mediators of the strong interaction are the massless gluons. They couple to the color charge and carry this charge as well.

A different type of boson is the Higgs boson. It is associated with the Higgs field, which gives mass to the W and Z bosons. The Higgs boson has zero spin.

Masses of the Elementary Particles

The masses of elementary particles vary over a large range from 0 to 173 GeV/c^2. Quarks can be arranged in three doublets with ascending mass. It turns out that these doublets are well motivated by the weak interaction. Leptons can be arranged in three doublets of a charged lepton and a corresponding neutrino. The doublets are usually referred to as generations. The elementary particles in the Standard Model are shown in Fig. 2.1.

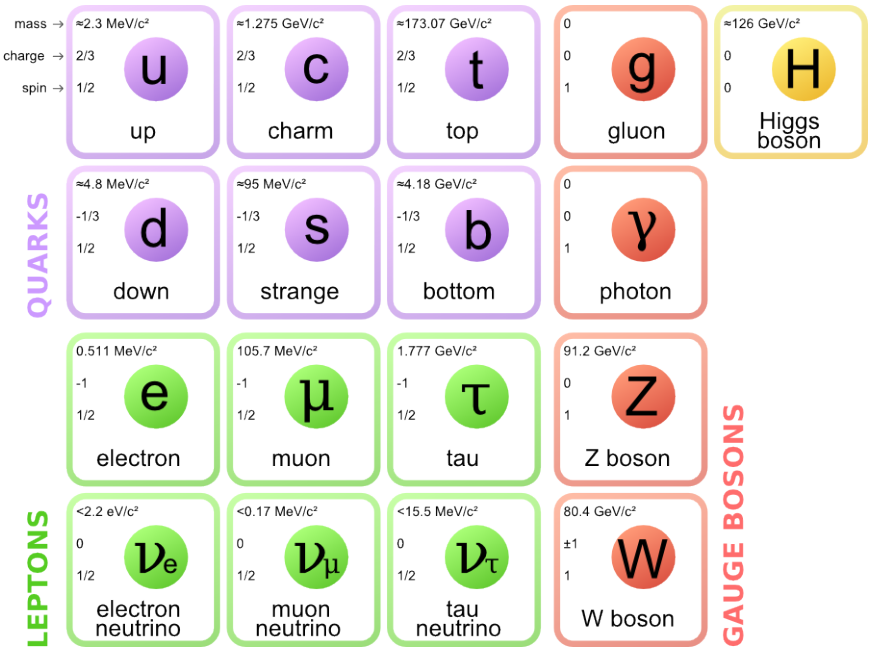

Figure 2.1.: Elementary particles in the Standard Model and their mass, electric charge and spin. The three columns of quarks and leptons correspond to the three generations. [4]

2.1.2. Fundamental Interactions in the Standard Model

The Standard Model describes the three fundamental interactions described in this section. Fundamental means that the interaction cannot be described by another one. In nature there exists a fourth fundamental interaction which is gravity. It is not described by the Standard Model but by the general theory of relativity.

The Strong Interaction

The strong interaction is described quantum chromodynamics (QCD). It is mediated by gluons, which couple to the color charge, so to quarks and gluons. It is the strongest force at nuclear scale and helps forming mesons and baryons. It is the dominant interaction of many decay processes on elementary particle scale.

The color charge can have three different values, often illustrated as the colors red, green and blue. Gluons carry a color and an anti-color at the same time. In terms of group theory, there are nine different gluons. One of them is a singlet which cannot exist in nature. The other gluons belong to an octet, so that in nature eight gluons exist.

The strength of the strong interaction is given by the strong coupling constant α_s. It strongly depends on the energy scale of the process, which is usually given by the momentum transfer squared Q^2 in the considered process. In the first order of perturbation theory the strong coupling constant is given by

$$\alpha_s(Q^2) = \frac{4\pi}{(11 - \frac{2}{3}N_F)\ln(Q^2/\Lambda^2_{\mathrm{QCD}})} \tag{2.1}$$

with the QCD scale Λ_{QCD}. The number of quark flavors having a mass below the scale Q is given by N_F.

The strong interaction forbids the existence of isolated particles with color charge, so only color-neutral objects can exist. They are described in section 2.1.3. This effect is known as confinement. Equation 2.1 shows that at high energies, meaning for quarks or gluons at small distances, the strong interaction becomes weaker, an effect termed asymptotic freedom.

The strong interaction does not discriminate quarks by their flavor. This is particularly evident for up and down quarks because they have similar masses, which is reflected in the concept of strong isospin, where up and down quarks are treated like spin $1/2$ states. Up and anti-down quarks are assigned the z-component of the strong isospin $+1/2$, down and anti-up have $-1/2$. When the properties of an object are mainly determined by the strong interaction, it is subject to the approximate isospin symmetry. This means that its properties do not change when an up (down) quark is exchanged by a down (up) quark. The strong interaction conserves the strong isospin because it cannot transform up to down quarks or vice versa.

The Electromagnetic Interaction

The electromagnetic interaction is carried by the photon, which couples to the electric charge. As the photon is massless and chargeless the electromagnetic interaction has an infinite range. The theory describing the electromagnetic interaction is quantum electrodynamics (QED).

At elementary particle scale it plays a role in decays of mesons and baryons. It also binds the electrons to the nucleus in an atom. Electromagnetism produces a variety of different phenomena on macroscopic scales.

The Weak Interaction

The weak interaction is mediated by the W and Z bosons. While W bosons couple to the weak isospin, the Z boson couples to a linear combination of the weak isospin and the electric charge. The weak isospin is zero for right-handed particles and left-handed antiparticles. This corresponds to maximal parity violation of the weak interaction. Because the mentioned bosons are heavy, the interaction is weak at low energies and has a very short range.

The weak interaction can change the flavor of quarks. Therefore it plays an important role in decays of mesons and baryons which cannot decay via the strong interaction, like B mesons. Those states have relatively long lifetime and so B mesons produced at the Tevatron fly a measurable distance before they decay. This effect is used in this thesis to distinguish B mesons from other particles.

Transitions between quarks from different families are suppressed in the weak interaction. This is described by the Cabibbo-Kobayashi-Maskawa (CKM) mechanism. The CKM matrix is a unitary complex matrix which rotates the quarks carrying charge $-1/3\,e$ from the mass eigenbasis to the flavor eigenbasis, in which transitions are allowed only within a family.

The theoretical framework of the weak interaction is the electro-weak theory, which also describes the electromagnetic interaction.

2.1.3. Composite Particles

Due to confinement, quarks can only exist in color neutral bound states with other quarks, called hadrons. Mesons and baryons are the two established types of hadrons. Mesons consist of a quark with color charge and an antiquark with the corresponding anti-charge forming a color neutral object. Baryons consist of three quarks with three different color charges. This combination is also color neutral. The most familiar baryons are the proton and the neutron.

Mesons

In the first instance, mesons can be characterized by their quark content. For an exact description, their mass is also indicated to distinguish different excitations. Excited states frequently have different names than the ground state. Mesons can be categorized in the following way:

- Light mesons, consisting of up, down or strange quarks,
- D mesons consisting of one charm quark and one lighter quark,
- charmonium states containing two charm quarks,
- B mesons containing one bottom quark and one lighter quark and
- bottomonium states with exactly two bottom quarks.

The first three categories are illustrated in Fig. 2.2. The top quark is so short-lived that it decays before it can form bound states.

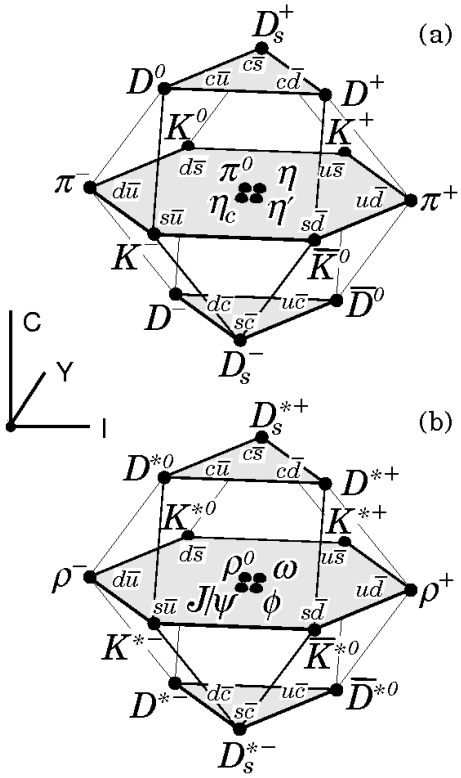

Figure 2.2.: The ground states of pseudoscalar (spin 0) (a) and vector (spin 1) (b) mesons containing light and charm quarks can be arranged with respect to their isospin (I), hypercharge (Y) and charm (C). [2]

2.2. Excitations of $B_{(s)}$ Mesons

Bound states of a bottom quark and a lighter quark are called B^0 mesons (quark content: down-antibottom), B^+ mesons (up-antibottom), B_s^0 mesons (strange-antibottom) and B_c^+ mesons (charm-antibottom). In this thesis, the name of a particle also refers to its antiparticle. The term B meson refers to B^0 and B^+ mesons collectively and $B_{(s)}$ meson refers to B^0, B^+ and B_s^0 mesons.

In the ground state of a B meson, the spins of the two quarks are aligned antiparallel. It has a mass of about 5 279 MeV/c^2. The lowest-energy excitation with the quark spins aligned parallel is named B^* meson. It decays through the electromagnetic interaction to a B meson and a photon. The mass difference to the ground state is about 45 MeV/c^2.

The next higher excitation arises from an orbital angular momentum $L = 1$ between the two quarks in the meson. The mass of the bottom quark is much larger than the QCD scale Λ_{QCD} so the momentum transfer between the constituents inside an B meson is much smaller than the bottom quark mass m_B. In the limit of an infinite bottom-quark mass, this means that the bottom quark is not influenced by the light quark. Corrections due to the finite mass of the bottom quark can be treated as an expansion in $\frac{\Lambda_{\mathrm{QCD}}}{m_B}$.

Consequently, the dynamics of the B meson is dominated by the properties of the light quark, given by the coupling of L with the spin $s_q = 1/2$ of the light quark. The sum of both is the total angular momentum of the light quark

$$j_q = L \oplus s_q, \tag{2.2}$$

which can take the values $j_q = 1/2$ or $j_q = 3/2$. The total angular momentum of the orbitally excited B meson

$$J = j_q \oplus s_b \tag{2.3}$$

is given by the coupling of j_q with the spin $s_b = 1/2$ of the bottom quark. The four possible combinations are referred to as B^{**} states. They are shown in Table 2.1. In the following, B_1 refers to the state with $j_q = 3/2$.

The mass difference of the known B^{**} states to the B ground state is about 450 MeV/c^2 and the mass difference between the B_1^0 and B_2^{*0} states has been measured to be about 20 MeV/c^2 [2]. The theoretical predictions about the masses of the $j_q = 1/2$ states minus the mass of the $j_q = 3/2$ states cover a region from -100 to $+200$ MeV/c^2 [5].

The spectrum of B_s^{**0} mesons shows the same structure. In comparison to B^{**} mesons, the masses of B_s^{**0} mesons are 100 MeV/c^2 higher and the mass splitting between the $j_q = 3/2$ states in only 10 MeV/c^2. They have a much smaller width than the B^{**} states because their decay products are heavier thus reducing the phase space in the decay. The spectra of B and B_s^0 mesons are shown in Fig. 2.3.

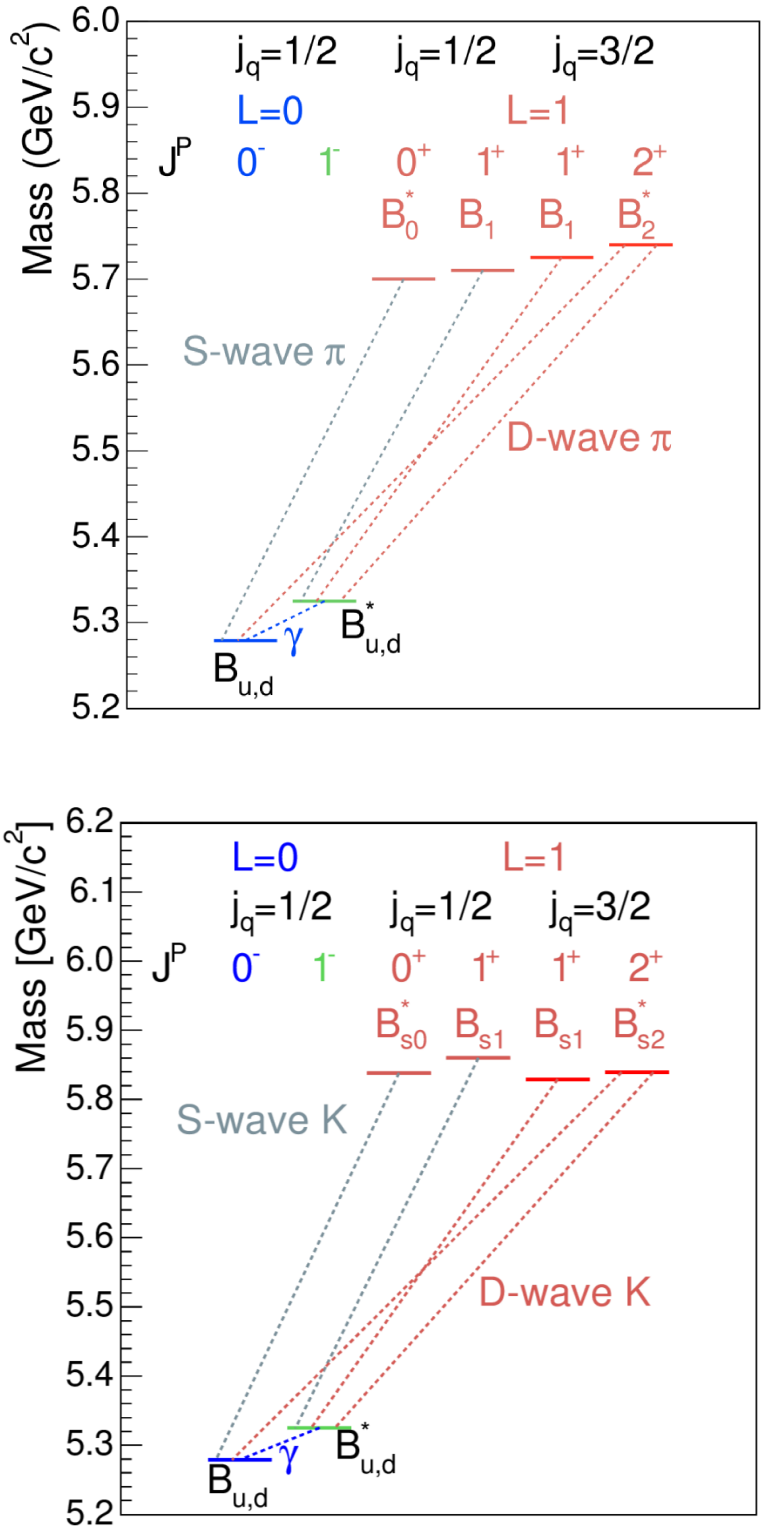

Figure 2.3.: Mass spectra and allowed decays of B [5] and B_s^0 mesons [6].

$B_{(s)}$ mesons decay via the strong interaction to a B or B^* meson and a pion (kaon). The decay $B_s^{**0} \to B_s^0\pi^0$ is suppressed by isospin conservation in the strong interaction, because the initial state has isospin 0 and the final state has isospin 1.

States with $j_q = 3/2$

The bottom quark is, due to its high mass, approximately decoupled from the light quark. For this reason, the total angular momentum of the light quark j_q must be conserved in the decay of a $B_{(s)}^{**}$ meson. Therefore, when a $j_q = 3/2$ state decays and the light quark forms a pion (kaon) together with another quark, the total angular momentum of the pion (kaon) can take the two possible values 1 or 2. This angular momentum must be conserved. It is transformed into an orbital angular momentum l between the pion (kaon) and the B or B^* meson, because pions and kaons have zero intrinsic angular momentum.

The parity of a meson with an intrinsic orbital angular momentum L is

$$P = (-1)^{L+1}. \tag{2.4}$$

So $B_{(s)}^{**}$ mesons have positive parity due to their orbital angular momentum:

$$P^{B_{(s)}^{**}} = (-1)^{1+1} = 1. \tag{2.5}$$

The parity of the final state with two ground states mesons ($L = 0$) with an orbital angular momentum l is given by

$$P_l = (-1) \cdot (-1) \cdot (-1)^l = (-1)^l \tag{2.6}$$

As for parity conservation in the strong interaction and the positive parity of the initial state, P_l has to be positive and so l can take only even-numbered values. Combining this and the previous considerations that for $j_q = 3/2$ states the possible

Table 2.1.: Nomenclature and quantum numbers of B^{**} mesons. The asterisk denotes states with parallel quark spins. [5]

	B_0^*	B_1	B_1	B_2^*
j_q	$\frac{1}{2}$	$\frac{1}{2}$	$\frac{3}{2}$	$\frac{3}{2}$
J^P	0^+	1^+	1^+	2^+
Transition	S-wave	S-wave	D-wave	D-wave
Natural width	broad	broad	narrow	narrow
Decay Modes	$B\pi$	$B^*\pi$	$B^*\pi$	$B\pi$, $B^*\pi$

values of the orbital angular momentum between the pion (kaon) and the B or B^* meson are 1 or 2, this angular momentum has to be 2.

Such a decay is referred to as a D-wave decay. The angular momentum reduces the overlap integral of the reaction and extends the lifetime of the $j_q = 3/2$ states B_1 and B_2^* and makes them narrow. In contrast, no such suppression exists for the broad $j_q = 1/2$ states. This is shown in Table 2.1.

The D-wave decay of the B_1 state, having $J = 1$, is only possible, when the angular momentum $L = 2$ of the final state is balanced by the spin 1 of a B^* meson to match the angular momentum of the initial state. Therefore decays to B^* mesons are allowed while decays to B mesons are not possible.

The B_2^* state has $J = 2$ so that both B and B^* mesons can be produced. Similar arguments determine the S-wave decays of the two other B_s^{**0} states. The possible decays of B and B_s^0 mesons are shown in Fig. 2.3.

B^* mesons decay via the reaction $B^* \to B\gamma$. The energy of the photon is so low that the CDF experiment is not able to detect it. Therefore B^* mesons are reconstructed as B mesons and an amount of energy of 45 MeV is lost in the reconstruction.

Higher Excitations

Besides the $B_{(s)}^*$ state, the orbitally excited $B_{(s)}^{**}$ states are the lowest-energy excitations of $B_{(s)}$ mesons. Theory predicts higher orbital excitations and radially excited states. This is supported by findings for D mesons. All four D^{**} have been observed and three more states at higher energies. This suggests that in the spectra of $B_{(s)}^{**}$ mesons new excitations can be observed.

2.3. Theoretical Predictions

As the bottom quark is not influenced by the light quark in the limit of an infinite bottom quark mass, the bottom quark can be approximated as a static source of a color field. In analogy to the hydrogen atom, which allowed to study QED, $B_{(s)}$ mesons allow to investigate the potential of QCD.

The low influence of the heavy quark on the light quark leads to an approach called Heavy Quark Symmetry. In this symmetry, the bottom quark is exchanged by another heavy quark. Excitations of $B_{(s)}$ mesons are described by Heavy Quark Effective Theory (HQET) [7].

Prediction are mostly made for the masses and less frequently for the widths of the $B_{(s)}^{**}$ states. Predictions made with HQET differ due to different approaches in the treatment of the light quark. Calculations can neglect or include relativistic effects or the spin dependence of the potential between the quarks [8, 9, 10, 11, 12].

The spectroscopy of $B_{(s)}$ meson provides a test for results obtained with lattice-gauge calculations [13, 14] and other approaches besides like potential models [15, 16], Heavy Quark Symmetry [17], chiral theory [18], and QCD strings [19]. Predictions of $B^{**}_{(s)}$ masses and widths are shown in Table 2.2 and 2.3.

The predicted masses cover a range of almost 200 MeV/c^2. This range is up to two orders of magnitude larger than the experimental uncertainty, so measurements can test theory with high precision. Many theory predictions however are made without a statement about the uncertainty of the prediction.

A prediction about the relative branching fraction of the $B^*_{(s)2}$ decaying to either $B\pi(K)$ or $B^*\pi(K)$ can be made. This is done in section 6.2.1.

Table 2.2.: Predicted $B^{**}_{(s)}$ masses. All values are given in MeV/c^2. [1]

Calculation	Ref.	B_1	B_2^*	B_{s1}^0	B_{s2}^{*0}
HQET	[8]	5700	5715		
HQET	[9]	5780 ± 40	5794 ± 40	5886 ± 40	5899 ± 49
HQET	[10]	5623	5637	5718	5732
HQET	[11]	5720	5737	5831	5847
HQET	[12]	5719	5733	5831	5844
Lattice	[13]	5732 ± 33	5772 ± 29	5815 ± 22	5845 ± 21
Lattice	[14]			5892 ± 52	5904 ± 52
Potential	[15]	5699	5704	5805	5815
Potential	[16]	5780	5800	5860	5880
HQS	[17]	5755	5767	5834	5846
Chiral theory	[18]	5774 ± 2	5790 ± 2	5877 ± 3	5893 ± 3
QCD string	[19]	5716	5724		

Table 2.3.: Predicted $B^{**}_{(s)}$ widths. All values are given in MeV/c^2. [1]

Ref.	B_1	B_2^*	B_{s1}^0	B_{s2}^{*0}
[9]		16 ± 5	2.8 ± 1.2	7 ± 3
[10]	20	29		
[16]		27		1.9
[17]	31 – 55	38 – 63	1 – 3	3 – 7
[18]	43 ± 10	57.3 ± 13.5	3.5 ± 1.0	11.3 ± 2.6

2.4. Experimental Status

Before this thesis, the three transitions of the narrow B^{**0} states and two transitions of the narrow B_s^{**0} states had been observed, while exclusively reconstructed B^{**+} mesons and the $B_{s2}^{*0} \to B^{*+}K^-$ transition had not been measured. No higher excitations of $B_{(s)}$ mesons were known.

The first observation of orbitally excited B^{**} mesons was achieved in 1995 at the LEP by DELPHI [20], OPAL [21] and ALEPH [22]. Due to limited statistics the structure of the narrow states could not be resolved until a measurement by DELPHI [23] in 2004. The most recent studies have been performed on B^{**0} mesons in 2007 by DØ [24] and in 2009 by CDF [25] at the Tevatron with higher statistics and a better mass resolution than the LEP experiments. Comparing the results for the mass difference between the two narrow states, CDF and DØ disagree at 2.8σ significance. LHCb showed preliminary results in 2011 [26]. The results are shown in Table 2.4.

Orbital excitations of B_s^{**0} mesons were first observed by OPAL [21] in 1995, where a state with a mass of $5\,853 \pm 15$ MeV/c^2 was found. DELPHI [23] presented a more precise measurement of $5\,852 \pm 5$ MeV/c^2 nine years later and identified it with the B_{s2}^* state. The B_{s1}^0 and B_{s2}^{*0} states were measured by CDF [27] in 2009. The B_{s2}^{*0} state was studied also by DØ [28].

Simultaneously to this thesis, the LHCb experiment performed a measurement [29] of B_s^{**0} mesons and observed the $B_{s2}^{*0} \to B^{*+}K^-$ transition in 2013. The results are shown in Table 2.5.

Table 2.4.: B^{**}-meson properties measured by CDF, DØ and LHCb. All values are given in MeV/c^2. For the LHCb results the third uncertainty originates from the uncertainty of the B and B^*-meson mass. [3]

	CDF [25]	DØ [24]
$m_{B_1^0} - m_{B^+}$	$446.2^{+1.9+1.0}_{-2.1-1.2}$	$441.5 \pm 2.4 \pm 1.3$
$m_{B_2^{*0}} - m_{B_1^0}$	$14.9^{+2.2+1.2}_{-2.5-1.4}$	$26.3 \pm 3.1 \pm 0.9$

	LHCb [26]
$m_{B_1^0}$	$5\,724.1 \pm 1.7 \pm 2.0 \pm 0.5$
$m_{B_1^+}$	$5\,726.3 \pm 1.9 \pm 3.0 \pm 0.5$
$m_{B_2^{*0}}$	$5\,738.6 \pm 1.2 \pm 1.2 \pm 0.3$
$m_{B_2^{*+}}$	$5\,739.0 \pm 3.3 \pm 1.6 \pm 0.3$

Table 2.5.: B_s^{**} masses measured by CDF, DØ and LHCb. All values are given in MeV/c^2. For the LHCb results the third uncertainty originates from the uncertainty of the B and B^*-meson mass. [3]

	CDF [27]	DØ [28]	LHCb [29]
$m_{B_{s1}^0}$	$5\,829.4 \pm 0.7$	-	$5\,828.99 \pm 0.08 \pm 0.13 \pm 0.45$
$m_{B_{s2}^{*0}}$	$5\,839.7 \pm 0.7$	$5\,839.6 \pm 1.1 \pm 0.7$	$5\,839.67 \pm 0.13 \pm 0.17 \pm 0.29$

3. Tevatron and CDF Experiment

This analysis is based on data collected at the Fermi National Accelerator Laboratory (Fermilab) located approximately 50 km west of Chicago. There the particle accelerator Tevatron was operated. It collided protons and antiprotons at an energy of 1.96 TeV. The collisions have been recorded by the Collider Detector at Fermilab (CDF). An aerial photo of the Fermilab is shown in Fig. 3.1.

Figure 3.1.: Aerial view of the Fermilab. The upper ring is the Tevatron, the lower one is the main injector. [30]

3.1. The Tevatron

The Tevatron [3, 31] accelerated and collided protons and antiprotons to an energy of 980 GeV each. It was operated from 1983 to 2011 and accomplished its most famous achievement in 1995 when the top quark was discovered. The performance

of the Tevatron was improved in several steps. The last period of operation between 2001 and 2011 is called Run II. In September 2011 the Tevatron was shut down. Until 2009 it was the particle accelerator with the world's highest center of mass energy. It was then superseded by the LHC at CERN.

3.1.1. Accelerator Complex

Two major challenges when colliding protons and antiprotons in the Tevatron were the production of antiprotons and the acceleration of protons and antiprotons over a huge energy range. This process was performed by a chain of different components shown in Fig. 3.2.

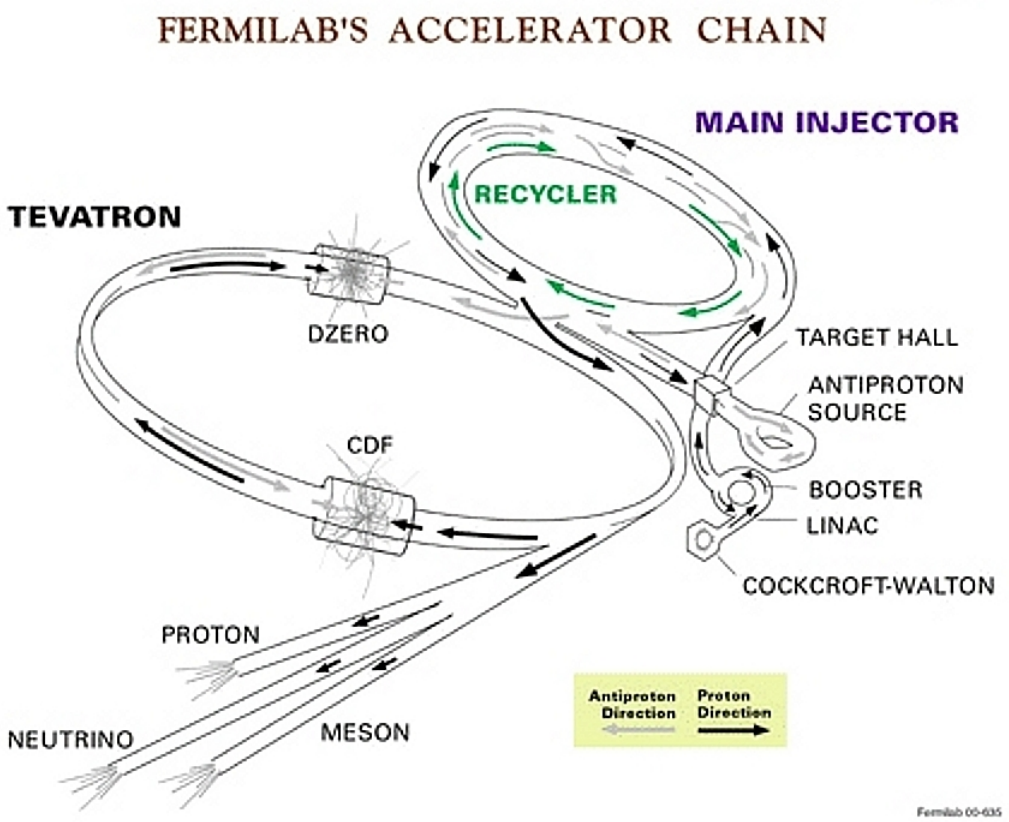

Figure 3.2.: Layout of the accelerator chain at the Fermilab. [32]

To produce protons, negatively charged hydrogen ions were accelerated in a Cockcroft-Walton accelerator and afterwards in a linear accelerator to reach an energy of 400 MeV. The two electrons were stripped off when the ions passed through a carbon foil. The protons were arranged in bunches and accelerated them to an energy of 8 GeV in a synchrotron called Booster.

Afterwards, the protons were accelerated to 120 GeV in the Main Injector. A fraction of the protons was then shot onto a nickel target to produce antiprotons. The latter were separated from other products of the reaction of the protons with the target. The antiprotons were stochastically cooled and stored in the Recycler, located at the same tunnel as the Main Injector. The remaining protons in the Main Injector and the antiprotons in the Recycler were then accelerated to 150 GeV and injected into the Tevatron.

The Tevatron was a synchrotron with a circumference of 6.3 km. High frequency cavities accelerated the protons and antiprotons from 150 GeV to 980 GeV. The particles were kept inside the ring by superconducting dipole magnets. The magnets were cooled to 10 K by liquid helium. Protons and antiprotons flied in opposite directions. Due to their opposite charge, the configuration of the magnetic field allowed them to be accelerated in a single beam pipe.

Inside the Tevatron, 36 bunches of protons and 36 bunches of antiprotons were circulated. The trajectories of the proton and antiproton bunches intersected inside the two particle detectors. The center of mass energy in one collision amounted to 1.96 TeV.

While the Tevatron remained in this configuration, the number of particles in the beams constantly decreased due to particle collisions and beam manipulations. After 15 to 20 hours, the beam was dumped. One period between injection into the Tevatron and dumping of the beam is referred to as a store. The time during one store was used to produce antiprotons.

3.1.2. Luminosity

The luminosity $\mathcal{L}$ is an important characteristic of a particle collider. It determines the event rate $\mathrm{d}N/\mathrm{d}t$ of a process with a given cross section σ

$$\mathcal{L} = \frac{1}{\sigma}\frac{\mathrm{d}N}{\mathrm{d}t} \tag{3.1}$$

and has the dimension $\mathrm{cm}^{-2}\,\mathrm{s}^{-1}$.

At a symmetric proton-antiproton collider the luminosity is determined by the number of bunches n and their circulation frequency f, the number of particles per bunch N_p and $\mathrm{N}_{\bar{p}}$, and the geometry of the beams. Assuming their radial profile to be Gaussian with the average transverse widths σ_x and σ_y, the luminosity reads

$$\mathcal{L} = n \cdot f \cdot \frac{N_p N_{\bar{p}}}{4\pi\sigma_x\sigma_y}. \tag{3.2}$$

The highest luminosity is usually achieved at the beginning of a store and referred to as peak luminosity. The peak luminosity of the Tevatron gradually increased during Run II due to improvements in the operation of the accelerator, as can be seen in Fig. 3.3.

The amount of data, that can be collected by a collider experiment depends both on the luminosity of the collider and the duration of the measurement. It is described by the (time-)integrated luminosity. The integrated luminosity determines the expected number of reactions N with a given cross section σ

$$N = \sigma \cdot \int \mathcal{L}\,\mathrm{d}t \tag{3.3}$$

within a data set. It has the inverse dimension than the cross section, so it can be measured in inverse femtobarn fb^{-1}. Figure 3.4 shows the integrated luminosity delivered by the Tevatron during Run II. In some cases, the Tevatron produced particle collision while the CDF experiment was not ready to record data or data were recorded while important parts of the detector did not work properly. For this reason the data set used in this analysis does not correspond to the full delivered integrated luminosity, but to 9.6 fb^{-1}.

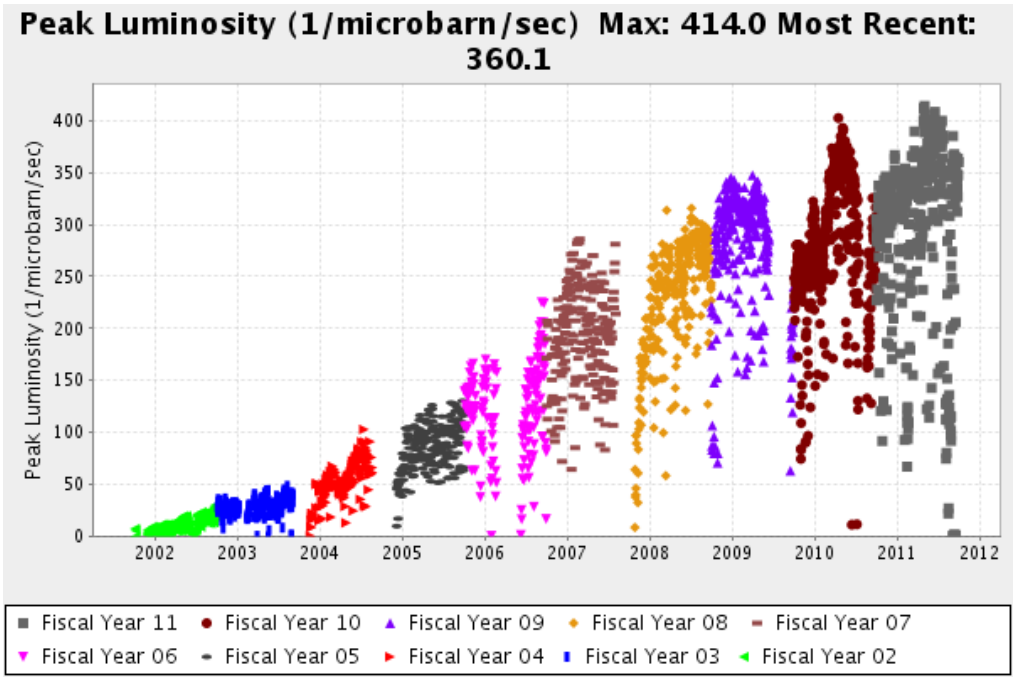

Figure 3.3.: Peak luminosity of the Tevatron during Run II of the CDF experiment [33]. A fiscal years begins on 1 October of the previous calendar year and ends on 30 September.

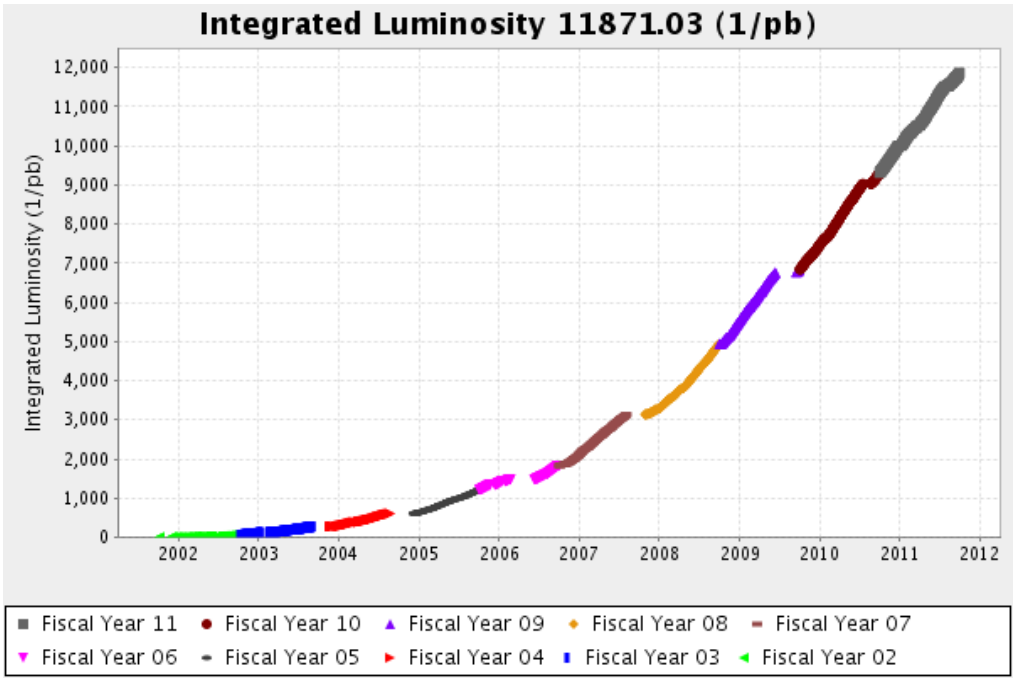

Figure 3.4.: Integrated luminosity delivered by the Tevatron during Run II of the CDF experiment. [34]

3.2. The CDF II Detector

The Collider Detector at Fermilab [3, 31, 35] recorded data of proton-antiproton collisions produced at the Tevatron from 1985 to 2011. The data are analyzed by the CDF collaboration consisting of about 600 physicists in order to study elementary and composed particles and their interactions.

The detector weighted 5 000 tons and was about 12 meters wide in each dimension. Its several subcomponents were arranged in a cylinder-symmetrical way around the collision point. In the following they will be described in detail. Major upgrades of the CDF II detector were performed in 1989 and 2001. An elevation view of the detector, an overview of the inner part and a photo are shown in Fig. 3.5-3.7. The interaction between particles and various detector components are illustrated in Fig. 3.8.

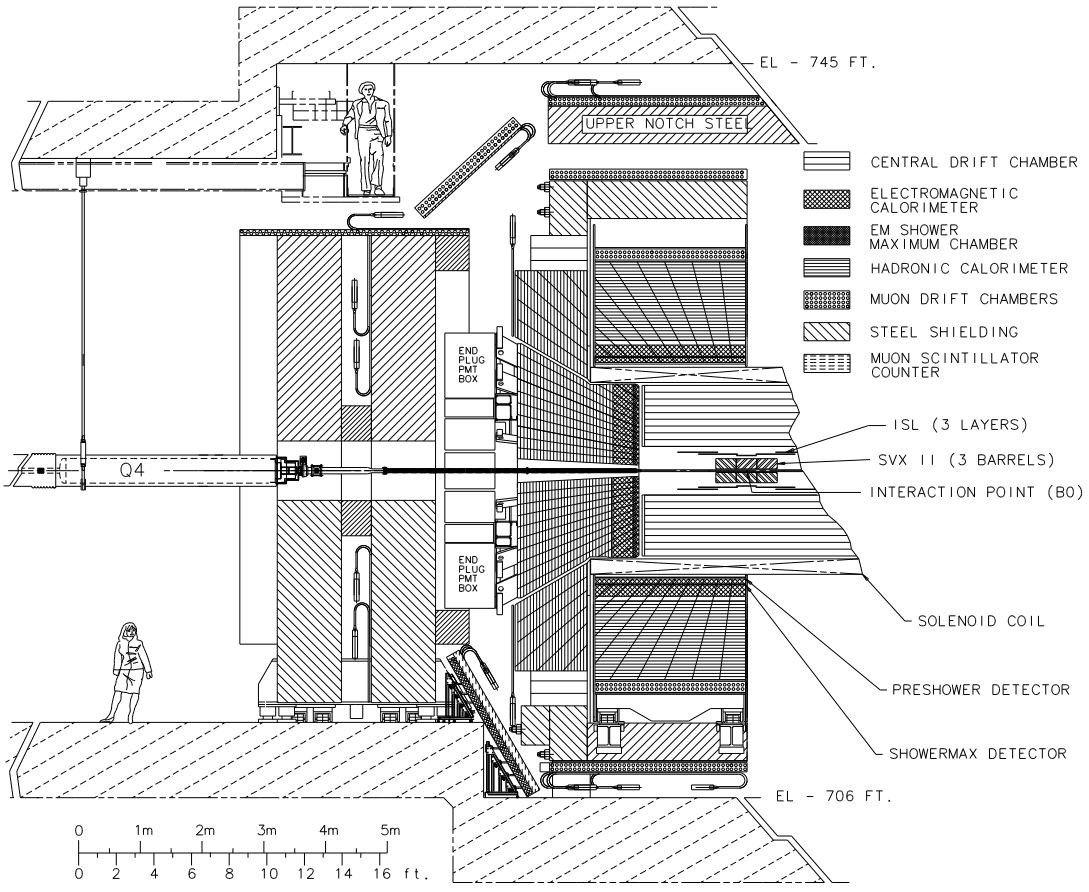

Figure 3.5.: Elevation view of the CDF II detector. [36]

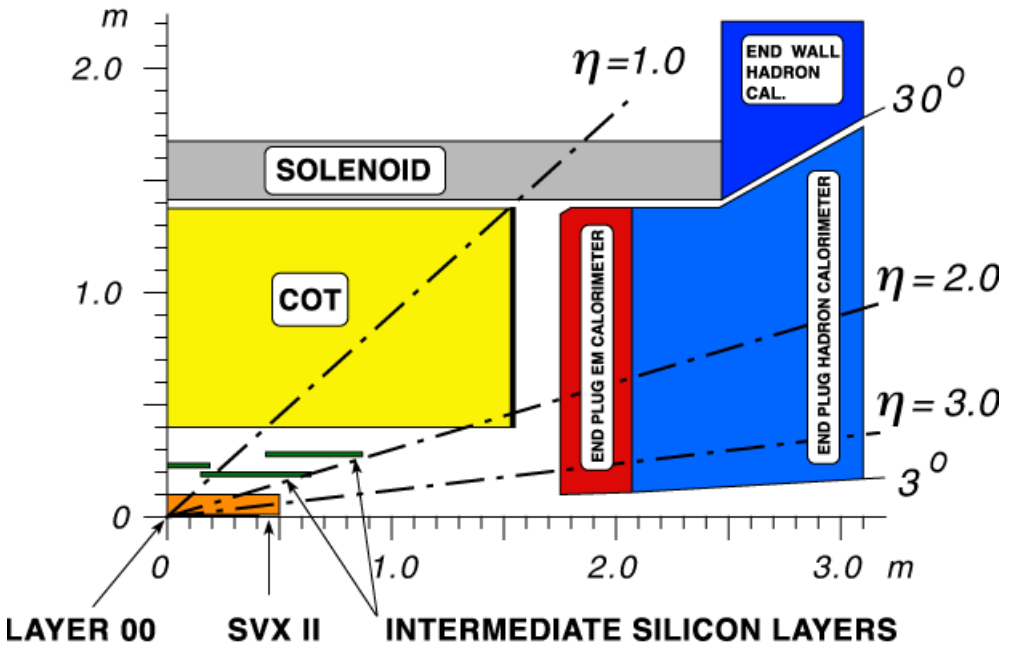

Figure 3.6.: Inner part of the CDF II detector showing the tracking system, the solenoid and the endcap calorimeters. [37]

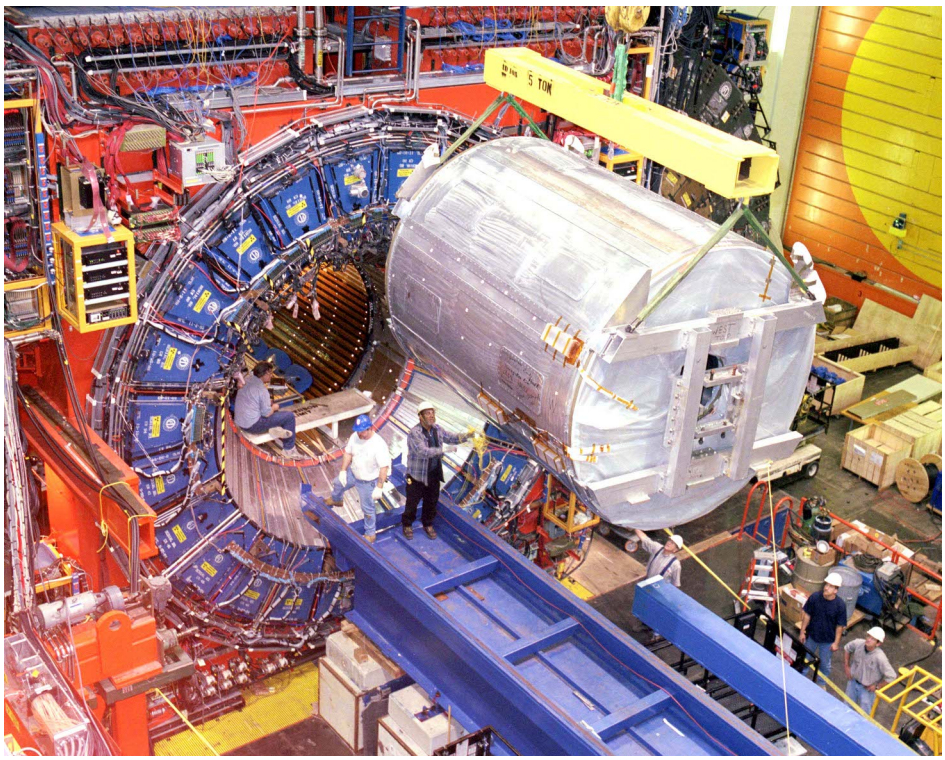

Figure 3.7.: Photo of the CDF II detector during installation of the central drift chamber (COT). [38]

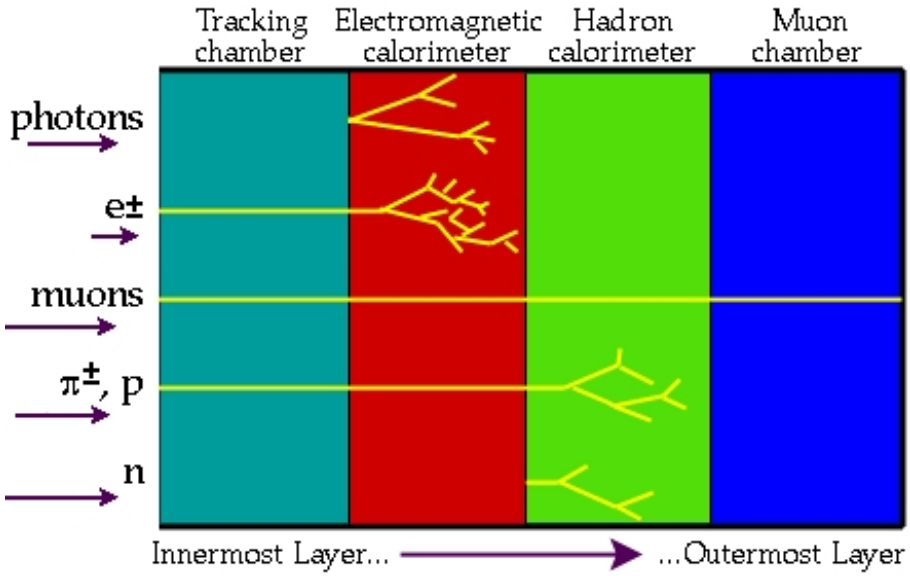

Figure 3.8.: Signatures of several types of particle in a typical collider detector: Charged particles form tracks in the tracking system. Electrons, positrons, photons and hadrons are absorbed in the calorimeters. Muons reach the outermost layer of the detector. [39]

3.2.1. Tracking System

The innermost part of the CDF II detector was the tracking system and detected trajectories of charged particles. A silicon detector and an open-cell drift chamber were located inside a 1.4 T uniform axial magnetic field generated by a superconducting solenoid. The superconductor was cooled by liquid helium. The components of the tracking system and their angular coverage are shown in Fig. 3.6.

The measurement of tracks from particles allows to determine their momentum by measuring the curvature. The curvature comes from the Lorentz force on charged particles inside the magnetic field. Besides the momentum, the sign of the electric charge can be determined. The geometrical measurement allows to detect particles which were produced displaced from the primary vertex. The primary vertex is given by the location of a proton-antiproton reaction.

Silicon Detector

The beam pipe was surrounded by the silicon detector. It had a radius of 28 cm and covered the angular region $|\eta| < 2$. Angles θ with respect to the beam direction are given in terms of the pseudorapidity

$$\eta = -\ln\left(\tan\left(\theta/2\right)\right). \tag{3.4}$$

The silicon detector consisted of several layers of doped silicon with readout circuits. Charged particles flying through a layer created free electrons and holes by ionization, which were observed as a current in the readout electronics.

The innermost layer L00 [40] was added during the upgrade for Run II. It was designed to resist a very strong radiation, which was necessary as it was mounted only 1.4-1.6 cm away from the primary vertex. The following five layers were called Silicon Vertex Detector (SVX II) [41]. The Intermediate Silicon Layer (ISL) [42] provided the outer three layers of silicon detectors.

The system allowed a three-dimensional track finding. When particles originate from the decay of some mother particle, their trajectories start at the same point. Motivated by this, tracks were extrapolated towards the primary vertex and the common origin of two or more tracks, referred to as vertex, can be determined.

Drift Chamber

The Central Outer Tracker (COT) [43] was the drift chamber of the CDF II detector and surrounded the silicon detector. It was located at a radius from 40 to 137 cm from the beam pipe and covered the angular region $|\eta| < 1$. The drift chamber was filled with a mixture of argon and ethane, and measured the ionization of the gas due to traversing charged particles. The signal was read out via a large number of charged wires spanned through the chamber. This allowed to identify the wires which were closest to the traversing particle. The COT consisted of 96 layers. The wires were aligned parallel to the beam, some of them were tilted by two degrees for a three-dimensional measurement. The COT had a transverse momentum resolution of $\sigma(p_T)/p_T^2 \approx 0.1\,\%/(\mathrm{GeV/c})$.

3.2.2. Time of Flight Detector and Particle Identification

The time of flight detector (TOF) [44] was a layer of scintillators and photomultipliers wrapped around the drift chamber at a radius of 138 cm. It measured the flight time of particles from the primary vertex. Using the flight time, length of the trajectory and momentum, the particle could be identified by calculating its mass. The separation power between pions and kaons of the TOF measurement is shown as a solid line in Fig. 3.9.

Also the COT allowed particle identification. Due to ionization, particles flying through the gas inside the drift chamber lost a fraction of their kinetic energy $\mathrm{d}E/\mathrm{d}x$ per travelled distance. The amount of energy depended on the type of particle. This is described by the Bethe-Bloch formula. The deposited energy could be measured from the amplitude of the currents in the wires of the drift chamber.

The separation between pions and kaons from the $\mathrm{d}E/\mathrm{d}x$ measurement is shown in Fig. 3.9 (dashed line). It performed poorly around 1.2 GeV/c and was comple-

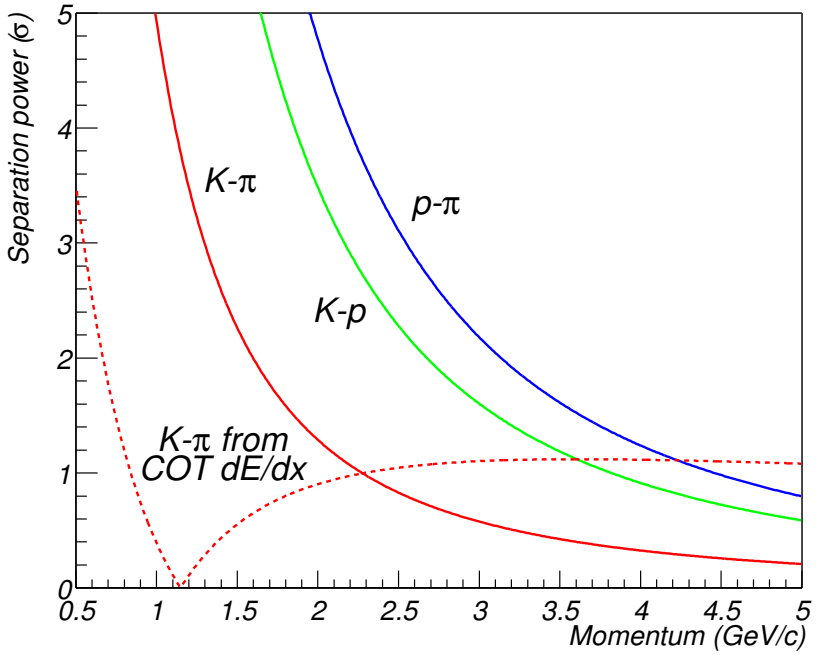

Figure 3.9.: Pairwise separation power between different types of particles by the time of flight measurement (solid lines) and the $\mathrm{d}E/\mathrm{d}x$ measurement (dashed line). [45]

mentary to the TOF. A combination of both measurements by a likelihood ratio was used for particle identification. It offered at least 1.5σ separation between kaons and pions over the whole momentum range.

3.2.3. Calorimeters

The calorimeters of the CDF II detector [46] were used to measure the energy of particles by fully absorbing them. They were optimized for high energy physics and their sensitivity was not sufficient for this analysis. Instead, the energy of particles is calculated from their momentum and the assumed mass.

The calorimeters are therefore only briefly described here. They were located outside the solenoid and covered the large range $|\eta| < 3.6$. The CDF calorimeters consisted of alternating layers of absorber material and scintillators. Electrons, positrons and photons produced showers of secondary particles when interacting with the absorber material of the electromagnetic calorimeter. Hadrons lead to showers in the hadronic calorimeter. The showers produced an amount of light in the scintillators which was proportional to the energy of their primary particle. The light was read out by photomultipliers.

3.2.4. Muon Detectors

Muons have relatively long range in matter and a relatively long lifetime of 2.2 μs. This made them the only charged particles to reach the outermost part of the detector, called muon system [47]. In reverse particles detected in the muon system could be identified as muons. The muon system consisted of drift chambers and scintillators and covered the region $|\eta| < 1.5$.

3.2.5. Trigger System

At the Tevatron, protons and antiprotons were collided every 0.4 μs, that is with a frequency of 2.5 MHz. Storing the information about one collision, referred to as event, required several hundred kB of storage. Recording all produced events would have lead to a data rate of several hundred GB/s so in practice it was not possible.

The interesting processes occurred only in a very small fraction of the collisions. Therefore it was necessary to filter the interesting events out of the data stream coming from the detector in real time. This was the purpose of the trigger system of CDF [48], which is outlined in Fig. 3.10.

Trigger Levels

The trigger system reduced the event rate from 2.5 MHz to several 100 Hz in three levels, named L1, L2 and L3. From level to level the event rate decreased so that the allowed computing complexity increased. Events accepted by the trigger system have been stored on tape for further processing.

The L1 trigger was implemented entirely in hardware and synchronized with the bunch crossing rate. Data were stored in a pipeline while the calculations of the trigger were performed. Events were analyzed by the extremely fast tracker (XFT) [49]. From the information from the COT, it calculated transverse momenta and azimuthal angles of particles for the trigger decision.

L2 comprised both dedicated hardware and programmable processors. It took into account information from the Silicon Vertex Tracker [50] and allowed a more precise calculation of impact parameters.

Level L3 was implemented in software on a Linux PC farm. It confirmed the decisions on L1 and L2 by running similar algorithms with a higher precision.

Trigger Paths

A set of criteria for trigger decisions on all three levels is called a trigger path. The data for this analysis were collected using either the di-muon or the two track trigger paths.

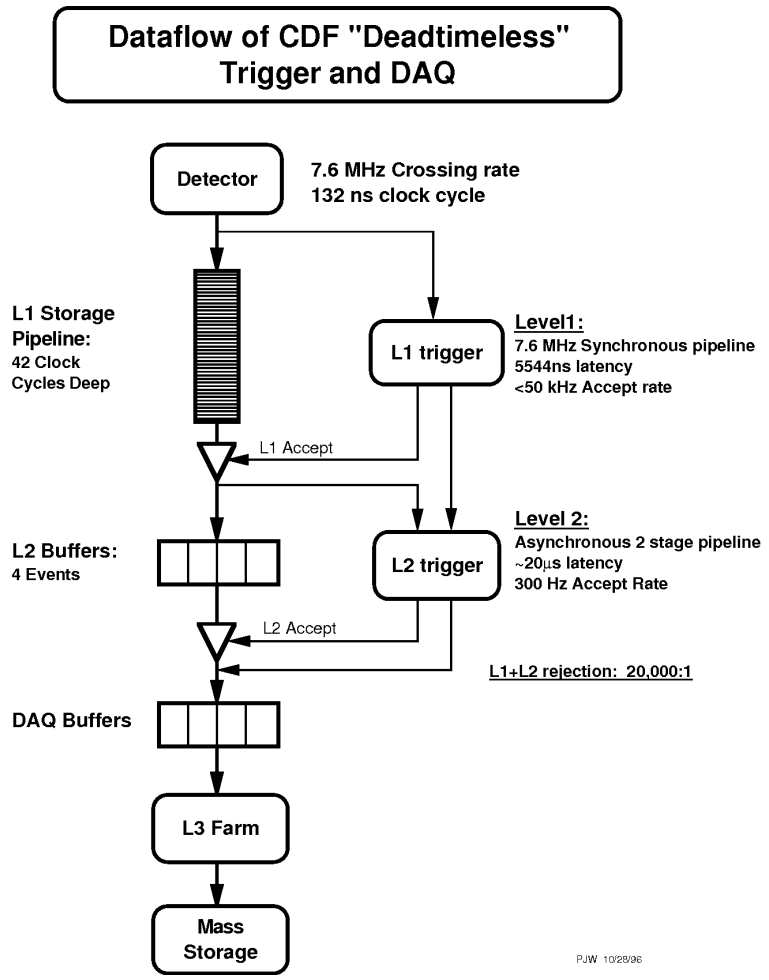

Figure 3.10.: Scheme of the trigger and data acquisition system at CDF. [51]

The di-muon trigger was designed to record events enriched in $J/\psi \rightarrow \mu^+\mu^-$ decays. It required two particles found both in the COT and the muon system with opposite charge. They were required to have a transverse momentum larger than 1.5 or 2.0 GeV/c and an opening angle smaller than 135°. Their invariant mass had to match the known J/ψ-meson mass.

The two track trigger enriched events with long-lived hadrons. It required two tracks displaced from the primary vertex with an impact parameter of 0.12-1 mm and an intersection point displaced at least 0.2 mm. Depending on the luminosity, the sum of their transverse momenta had to exceed 4.5 to 6.5 GeV/c.

4. Analysis Methods and Tools

The stochastic behavior of nature and our measurements needs to be approached with appropriate statistical analysis tools. Nature is stochastic due to its quantum character and our measurement is because of the limited resolution and acceptance of the detector. These effects need to be accurately understood to extract results from the measured data. This chapter describes fit methods and significance determination procedures, which are used to extract quantitative results from the measured data. Afterwards methods to study systematic effects to the measurement process are explained. The last part of the chapter describes the multivariate analysis tools used in this thesis.

4.1. Parameter Estimation and Significance Determination

To extract quantitative results from data, an analytical model for the data has to be constructed. It can comprise theory-motivated components and phenomenological models. The model depends on physical parameters. Measuring the parameters means maximizing the agreement between the model and data by varying the parameters of the model. This process is described in section 4.1.1.

A measured data set consists of a set of N independent measurements $\vec{x}_i$. The model for the data is given in terms of a probability density function (PDF). It has the form $f(\vec{x}_i; \vec{a})$ and depends on the results of one single observation $\vec{x}_i$ and a set of parameters $\vec{a}$. For given parameters $\vec{a}$ the PDF describes the probability for a measurement to yield the parameters $\vec{x}_i$. The condition for normalization

$$\int f(\vec{x}; \vec{a})\, \mathrm{d}\vec{x} = 1 \tag{4.1}$$

has to be fulfilled for each value of $\vec{a}$. Usually not all of the parameters represent physical quantities. Some are nuisance parameter that are not of immediate interest.

Another type of measurement is the significance of a new resonance. It is expressed by stating the probability that the resonance does not exist, even though the data suggest its existence. This measurement is described in section 4.1.3.

4.1.1. Maximum Likelihood Fit

The likelihood function $L(\vec{a})$ depends on the parameters of a statistical model. It is given by the product of the individual probability densities of each observation

$$L(\vec{a}) = \prod_{i=1}^{N} f(\vec{x}_i; \vec{a}). \tag{4.2}$$

Fitting a model to a data set means finding the set of parameters $\hat{\vec{a}}$ that maximizes the value of the likelihood function. It is numerically more convenient to minimize the negative logarithm of the likelihood

$$\mathcal{L}(\vec{a}) = -\ln L(\vec{a}) = -\sum_{i=1}^{N} \ln f(\vec{x}_i; \vec{a}), \tag{4.3}$$

which leads to the same results because the logarithm is monotonic.

Binned Maximum Likelihood Fit

For larger data sets a binned maximum likelihood fit can be performed. The data are then represented by a histogram with J bins. The information about the exact value of each observation in the data is partly lost as only the position of the corresponding bin is used. The advantage is that the PDF does not have to be evaluated for each observation, but only for each bin. This improves the speed of the minimization process.

The expected number of entries in a bin μ_j is given by an approximation of the integral of the PDF over the bin based on the PDF evaluated in the middle of the bin. The likelihood function is given by

$$\mathcal{L}(\vec{a}) = \sum_{j=1}^{J} \ln\left(\frac{\mu_j^{o_j} e^{-\mu_j}}{o_j!}\right) = \sum_{j=1}^{J} o_j \ln \mu_j - \sum_{j=1}^{J} \mu_j - \sum_{j=1}^{J} \ln(o_j!) \tag{4.4}$$

with the observed number of entries in a bin o_j. The last term is constant and can be omitted from the minimization.

4.1.2. The χ^2 Test

The χ^2 test is a statistical method that can be used to evaluate the adequacy of a model to describe a given data set. It compares the expected frequencies and observed frequencies in multiple categories and indicates whether there is a significant difference between them. The categories can be the bins of a histogram. The differences of the counting rates in the histogram o_i and the expected counting

rates e_i are divided by the expected Poisson error and afterwards squared. The sum over all N bins is the χ^2 value given by

$$\chi^2 = \sum_{i=1}^{N} \frac{(o_i - e_i)^2}{e_i}. \tag{4.5}$$

It will follow a χ^2-distribution if the model describes the data. From the χ^2-distribution one can calculate the probability that the model does not describe the data well.

4.1.3. The p-Value

The p-value is used in significance testing. It is given by the probability to observe a signal at least as strong as the observed one, given the hypothesis that no signal exists.

In this analysis a p-value test is used to evaluate the significance of a signal in measured data. Assuming the null hypothesis, a model without the signal is used to generate Toy Monte Carlo samples (cf. section 4.2.2). A quantity indicating the strength of the signal in each sample is then evaluated using the same procedure as was used in measured data. The probability to observe a signal at least as strong as in measured data is calculated. It is given by the fraction of Toy Monte Carlo samples with a higher signal strength in all generated samples. It corresponds to the probability to wrongly claim a signal.

Among particle physicists there are two prominent levels of significance: Evidence for a signal is given by an error probability below 1/370 and an observation may be claimed when the error probability is below 1/1 744 278. Those two levels are called 3σ and 5σ levels. Their error probability corresponds to the integral of a standard normal distribution outside the intervals $[-3, 3]$ or $[-5, 5]$.

4.2. Monte Carlo Simulations

Monte Carlo methods are algorithms that run simulations of probabilistic processes multiple times to obtain the distribution of an unknown stochastic quantity. They are especially useful when an analytic description of all involved processes is very complicated.

This section describes the two fields of application of Monte Carlo simulations in this analysis. The first one is to determine the response of the CDF II detector to the decay of a $B^{**}_{(s)}$ meson. The second one is to estimate the probability that a signal is mimicked by upward fluctuations in a histogram.

4.2.1. Detector Simulation

Several tasks in the analysis of collider experiment data require to simulate the detector response to a given reaction in the collisions.

First the basic physical process is simulated. In this analysis, a $B^{**}_{(s)}$ meson is simulated as the primary particle. Its kinematic properties like transverse momentum are distributed in the same way as determined from measurements of b-hadron kinematic distributions [52, 53]. Other particles originating from the proton-antiproton reaction are not simulated. The decay of the $B^{**}_{(s)}$ meson to a B meson and a pion (kaon) and the subsequent decay of the B meson into several pions, kaons or muons in the considered B-meson decay modes is then calculated using EvtGen [54]. So the kinematics of the particles entering the detector are known. Input for EvtGen are decay tables defining properties of the possible decays of each particle. The used decay tables are shown in appendix A.

A simulation of the full CDF II detector is run with the GEANT software package [55]. Using a geometrical model, it calculates the interaction with the detector material, the reaction of the readout components and the signals finally generated by the detector. The trigger criteria are applied to the simulated detector output and all offline reconstruction algorithms are applied to the resulting data.

This finally results in a data set comprising the same quantities as measured data and similarly distributed as data. The data set includes the influence of the detection process, has the same format as measured data and contains additional information about the generated true values.

Monte Carlo simulations with a Flat Mass Distribution

In the Monte Carlo simulations for this analysis, the mass of the primary $B^{**}_{(s)}$ particle was manipulated in a particular way. For each generated $B^{**}_{(s)}$ particle its mass was randomly chosen within a relatively wide interval with a probability density constant in mass. The mass range is given by [5.42,6.00] GeV/c^2 for B^{**} mesons and by [5.77,5.90] GeV/c^2 for B^{**0}_s mesons. The lower bound of this range is given by the sum of the masses of the daughter particles, because $B^{**}_{(s)}$ mesons with a lower mass would not be able to decay in the specified decay mode. The upper bound was chosen so that the $B^{**}_{(s)}$-meson signal is located approximately in the middle of the mass interval.

This procedure has several benefits for this analysis. The simulations are used in the training of the multivariate selection. If they were generated with the $B^{**}_{(s)}$ mass peaking at their nominal mass, this mass could be learned by the classifier from kinematic observables in the training. Events with these masses would be more likely to be accepted as signal by the classifier so that the signal strength would be biased to higher yields. This is avoided by having a flat mass distribution in the simulation.

Simulating primary particles with a higher mass reflects the properties of higher excitations of B mesons, so that the selection is also suited to discover new excited B-meson states. A flat-mass Monte Carlo finally allows to determine the relative acceptance of the selection depending on the $B^{**}_{(s)}$-meson mass.

4.2.2. Toy Monte Carlo Studies

The measurements in this analysis result from either the fit of a complicated model to measured data or an algorithm to determine the significance of a signal. Both methods introduce possible systematic errors that cannot be determined from the model or the algorithm itself. Instead Toy Monte Carlo studies can be performed to check for possible systematic errors.

In such studies the measured data set is replaced by a randomized data set. A possible way to obtain such a data set is to generate random events with properties distributed in accordance with the model which is used to describe the measured data. As a set of parameters of the model, the parameters obtained from a fit to data can be used.

An ensemble of many toy data sets with different random seeds is generated. The measurement procedure is applied to each of the data sets and the distribution of the measured quantities are studied. It can be tested whether the statistical uncertainty is correctly estimated by the measurement and whether the measurement is biased in any of the measured quantities. Toy studies are also used to calibrate the method for determination of the significance by estimating the probability for a statistical upward fluctuation.

4.3. Multivariate Analysis

Multivariate analysis refers to techniques taking into account several variables of a given problem at the same time. Often the purpose is to predict the probability for the positive outcome of an experiment or to estimate the value of a continuous quantity.

In high energy physics, multivariate methods are frequently used because recorded events contain the information about multiple particles and for each particle several observables can be considered. Each observable carries a part of the available information, so the full available knowledge can only be obtained by considering and combining many observables.

This analysis relies on multivariate classification. Classification means that there exist two classes and each event belong to either of them. In this analysis, these classes are referred to as signal and background. On a part of the data set the assignment to the class is not known but shall be inferred by the multivariate algorithm. The assignment usually has an uncertainty so that a probability to

belong to one of the classes is indicated. Classifying an event can be mathematically expressed as a function f relating an n-dimensional vector of observables to a one-dimensional real number:

$$f : \mathbb{R}^n \to \mathbb{R}. \tag{4.6}$$

4.3.1. NeuroBayes

NeuroBayes [56] is a software package for multivariate analysis. It is trained using historic data or simulations. The training is based on a sophisticated preprocessing of the data and an artificial neural network. The output of NeuroBayes can be interpreted as a Bayesian posteriori signal probability when one is added to the NeuroBayes output and the result is divided by two. This can be concluded from Fig. 4.1, where the purity, defined as the ratio of signal, is plotted over the NeuroBayes output. The purity is statistically in good agreement with the diagonal line in the plot. This means that for each bin the signal probability in data corresponds to the transformed NeuroBayes output.

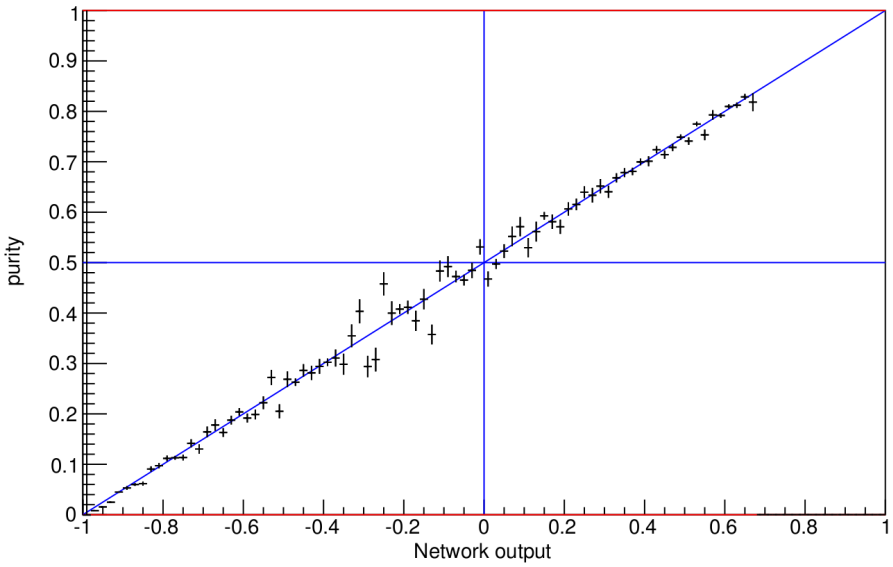

Figure 4.1.: Purity plotted against NeuroBayes output for an exemplary training.

Preprocessing

In the first step of a NeuroBayes training each variable is preprocessed individually to minimize the effect of statistical fluctuations. A histogram with 100 bins of variable bin widths is constructed in a way that each bin contains the same number of events. The histograms of signal and background are shown in Fig. 4.2 for an exemplary observable.

In each bin the purity is calculated and plotted. The dependence of the purity on the observable is modelled by a spline fit, which is shown in Fig. 4.3. The fit levels out statistical fluctuations of the purity. For categorical variables similar preprocessing algorithms are used. The range of values of the spline function is transformed to a standard normal distribution. The transformed values of all observables are decorrelated using their covariance matrix.

The preprocessing achieves a very good exploitation of the information in the individual variables taking into account their linear correlations. The neural network can only improve the classification power by taking into account non-linear correlations between the inputs. It introduces many additional parameters to the classifier and thereby introduces a systematic uncertainty. As the improvement due to the neural network in this analysis was found to be small, it was switched off in the NeuroBayes trainings. In this case all decorrelated observables are combined to a single output quantity.

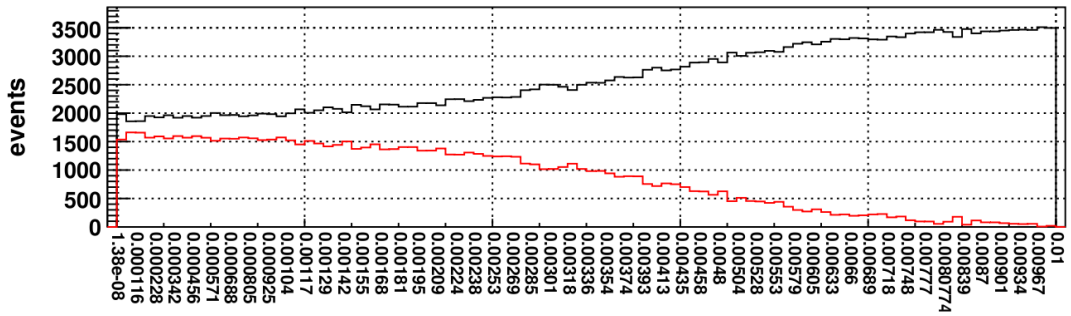

Figure 4.2.: Histogram of a signal observable with variable bin width produced by NeuroBayes. The red histogram corresponds to signal and the black one to background.

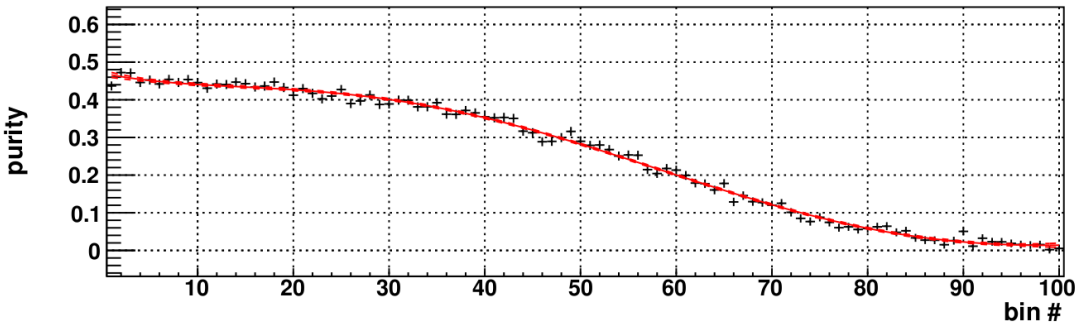

Figure 4.3.: Spline fit to the purity calculated from the histogram in Fig. 4.2.

Training with Weights

NeuroBayes supports the application of individual weights for each event in the training process. Weights represent the importance of an event in the training. An application of weights in trainings are boost trainings where events which are difficult to classify are given a higher weight. NeuroBayes can also handle negative weights, which is important as in this analysis ${}_s\mathcal{P}lot$ weights are used. They are explained in section 4.3.2.

4.3.2. ${}_s\mathcal{P}lot$ Method

The ${}_s\mathcal{P}lot$ [57] method is a tool to statistically separate signal and background in a data set where the true assignment is not known. The sideband subtraction will be explained as an example. Afterwards the details of the ${}_s\mathcal{P}lot$ algorithm will be described.

Sideband Subtraction

In high energy physics analyses often pure signal samples are needed. They can be obtained from Monte Carlo simulations. However simulations do not describe the detector and the physical process perfectly and are very likely to describe wrongly or miss several processes that exist in the real detector. A pure signal sample of measured data is usually not available because there are background processes which cannot be entirely removed from the signal sample.

But there are methods to statistically subtract the background from a sample. This means that histograms resembling the pure signal distribution of observables can be plotted. One method is called background subtraction. When considering the mass spectrum of a resonance like in Fig. 4.4, a signal region containing both signal and background, and a background region containing only background events can be defined. From a fit to the spectrum the yield of background events in the signal region can be determined.

The assumption is made that for background events the histograms of observables have the same shape in the sidebands and in the signal region within statistical fluctuations. The motivation for this lies in the assumption that background processes have little dependence on the reconstructed mass. When histograms of observables are drawn for the signal region the amount of background in each bin can be estimated from the corresponding sideband histogram. The amount is subtracted and the histogram for signal remains. This procedure is equivalent to adding signal histogram with weight one and sideband histograms with a defined constant negative weight.

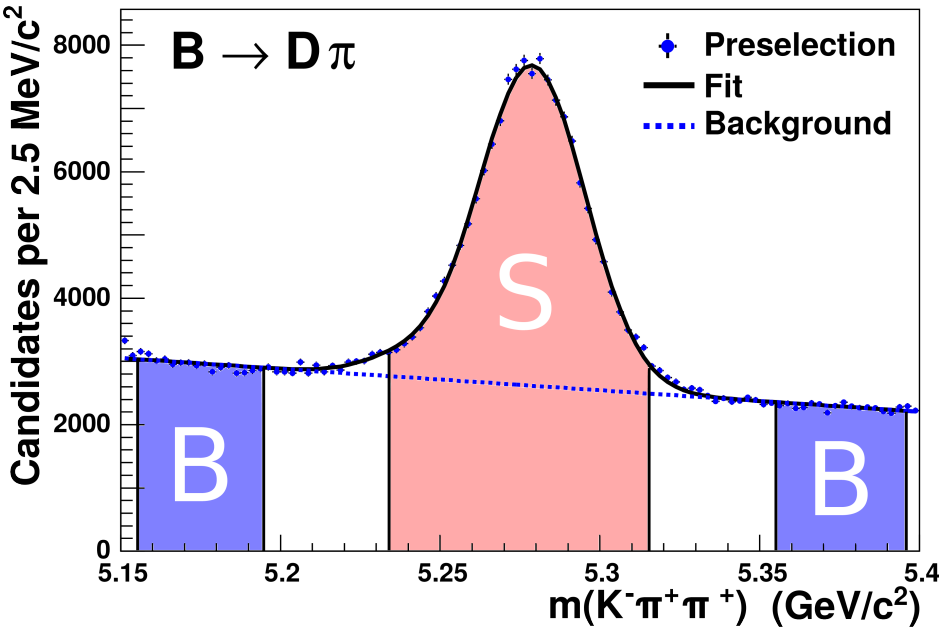

Figure 4.4.: Mass spectrum of B-meson candidates and fit of the sum of signal and background PDF. The signal region is indicated by S, the sideband region by B.

${}_s\mathcal{P}lot$ Method

While a sideband subtraction uses only two different weighs, the ${}_s\mathcal{P}lot$ method refines this principle to continuously valued weights. The weights are calculated from the signal and background PDF $f_1(y)$ and $f_2(y)$ from a fit to data like in Fig. 4.4 and the corresponding yields N_1 and N_2. The ${}_s\mathcal{P}lot$ weight for an event e is given by

$$ {}_sP_n(y_e) = \frac{\sum_{j=1}^{2} \mathbf{V}_{nj} f_j(y_e)}{\sum_{k=1}^{2} N_k f_k(y_e)} \tag{4.7} $$

where j, k and n correspond to either signal or background. The inverse matrix of $\mathbf{V}_{nj}$ is given by

$$ \mathbf{V}^{-1}_{nj} = \sum_{e=1}^{N} \frac{f_n(y_e) f_j(y_e)}{(\sum_{k=1}^{2} N_k f_k(y_e))^2}. \tag{4.8} $$

For each event the sum of the signal and background weight is equal to one. The sum over all signal (background) weights is equal to the signal (background) yield.

The distributions of signal observables are obtained by weighting the data set with the signal weight. When using a multivariate classifier each event enters the training twice. First as signal weighted with the signal ${}_s\mathcal{P}lot$ weight and second as background with the background ${}_s\mathcal{P}lot$ weight.

5. Reconstruction and Selection

The data recorded by the CDF experiment are provided for analysis in a form which comprises all detected particles in an event. For this analysis, the interesting final state particles are pions, kaons and muons. In the reconstruction, sets of these particles are combined to form candidates and for each candidate the properties of the primary excited B meson are inferred. Some candidates do not correspond to real excited B mesons, but originate from background processes. The background candidates need to be rejected. This is done in the selection.

This chapter includes the description of the B^{**}-meson reconstruction and selection. In this analysis, B^{**}-meson candidates are per se candidates for any $B\pi$ resonance like the $B(5970)$ state, which was first observed and studied in this analysis. The reconstruction and selection was, however, performed only with regard to the B^{**} states and not to any higher excitation, so the term B^{**} meson is used in this chapter, but it implies any $B\pi$ resonance.

5.1. Data Set and Reconstruction

The events recorded by the CDF II detector were selected by either the di-muon or the two track trigger described in section 3.2.5.

In the offline reconstruction process, tracks found in the detector are refit using a pion, kaon or muon mass hypothesis to take into account differences in multiple scattering and different energy loss through ionization. The charge of a final state particle is determined from the curvature of the corresponding track. The charge of other particles is determined from the sum of the charge of their daughter particles.

Intermediate $K^*(892)$, K^0_S, D and J/ψ resonances are reconstructed by combining two or three tracks in the patterns

$$\begin{array}{lcl} J/\psi & \to & \mu^+\mu^-, \\ \overline{D}^0 & \to & K^+\pi^-, \\ D^- & \to & K^+\pi^-\pi^-, \\ K^*(892)^0 & \to & K^+\pi^- \text{ and} \\ K^0_S & \to & \pi^+\pi^-. \end{array}$$

The tracks are constrained to originate from the same space point and the reconstructed masses of the resonances are constrained to their known values [2].

B-meson candidates are formed from tracks and intermediate resonances in the seven decay modes

$B^+ \rightarrow J/\psi\, K^+$,
$B^+ \rightarrow \overline{D}^0\pi^+$,
$B^+ \rightarrow \overline{D}^0\pi^+\pi^+\pi^-$,
$B^0 \rightarrow J/\psi\, K^*(892)^0$,
$B^0 \rightarrow J/\psi\, K^0_S$,
$B^0 \rightarrow D^-\pi^+$ and
$B^0 \rightarrow D^-\pi^+\pi^-\pi^+$.

$B^{**}_{(s)}$-meson candidates are finally formed from a B-meson candidate and an additional track in the three combinations

$B^{**0} \rightarrow B^+\pi^-$,
$B^{**+} \rightarrow B^0\pi^+$ and
$B^{**0}_s \rightarrow B^+K^-$.

$B^{**}_{(s)}$-meson decays including an intermediate B^* meson are only partially reconstructed because the photon from the decay $B^* \rightarrow B\gamma$ is too low in energy to be recorded by the CDF II detector. In this case the $B^{**}_{(s)}$ mass is lowered by about 45 MeV/c^2. This effect is taken into account in the fit model.

Selection Variables

For each reconstructed $B^{**}_{(s)}$-meson candidate, several observables are calculated and stored for final state particles, intermediate resonances and the $B^{**}_{(s)}$-meson candidate. They are used in the selection process.

- The transverse momentum p_T is the component of the particle momentum orthogonal to the beam axis.
- The reconstructed mass m is calculated for intermediate resonances and the $B^{**}_{(s)}$ meson from the magnitude of the sum of the four-momenta of their daughter particles. The distribution of the reconstructed mass has a non-zero width due to the detector resolution and the natural width of the particle.
- The impact parameter d_0 is given by the distance of the extrapolated helix of a track to the primary vertex.
- The signed impact parameter $d_0^{\pm}$ includes the direction with respect to the mother particle. Its sign is given by the sign of the scalar product of $\vec{d_0}$ and the momentum of the mother particle.
- The significance of the transverse decay length $L_{xy}/\sigma(L_{xy})$ is used to require a minimal flight length of a particle with a relatively long lifetime. It is given by the measured flight length of a particle orthogonal to the beam axis divided by the estimated error of this measurement.

- The transverse decay length with respect to the parent L_{xy}^{parent} is the transverse flight length measured from the decay vertex of the mother particle.

- The fit quality of the three-dimensional vertex fit χ^2_{3D} is calculated for intermediate resonances and the $B^{**}_{(s)}$-meson candidate. In principle all daughter tracks have to originate from a common vertex. In practice this is not exactly true, because the measured tracks of particles have uncertainties. The most probable intersection point is derived from the vertex fit and the χ^2-value gives the fit quality.

- The helicity angle ϕ is the angle between the directions of the particle and the grandparent particle measured in the rest frame of the mother particle.

- The quantity $\alpha_{\text{cms}}^{\text{parent}}$ is given by the angle between the momentum of a particle in the rest frame of its mother particle and the momentum of the mother particle in the lab frame.

- The pull^{ToF} of a particle is given by the difference between the expected flight time, given a mass hypothesis, and the measured flight time, divided by the uncertainty of the measured flight time.

- The combination of all available particle identification information is given by the likelihood $\mathcal{L}^{\text{PID}}$.

5.2. B-Candidate Selection

In the first part of the selection process, wrong B-meson candidates are rejected. The B-meson selection, performed before the $B^{**}_{(s)}$-meson selection, is performed using only data and no simulations. The selection of B-mesons has been finalized already as part of [3] and is explained here for sake of completeness.

5.2.1. Preselection

The purpose of the preselection is to reduce the amount of reconstructed data by removing wrong B-meson candidates until a multivariate analysis is technically possible. It needs to be both fast enough to process several hundred GB of data and very efficient in removing only a very small fraction of true B-meson candidates.

The preselection is performed individually for each considered B-meson decay chain. Using the ${}_s\mathcal{P}lot$ method the distributions of observables of final state particles, intermediate resonances and the B-meson candidates of signal and background events are compared. For each observable, the distribution is searched for regions containing mostly background and very few signal. These regions are then removed

Table 5.1.: Cuts applied for the preselection of B^+ mesons. [3]

		$B^+ \to \overline{D}^0\pi^+$	$B^+ \to \overline{D}^0\pi^+\pi^+\pi^-$	$B^+ \to J/\psi K^+$
B-meson χ^2_{3D}		< 50	< 50	< 70
B-meson d_0	(cm)	< 0.01	< 0.007	< 0.01
B-meson $L_{xy}/\sigma(L_{xy})$		> 5	> 12	> 4
B-meson p_T	(GeV/c)	> 5	-	-
K from B p_T	(GeV/c)	-	-	> 0.8
π(s) from B p_T	(GeV/c)	> 0.8	> 0.4	-
$m(3\pi)$ from B	(GeV/c^2)	-	< 2.8	-
$m(D)$	(GeV/c^2)	1.81 - 1.91	1.81 - 1.91	-
D-meson d_0	(cm)	> 0.003	> 0.003	-
D-meson $L_{xy}/\sigma(L_{xy})$		-	> 6	-
D-meson p_T	(GeV/c)	-	> 2	-
π from D p_T	(GeV/c)	> 0.4	> 0.4	-
K from D p_T	(GeV/c)	-	> 0.5	-

from the data by defining threshold values for the observables and removing the events which do not pass the threshold. This procedure is referred to as a cut.

For each decay chain cuts on several observables are defined. The exact values are listed in Table 5.1 and 5.2. The cut values were chosen so that the remaining data set of each decay chain amounts to around one GB of data.

Also the correct sign of the charge of a particle is required for the signal selection. Combinations with wrong charge are also stored as they are useful for additional studies. An exception is given for the decay $B^{**+} \to B^0\pi^+$. The B^0 meson can oscillate to a $\overline{B}^0$ meson so that a valid combination is not only given by $\overline{B}^0\pi^-$, but also by $\overline{B}^0\pi^+$ combinations.

The spectrum of the reconstructed B-meson candidate mass before the preselection is shown in Fig. 5.1. The B-meson signal peak is nearly not visible over the large amount of background. The spectrum after the application of the preselection cuts is shown in Fig. 5.2.

5.2.2. NeuroBayes Selection

True B-meson candidates are distinguished from wrong B-meson candidates by using the NeuroBayes software package. A separate instance of NeuroBayes is used for each of the seven considered B-meson decay chains. Plots and tables in this section describe the NeuroBayes instance trained for the $B^+ \to \overline{D}^0\pi^+$ decay chain. The six other instances were trained in a similar way. The B-meson mass fits are shown in appendix B and the training variables are listed in C.

The training of the NeuroBayes classifiers is performed using only measured data and no simulations. This is possible by using the ${}_s\mathcal{P}lot$ method described in

Table 5.2.: Cuts applied for the preselection of B^0 mesons. [3]

		$B^0 \to D^-\pi^+$	$B^0 \to D^-\pi^+\pi^+\pi^-$
B-meson χ^2_{3D}		< 50	< 50
B-meson d_0	(cm)	< 0.01	< 0.007
B-meson $L_{xy}/\sigma(L_{xy})$		> 5	> 14
B-meson p_T	(GeV/c)	> 5	> 6
π(s) from B B p_T	(GeV/c)	> 0.9	> 0.4
$m(3\pi)$ from B	(GeV/c^2)	-	< 2.2
$m(D)$	(GeV/c^2)	1.81 - 1.91	1.81 - 1.91
D-meson d_0	(cm)	> 0.003	> 0.003
D-meson $L_{xy}/\sigma(L_{xy})$		> 2	-
D-meson p_T	(GeV/c)	-	> 2
πs from D p_T	(GeV/c)	-	> 0.4
K from D p_T	(GeV/c)	-	> 0.7

		$B^0 \to J/\psi K^{*0}$	$B^0 \to J/\psi K^0_s$
B-meson χ^2_{3D}		< 70	< 70
B-meson d_0	(cm)	< 0.01	< 0.01
B-meson $L_{xy}/\sigma(L_{xy})$		> 4	> 1
B-meson p_T	(GeV/c)	> 3.5	> 5
J/ψ $L_{xy}/\sigma(L_{xy})$		-	> 0
K_s-meson p_T	(GeV/c)	-	> 1
K^*-meson p_T	(GeV/c)	> 1.3	-
π from K_s meson p_T	(GeV/c)	-	> 0.5
K from K^* meson p_T	(GeV/c)	> 0.5	-

section 4.3. The spectrum of B-meson candidate invariant mass $m(B)$ is fit with a phenomenological model describing the shape of the signal peak and the smooth background. For the signal component, the best fitting choice from one or two Gaussian functions or a Breit-Wigner is used. The background component is a first order polynomial or an exponential function. The fit for the $B^+ \to \overline{D}^0\pi^+$ decay chain is shown in Fig. 5.2.

From the fit PDFs and their normalization, an individual ${}_s\mathcal{P}lot$ weight is calculated for each candidate. The candidates and weights are given to NeuroBayes and a training is performed. The variables entering the training are shown in Table 5.3, their correlation matrix is shown in Fig. 5.3.

The distribution of the NeuroBayes output is shown in Fig. 5.4. A cut is performed and events with an output below -0.8 are discarded in the following process. The selected data set is shown in Fig. 5.2. Of signal events 97 % are retained, while 74 % of the background events are removed.

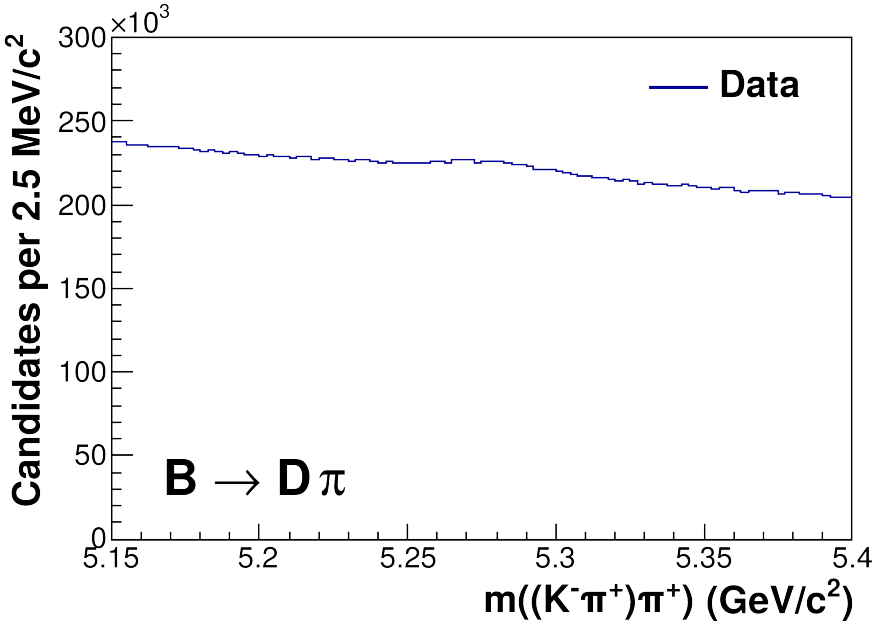

Figure 5.1.: Spectrum of $m(B)$ in the decay chain $B^+ \to \overline{D}^0\pi^+$ before application of the preselection.

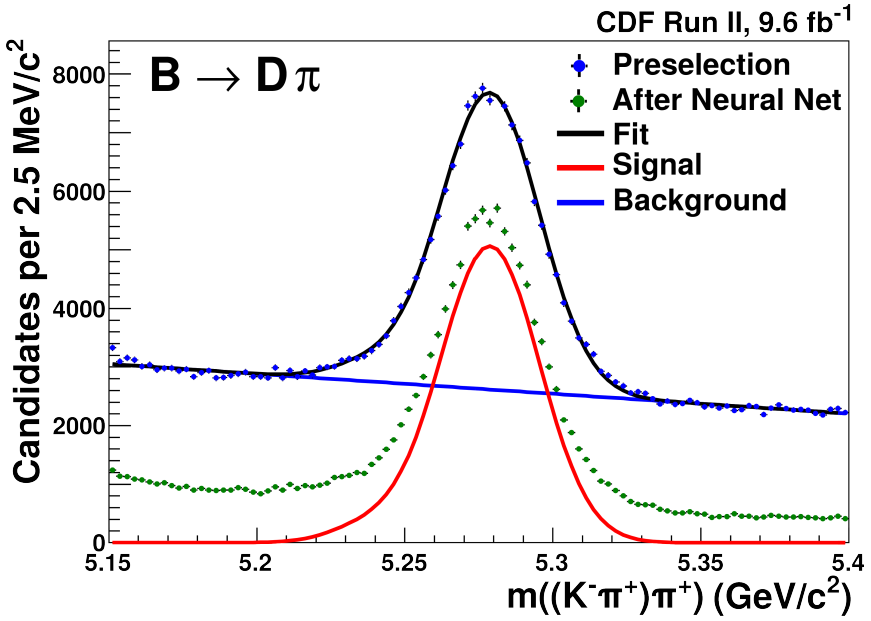

Figure 5.2.: Spectrum of $m(B)$ in the decay chain $B^+ \to \overline{D}^0\pi^+$ after application of the preselection (blue data points) together with the fit with a linear background and the sum of two Gaussians functions. One Gaussians represents the actual signal and other one represents the Cabibbo suppressed decay to $\overline{D}^0K^+$. Data after the NeuroBayes selection are shown as green data points.

Table 5.3.: Inputs used in the NeuroBayes training for the selection of B meson-candidates in the $B^+ \to \overline{D}^0\pi^+$ decay chain. The added significance takes into account correlations to other variables. If it is below three, the variable is not used in the training. [3]

Rank	Name	Number	Added significance	Used
1.	B-meson $L_{xy}/\sigma(L_{xy})$	19	260.23	yes
2.	B-meson χ^2_{3D}	18	188.69	yes
3.	D-meson L_{xy}^{parent}	15	136.01	yes
4.	B-meson d_0	17	114.68	yes
5.	K from D meson $\mathcal{L}^{\text{PID}}$	4	76.76	yes
6.	K from D meson p_T	2	69.18	yes
7.	D-meson d_0	13	49.36	yes
8.	B-meson p_T	16	50.28	yes
9.	D-meson $L_{xy}/\sigma(L_{xy})$	11	36.34	yes
10.	D-meson $\alpha_{\text{cms}}^{\text{parent}}$	14	37.29	yes
11.	$m(D)$	12	24.08	yes
12.	D-meson p_T	10	22.86	yes
13.	K from D meson pull^{ToF}	6	17.78	yes
14.	π from D meson p_T	8	17.32	yes
15.	π from B meson p_T	21	11.39	yes
16.	K from D meson $\mathcal{L}^{\text{PID}}$	5	10.92	yes
17.	π from B meson p_T	20	9.52	yes
18.	π from D meson p_T	9	4.27	yes
19.	K from D meson ϕ	7	0.96	no
20.	K from D meson p_T	3	0.70	no

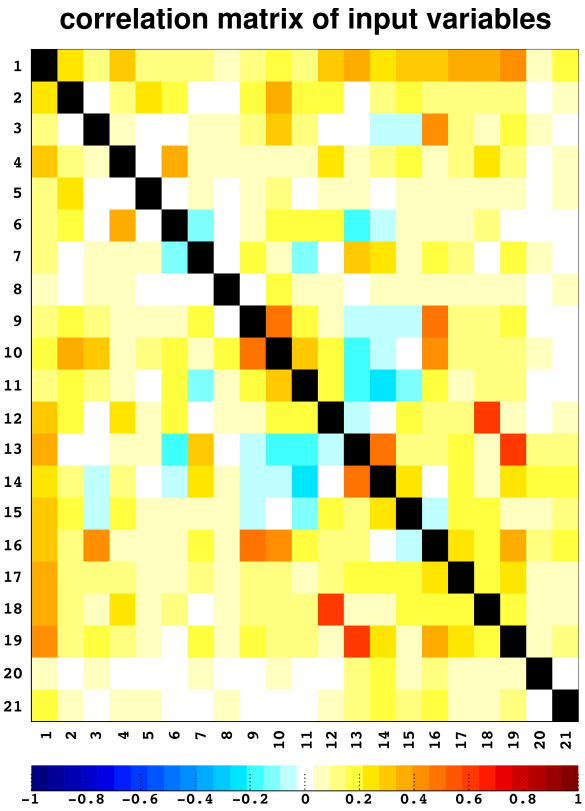

Figure 5.3.: Visualization of the correlation matrix in the NeuroBayes training using pseudo-colors for the $B^+ \to \overline{D}^0\pi^+$ decay chain. The target corresponds to variable 1. The numbers of the input variables 2-21 are given in Table 5.3. [3]

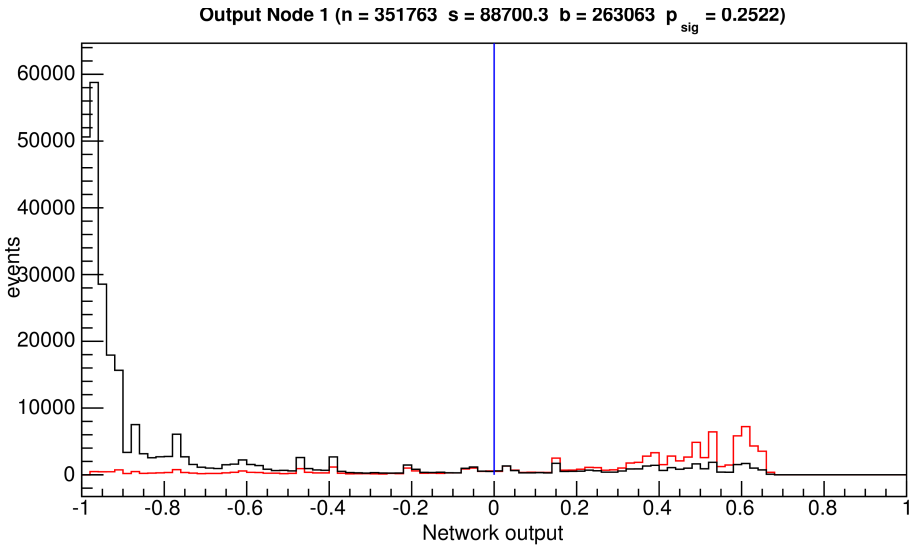

Figure 5.4.: Distributions of the NeuroBayes output for signal (red) and background (black) for the $B^+ \to \overline{D}^0\pi^+$ decay chain. [3]

5.3. $B^{**}_{(s)}$-Candidate Selection

The combination of a B meson with an additional pion or kaon introduces a large number of wrong random combinations. These are suppressed using a second set of NeuroBayes trainings. For the training process, simulated signal events are used. In order to extract the measured quantities with the highest possible precision, the selection cut on the final NeuroBayes discriminant is optimized.

5.3.1. NeuroBayes Selection

$B^{**}_{(s)}$ mesons are selected with ten different NeuroBayes instances; each one optimized for one combination of a $B^{**}_{(s)}$-meson flavor and B-meson decay chain. This section describes the instance trained for the $B^{**0} \to B^+\pi^-$ and subsequently $B^+ \to \overline{D}^0\pi^+$ decay chain. The training variables in the other nine instances are shown in appendix C.

In the B-meson NeuroBayes selection the signal contained in the measured data was sufficient to use measured data as a training sample. In contrast, this is not possible for the $B^{**}_{(s)}$-meson selection due to the much lower yield of signal events. In addition, using the ${}_s\mathcal{P}lot$ method could bias the amount and the shape of the signal.

For this reason, full event and detector simulations of $B^{**}_{(s)}$-meson decays, described in section 4.2.1, are used to train the NeuroBayes instances. A particular property of the simulations is that the distribution of the mass of the primary $B^{**}_{(s)}$ meson was not produced peaking at the nominal mass, but distributed flatly over a wide range of mass. If this had not been done, there would have been the risk that the multivariate selection was biased to enhance the signal. The mass spectrum of the simulations is shown in Fig. 5.5. Instead of the reconstructed $B^{**}_{(s)}$-meson mass $m(Bh)$, the Q value, defined as

$$Q = m(Bh) - m(B) - m_h, \tag{5.1}$$

is used to determine the resonance parameters because it reduces the effect of the detector resolution. h denotes a pion or kaon. The shown spectrum for simulations is not flat any more, because the reconstruction efficiency depends on the Q value.

There are no simulations available of the background processes for this analysis. A background sample has to be chosen from data, so the reconstructed $B^+\pi^-$ data with the B-meson selection applied is used. It contains a negligible fraction of signal, as can be observed from Fig. 5.6.

As signal simulations and background data have different shapes in Q value, the NeuroBayes training would learn that the signal-to-background ratio varies depending on Q value. In order to avoid this, training weights for the simulated

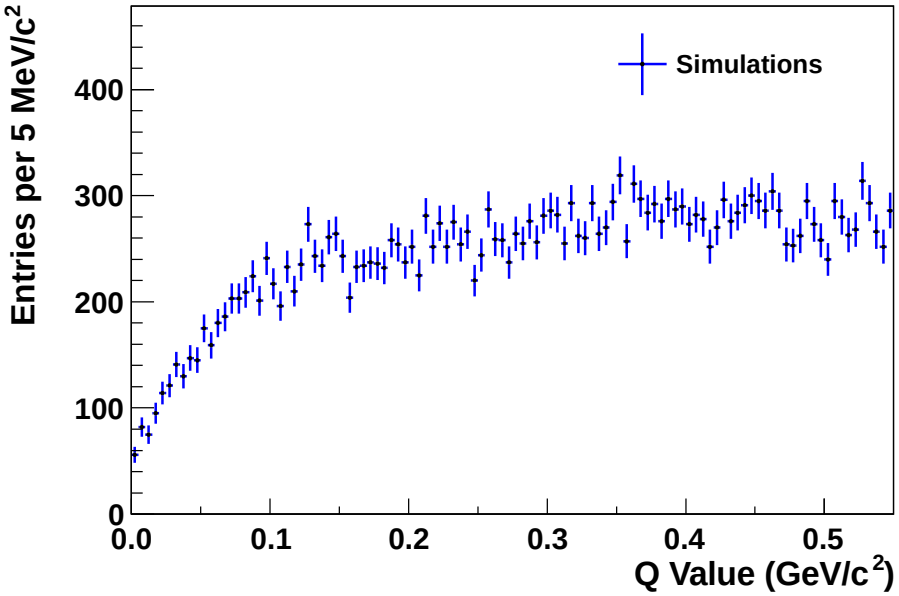

Figure 5.5.: Q-value spectrum of simulated $B^{**0} \to B^+\pi^-$ (with $B^+ \to \overline{D}^0\pi^+$) candidates with the B-meson selection applied, before the $B^{**}_{(s)}$-meson selection.

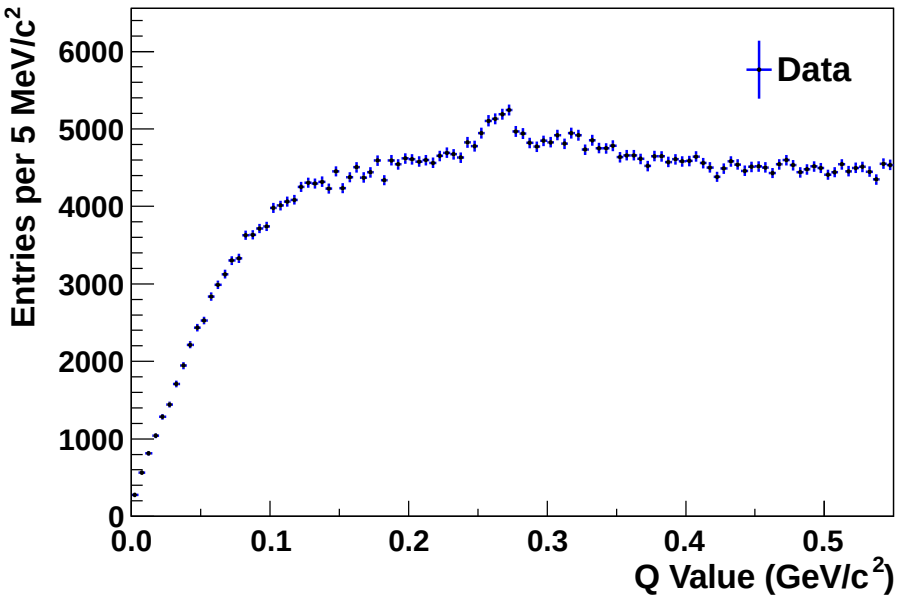

Figure 5.6.: Q-value spectrum of measured $B^{**0} \to B^+\pi^-$ (with $B^+ \to \overline{D}^0\pi^+$) candidates with the B-meson selection applied, before the $B^{**}_{(s)}$-meson selection.

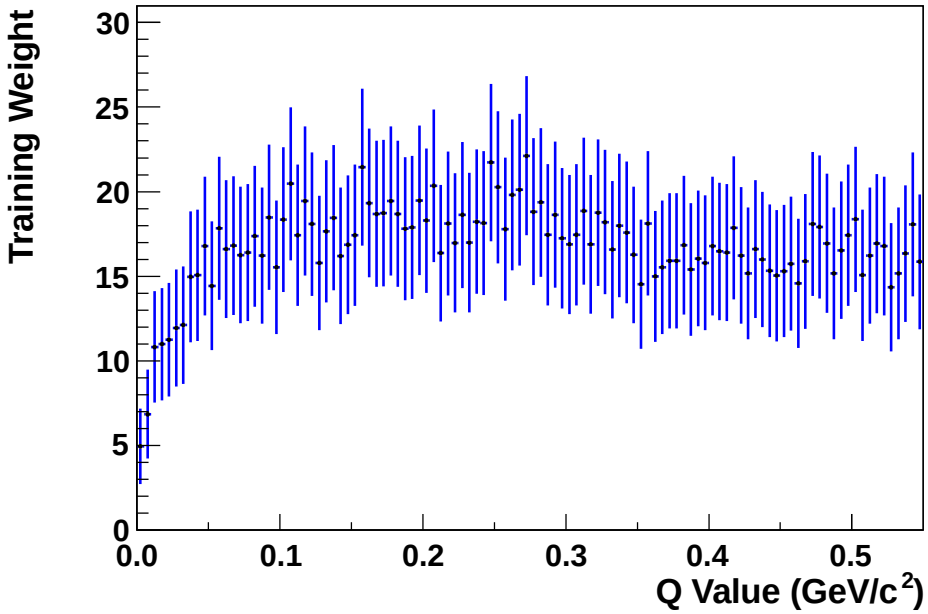

Figure 5.7.: Weights applied to the signal simulations in the NeuroBayes training for the selection of $B^{**0} \to B^+\pi^-$ (with $B^+ \to \overline{D}^0\pi^+$) candidates.

signal events are introduced in a way that at each Q value the signal-to-background ratio is 0.5. The Q-value dependence of the weights is shown in Fig. 5.7.

Inputs for the training are the observables of the $B^{**}_{(s)}$ candidate and the pion (kaon) from the $B^{**}_{(s)}$ decay, the mass of the B candidate and the output of the NeuroBayes discriminant of the B-meson selection. All other information is already included in the B-meson discriminant. The quantities entering the training and their importances are shown in Table 5.4 and their correlation is shown in Fig. 5.8.

5.3.2. Cut Optimization

The distribution of the output of the NeuroBayes discriminant is shown in Fig. 5.9. The final selection criterion is given by a cut on this discriminant. This cut needs to be chosen carefully to find the optimal balance between a loose cut keeping enough signal for a precise measurement and a tight cut removing as many background candidates as possible.

The optimization of the cut is performed by considering a figure of merit while scanning over different cut values. The figure of merit, maximizing the significance of the considered signal, is given by

$$\mathcal{F} = \frac{S}{\sqrt{S+B}} \tag{5.2}$$

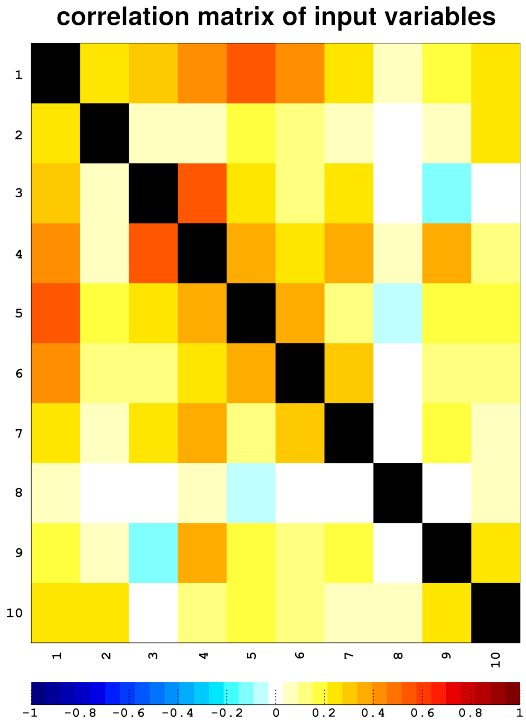

Figure 5.8.: Visualization of the correlation matrix using pseudo-colors in the NeuroBayes training for the decay $B^{**0} \to B^+\pi^-$ with the subsequent $B^+ \to \overline{D}^0\pi^+$ decay. The target corresponds to variable 1. The numbers of the input variables 2-10 are given in Table 5.4.

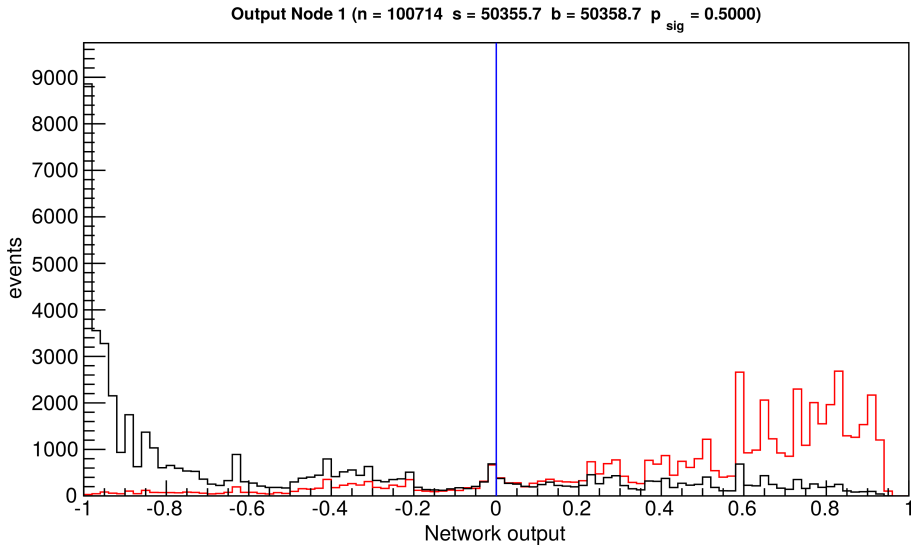

Figure 5.9.: Distributions of signal (red) and background (black) of the output of the NeuroBayes instance for the decay $B^{**0} \to B^+\pi^-$ with the subsequent $B^+ \to \overline{D}^0\pi^+$ decay.

Table 5.4.: Inputs used in the NeuroBayes training for the selection of B^{**0}-meson candidates for the decay $B^{**0} \to B^+\pi^-$ with the subsequent $B^+ \to \overline{D}^0\pi^+$ decay. All variables are used in the training.

Rank	Name	Number	Added significance
1.	π from B^{**0} meson $d_0^{\pm}$	5	179.67
2.	π from B^{**0} meson p_T	4	78.72
3.	π from B^{**0} meson pull$^{\mathrm{ToF}}$	6	60.94
4.	$m(B)$	2	45.23
5.	B-meson NeuroBayes discriminant	10	31.07
6.	B-meson $\alpha_{\mathrm{cms}}^{\mathrm{parent}}$	3	22.07
7.	π from B^{**0} meson $\mathcal{L}^{\mathrm{PID}}$ binary	8	15.80
8.	B-meson p_T	9	15.19
9.	π from B^{**0} meson $\mathcal{L}^{\mathrm{PID}}$ continuous	7	14.16

with the number of signal events S and the number of background events B. It is evaluated in the region of the decay of the B_2^* state to a B meson. The region is given in Q value by [300, 340] GeV/c^2 for B^{**0} and B^{**+} mesons and by [55, 80] GeV/c^2 for B_s^{**0} mesons. The number of expected signal events is proportional to the yield in signal simulations N_{MC}. The sum of signal and background events is given by the yield in data N_{data}, so the quantity that is maximized when varying the cut value is given by

$$\mathcal{F} \propto \frac{N_{\mathrm{MC}}}{\sqrt{N_{\mathrm{data}}}}. \tag{5.3}$$

The dependence of $\mathcal{F}$ on the cut value is shown in Fig. 5.10. The plot shows a wide plateau where $\mathcal{F}$ is nearly independent from the cut value.

The cut with the maximal value of $\mathcal{F}$ is chosen and rounded to one decimal place. The reason for rounding the cut value is to avoid choosing a cut that produces a statistical upward fluctuation of the B_2^* signal. The Q-value spectrum of measured data after the full selection process is shown in Fig. 5.11. The chosen cut values for all NeuroBayes instances are listed in Table 5.5.

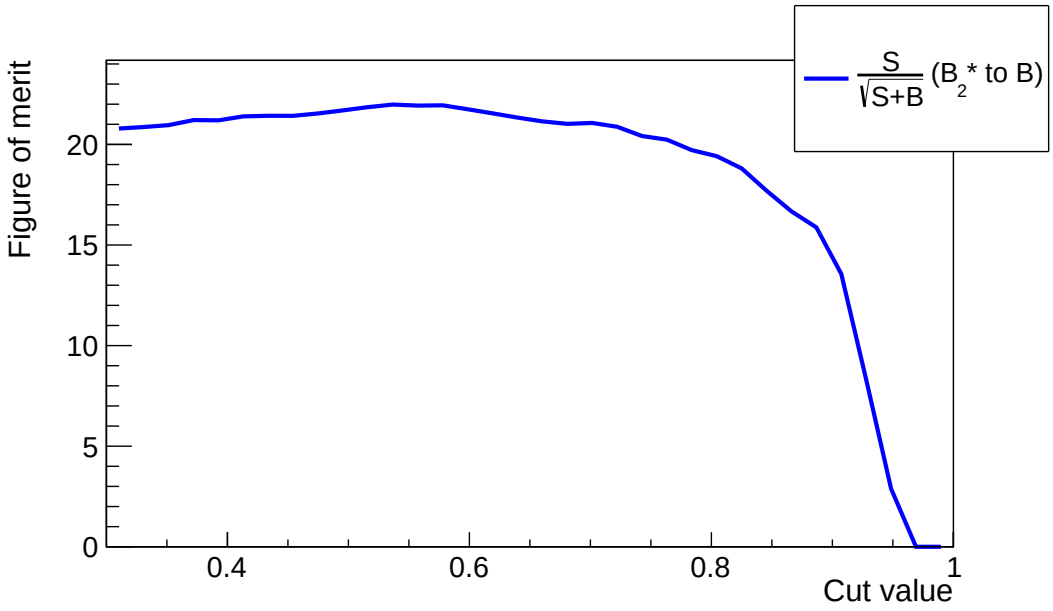

Figure 5.10.: Scan over different cut values on the NeuroBayes discriminant for the decay $B^{**0} \to B^+\pi^-$ with the subsequent decay $B^+ \to \overline{D}^0\pi^+$. The yield in simulations S is an approximation to the number of signal events, $S+B$ is the yield in data. As of the procedure described in the text, the cut value 0.5 was chosen in this case.

Table 5.5.: List of the optimal cut values on the NeuroBayes discriminant for the $B^{**}_{(s)}$-meson selection.

$B^{**}_{(s)}$ decay	B-meson decay chain	Cut value
$B^{**0} \to B^+\pi^-$	$B^+ \to \overline{D}^0\pi^+$	0.5
	$B^+ \to \overline{D}^0\pi^+\pi^+\pi^-$	0.6
	$B^+ \to J/\psi K^+$	0.7
$B^{**+} \to B^0\pi^+$	$B^0 \to D^-\pi^+$	0.5
	$B^0 \to D^-\pi^+\pi^+\pi^-$	0.6
	$B^0 \to J/\psi K^{*0}$	0.8
	$B^0 \to J/\psi K^0_s$	0.7
$B^{**0}_s \to B^+K^-$	$B^+ \to \overline{D}^0\pi^+$	0.8
	$B^+ \to \overline{D}^0\pi^+\pi^+\pi^-$	0.8
	$B^+ \to J/\psi K^+$	0.8

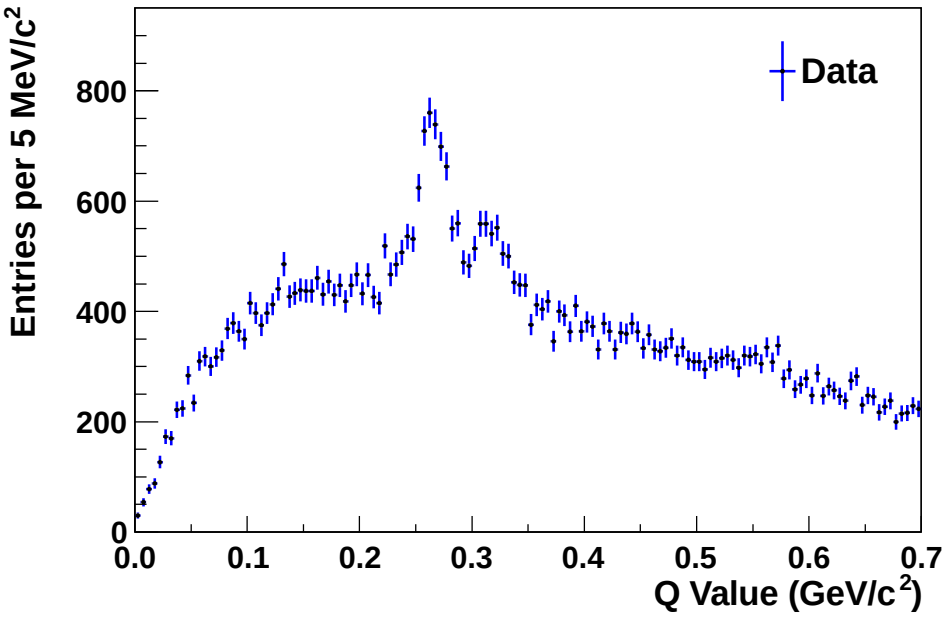

Figure 5.11.: Q-value spectrum of $B^{**0} \to B^+\pi^-$ (with $B^+ \to \overline{D}^0\pi^+$) candidates after the $B^{**}_{(s)}$-meson selection.

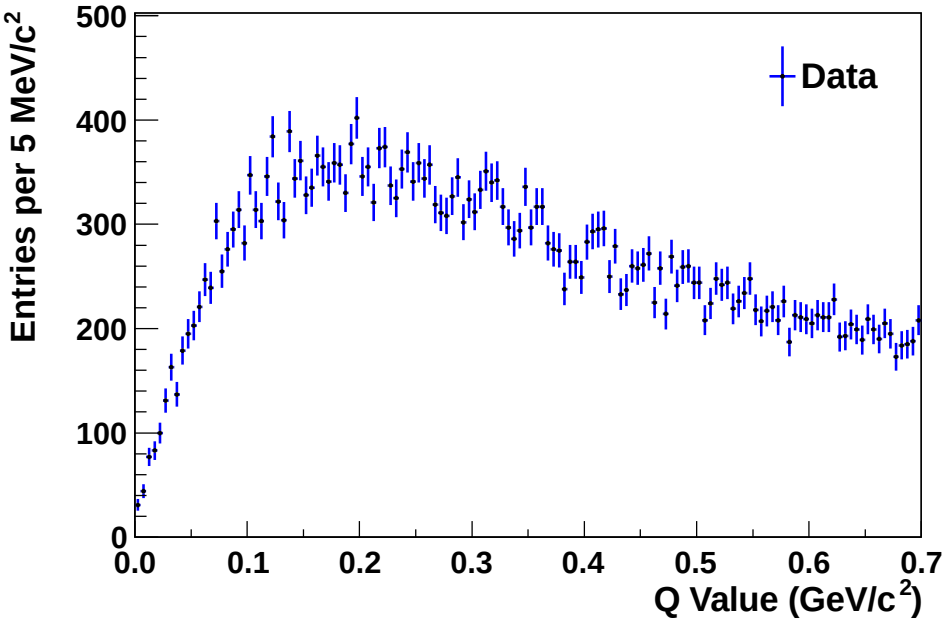

Figure 5.12.: Q-value spectrum of $B^+\pi^+$ (with $B^+ \to \overline{D}^0\pi^+$) candidates after the selection. These candidates lead to a wrong charge of the B^{**0}-meson candidate and signal is neither expected, nor observed.

5.4. Alternative $B^{**}_{(s)}$-Candidate Selection Criteria

For studies of possible systematic errors, two alternative sets of selection criteria are used: Candidates with wrong electric charge and a selection neglecting part of the multivariate analysis. Both are described in this section.

5.4.1. Wrong-Charge Candidates

As a test whether there is a systematic effect producing peaking structures looking like a signal, candidates with a wrong combination of electric charge, namely $B^+\pi^+$ combinations, are considered. In their Q-value spectrum, there should be no resonances as there are no doubly charged B mesons in nature.

The spectrum is shown in Fig. 5.12. As expected, no significant resonant structures are observed there. The distribution corresponds roughly to the shape of the background in the correct-charge combinations shown in Fig. 5.11. Although the selection criteria and the amount of data of both plots is the same, the yield and the shape of both background distributions are slightly different. The reason for this is that the physical processes responsible for finding random combinations of a charged B meson and a charged pion are different for neutral or doubly-charged combinations.

As explained in section 5.2.1, this procedure is not possible for B^{**+} meson due to B^0-$\overline{B}^0$-meson oscillations.

5.4.2. B^{**}-Candidate Selection Based on Cuts

An alternative selection for B^{**} candidates is used in order to verify that structures in the Q-value spectra are not an artifact of the multivariate B^{**}-meson selection. A possible reason for such artifacts could be that the NeuroBayes discriminant favors narrow regions of Q value due to structures in the training samples or due to the Q-value range in which the training was performed.

For the alternative selection, the B-meson selection is used in an unmodified way as it is independent from the Q value of the B^{**}-meson candidates. The NeuroBayes discriminant for the B^{**}-meson selection is not used. It is replaced by two cuts on properties of the pion from the B^{**}-meson decay. The absolute value of the significance of its impact parameter $d_0/\sigma(d_0)$ is required to be below one and its transverse momentum p_T is required to be greater than 1.5 GeV/c. There was no specified optimization procedure for the cut values.

The Q-value spectrum after the cut-based selection is shown in Fig. 5.13. Two B^{**0} signal peaks are visible between 0.25 and 0.35 GeV/c^2. Other structures cannot be clearly seen due to relatively low statistics. They become visible when the data of both B^{**0} and B^{**+} mesons are combined and all B-meson decay chains are considered (cf. Fig. 8.1, 8.2 and 8.4).

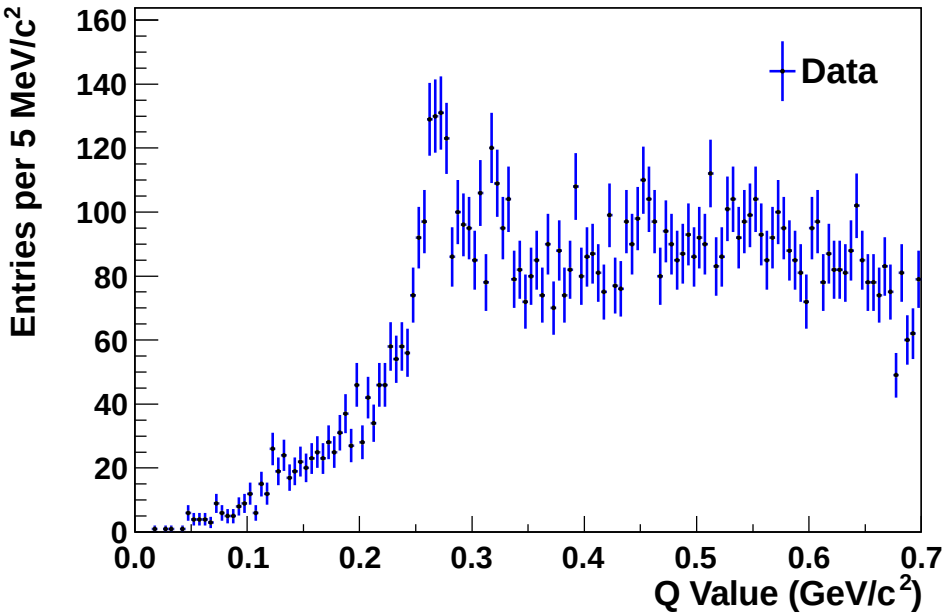

Figure 5.13.: Q-value spectrum of $B^{**0} \to B^+\pi^-$ (with $B^+ \to \overline{D}^0\pi^+$) candidates with a modified B^{**0}-meson selection. The NeuroBayes discriminant was replaced by a cut-based selection.

This selection has less discrimination power compared to the default selection, because less information is used. This can be seen when comparing to Fig. 5.11. While the signal to background ratio is roughly the same, the acceptance and thereby the yield of the cut-based selection is much lower.

6. Fit Procedure

This chapter describes the procedure to extract measured quantities from the selected data. The fit model is described in section 6.1. Some parameters of the model cannot be estimated from the measured data. They are determined in other ways and are inputs to the fit as described in section 6.2. The fit procedure is explained in section 6.3.

6.1. Components of the Fit Model

This section specifies the components of the fit model used to describe all components present in the Q-value spectra of candidates for excited $B_{(s)}$ mesons. These candidates are given by reconstructed and selected $B^+\pi^-$, $B^0\pi^+$ and B^+K^- combinations. Alternative fit models are also discussed. They are used to determine systematic uncertainties and for time-consuming calculations.

6.1.1. Relativistic Breit-Wigner Distribution

Each time resonances like $B^{**}_{(s)}$ mesons are produced and the mass of the resonance is measured, the value of this mass is distributed randomly in a region around the mean mass of the resonance. This phenomenon can be explained by the uncertainty principle. The lifetime of the resonance, determined by the properties of its decay, is relatively short. Due to the short lifetime the energy or mass of the resonance has a natural uncertainty.

An approximation of the distribution of the observed mass m of a resonance with the mean mass M is given by the non-relativistic Breit-Wigner distribution

$$p(m) = \frac{1}{2\pi} \frac{\Gamma}{(m-M)^2 + \Gamma^2/4}. \tag{6.1}$$

The full width at half maximum of the resonance Γ is closely related to its lifetime.

For many resonances this model is not sufficient, when they are studied with high statistics. Then the relativistic Breit-Wigner distribution with amplitude

$$A_l(m) = \frac{M\Gamma_l(m)}{(M^2 - m^2) - iM\Gamma_l^{\mathrm{tot}}(m)} \tag{6.2}$$

yields a better description. This formula takes into account the angular momentum l between the daughter particles in the two-body decay of the resonance. The partial width of the considered decay mode is indicated by Γ_l, and Γ_l^{tot} is the total width of the resonance given by the sum of all partial widths.

The width of a resonance increases when the phase space for its decay products gets larger. This happens when the mass of the resonance is increased, which means for particles in the right tail of the Breit-Wigner distribution the width is larger than of particles in the left tail; it depends on the mass m. This effect is particularly important for resonances with large widths and for decays with a small phase space. The latter situation is referred to as decays close to threshold.

The relation between Γ_l and m depends on the angular momentum l between the decay products [58]. It is given by

$$\Gamma_0(m) = \Gamma \frac{M}{m} \left(\frac{q}{Q} \right) \tag{6.3}$$

$$\Gamma_1(m) = \Gamma \frac{M}{m} \frac{1 + r^2 Q^2}{1 + r^2 q^2} \left(\frac{q}{Q} \right)^3 \tag{6.4}$$

$$\Gamma_2(m) = \Gamma \frac{M}{m} \frac{9 + 3r^2 Q^2 + r^4 Q^4}{9 + 3r^2 q^2 + r^4 q^4} \left(\frac{q}{Q} \right)^5 \tag{6.5}$$

with the momentum of the decay products in the rest frame of the resonance [2]

$$q(m) = \frac{\left((m^2 - (m_1 + m_2)^2) \, (m^2 - (m_1 - m_2)^2) \right)^{1/2}}{2m} \tag{6.6}$$

with the mother particle mass m and the daughter particle masses m_1 and m_2. Q is given by $Q = q(M)$. The mass-dependent widths include Blatt–Weisskopf barrier factors which are the terms with q in the denominator. Omitting them would lead to a continuous increase of the width with increasing mass, so that the cross section of the resonance would not go down to zero when m increases. The radius of the resonance is described by the parameter r. Based on previous analyses [31], a value of $r = 3.5$ GeV^{-1} is assumed.

The PDF of the $B^{**}_{(s)}$ resonances is given by the absolute value of the product of the amplitude of the production and the decay process. The decay is described in detail in section 2.2. For the narrow states, it is a D-wave process with $l = 2$. The topology of the production process is different and states with up to $J = 2$ can be formed using only the intrinsic spins of two gluons. Therefore production via S-wave is possible and higher angular momenta are suppressed in the production. The PDF for the narrow $B^{**}_{(s)}$ resonances reads

$$p(m) = |A^{\text{prod}}(m) \cdot A^{\text{dec}}(m)| = |A_0(m) \cdot A_2(m)|. \tag{6.7}$$

6.1.2. Structure of the Signal

As described in section 2.2 three narrow resonances are expected in the Q-value spectrum of each B^{**0}, B^{**+} and B_s^{**0}-meson candidates. Two peaks correspond to the B_2^* resonance. One of them is observed at the nominal Q value of the B_2^* state and the other one is shifted to a lower Q value by the mass difference between the B^* meson and the B ground state. The third peak corresponds to the B_1 state and its Q value is also lowered by the mass difference between the B^* state and the B ground state. It is assumed that there is no interference between the orbitally excited B-meson states.

The total width used in the relativistic Breit-Wigner distribution of the B_2^* state is given by the sum of the two partial widths given by the decays to either a B or a B^* meson $\Gamma^{\mathrm{tot},B_2^*}(m) = \Gamma^{B_2^*\to B^*h}(m) + \Gamma^{B_2^*\to Bh}(m)$. For the B_1 state it is equal to the partial width of the only decay mode $\Gamma^{\mathrm{tot},B_1}(m) = \Gamma^{B_1\to B^*h}(m)$.

The shape of each peak is determined by two main effects, the natural shape of the resonance, described in section 6.1.1, and the detector resolution. The latter broadens the distribution of the peak due to measurement uncertainties of the detector. It has been studied with simulated events. The results of this study are presented in section 6.2.2.

When observing the mass of a particle measured with the CDF II detector, this mass is randomly distributed following the line shape of the resonance and the obtained mass is then altered according to the detector resolution. The resulting distribution is given by the convolution of the PDF describing the detector resolution and the PDF describing the natural shape of the resonance. In the fits for this analysis, the convolution is performed using a fast Fourier transform.

In the spectra of B^{**0} and B^{**+}-meson candidates, an excess over the background expectation is observed in this analysis around a Q value of 550 MeV/c^2. After further investigation, it is interpreted as an excited B-meson state and given the name $B(5970)$. As its angular momentum and possible substructure are unknown, it is described with a non-relativistic Breit-Wigner distribution. The convolution of this PDF with a Gaussian distribution is called Voigt profile. It can be evaluated analytically avoiding the convolution. Therefore it requires less computing time.

The fit model includes three quantities describing the relative yields of the four peaks. As a reference, usually the $B_2^* \to Bh$ transition is chosen, because its peak is well isolated from the other signals. The yields of the $B_2^* \to B^*h$ and $B(5970) \to B\pi$ decays are parameterized relative to this yield. The amount of B_1 mesons is described relative to the total amount of B_2^* mesons.

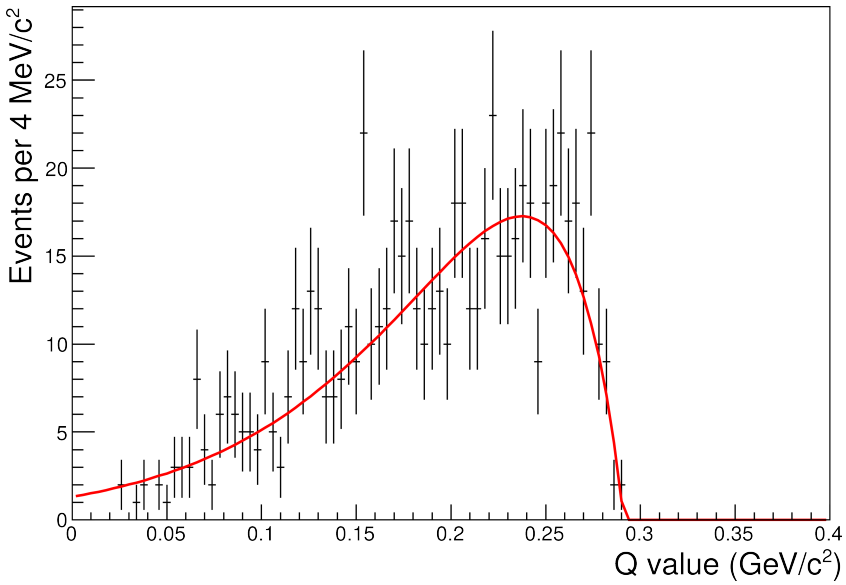

Figure 6.1.: Result of the fit to the Q-value spectrum of simulated B_s^{**0} mesons reconstructed as B^{**0} mesons.

6.1.3. $B_{(s)}^{**0}$ Reflections

In some cases it happens that the kaon in the decay $B_s^{**0} \to B^{(*)}K$ is mis-interpreted as a pion. These B_s^{**0} mesons then appear in the Q-value spectrum of B^{**0}-meson candidates and may produce a peaking structure. The other way round pions from B^{**0}-meson decays can be mis-identified as kaons and produce structures in the spectra of B_s^{**0} mesons. Both cases were studied using simulated events. Simulations of B_s^{**0}-meson decays were reconstructed as B^{**0}-meson candidates. Simulated events with a B_s^{**0}-meson mass corresponding to one of the narrow states were considered. The spectrum of the mis-reconstructed B_s^{**0} mesons is shown in Fig. 6.1. The shape of the spectrum shows a softly rising part starting from 0 to the peak at 0.25 GeV/c^2 and afterwards a sharp drop. This shape is phenomenologically modeled by a gamma distribution.

The amount of correctly reconstructed and selected B_s^{**0} simulations is compared to the observed yield of selected B_s^{**0} mesons in data. This determines which fraction of simulations corresponds to the amount of signal in the data. This fraction is used to scale the yield of data in Fig. 6.1 to get the expected yield of B_s^{**0} reflections in B^{**0}-meson data.

The shape of mis-identified B^{**0} mesons as B_s^{**0} candidates is shown in Fig. 6.2. The region of the B_s^{**0} fits reaches from 0 to 0.1 GeV/c^2. In this region the mis-identified B^{**0} mesons show a linearly rising shape and no significant peaks. Due to this, no component for reflections is used in the B_s^{**0} fit, but the reflections are well described by the phenomenological background model.

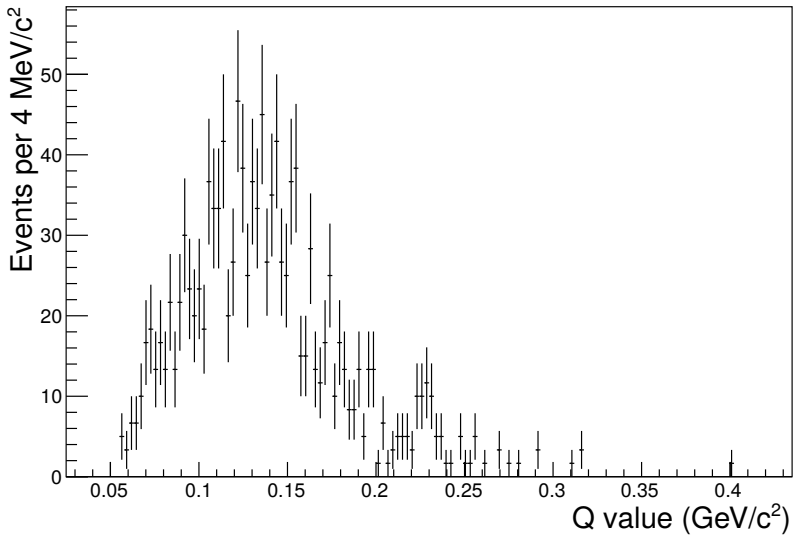

Figure 6.2.: Q-value spectrum of simulated B^{**0} mesons reconstructed as B_s^{**0} mesons.

6.1.4. Background Model

For the background a phenomenological model is selected by comparing different types of analytical functions. The tested functions comprise a gamma distribution [59], an argus distribution [60] and polynomials of different orders. These functions were fit to the Q-value spectra of each B^{**0}, B^{**+} and B_s^{**0} mesons for each B-meson decay chain separately. The region containing the signal peaks was cut out in the fits. It is given by [0.2, 0.35] GeV/c^2 for B^{**0} and B^{**+} mesons and by [0.005, 0.03] and [0.05, 0.08] GeV/c^2 for B_s^{**0} mesons. As a figure of merit, the χ^2 value of the data and the fit PDF is calculated. The results are shown in Table 6.1.

When interpreting this results, the number of parameters of the fit model is important. When neglecting the yield, a polynomial of the order N has N degrees of freedom. The used implementation of the gamma distribution in RooFit (RooGamma) has two degrees of freedom, as the threshold parameter μ is set to zero. The argus distribution has three degrees of freedom. Models with more degrees of freedom can lead to a lower χ^2 value by over-fitting the data. When the difference of the χ^2 values of two models was not not larger than 4 the model with less parameters was chosen. After this procedure a gamma distribution was chosen for the B^{**0} and B^{**+} spectra, a linear model was chosen for the B_s^{**0}-meson decays including a D meson and a second order polynomial is used for the decay chain containing a J/ψ. In the two decay channels of B^{**+} mesons which include a D meson, a phenomenologically motivated polynomial of the first order was added to better describe the spectrum near $Q = 0$.

Table 6.1.: χ^2 value of different background parameterizations. The number of degrees of freedom is 50 for B^{**0} and B^{**+} and 22 for B_s^{**0} fits. "-" indicates not tested. The used background model is indicated by an underline. The alternative background model is indicated by **bold numbers**.

	Decay mode	Gamma	Argus	pol1	pol2	pol3	pol4	pol5	pol6
B^{**0}	$B^+ \to \overline{D}^0\pi^+$	95	95	-	-	110	**48**	44	44
	$B^+ \to \overline{D}^0\pi^+\pi^+\pi^-$	50	49	-	-	56	**41**	39	-
	$B^+ \to J/\psi K^+$	101	97	-	-	108	**83**	79	-
B^{**+}	$B^0 \to D^-\pi^+$	68	74	-	-	72	**45**	44	-
	$B^0 \to D^-\pi^+\pi^+\pi^-$	57	57	-	-	**33**	31	-	-
	$B^0 \to J/\psi K^{*0}$	64	63	-	-	72	**55**	55	-
	$B^0 \to J/\psi K_s^0$	66	65	-	-	**62**	59	53	48
B_s^{**0}	$B^+ \to \overline{D}^0\pi^+$	-	-	31	**30**	29	-	-	-
	$B^+ \to \overline{D}^0\pi^+\pi^+\pi^-$	-	-	13	**12**	-	-	-	-
	$B^+ \to J/\psi K^+$	-	-	51	37	**37**	-	-	-

6.1.5. Alternative Background Model

For each fit, an alternative background model is defined. It is used to estimate the systematic influence of choosing a phenomenological model background model on the results of the measurement. For B^{**0} and B^{**+} mesons, a polynomial is used. The order of the polynomial is determined as described in section 6.1.4 and is given in Table 6.1. For B_s^{**0} mesons, the order of the used polynomial is increased by one.

6.1.6. Simplified Model for the Significance Determination

To determine the significance of the $B(5970)$ state, a simplified fit model is used. The description of the signal and the background is done in a simple way in order to determine the significance independently from other signals and to cope with the computing time used for the p-value test.

The considered region in Q value is given by [0.4, 0.7] GeV/c^2. The lower bound of 0.4 GeV/c^2 is motivated by the fact that the B^{**} states peaking just below this region prevent finding any new signal there with the current statistics. An upper bound is motivated by the shape of the background. In the given region the background is well described by a straight line. For higher Q values the slope of the background increases and a higher order polynomial would be needed. The signal is modeled with a Voigt profile, of which the non-relativistic Breit-Wigner describes the natural width of the $B(5970)$ resonance and the Gaussian describes the detector resolution.

6.2. Inputs to the Fit Model

The main reason for the use of external inputs in the fit model is that some quantities cannot be determined from the data, like the width and the shape of the detector resolution and the relative acceptance of the selection. Some physical quantities are inputs to the fit model due to the structure of the B^{**} signal, where two peaks overlap due to their natural width.

6.2.1. Physics Constraints in the Fit

The available data of an experiment should be analyzed in a way that extracts as much information as possible. The structure of the B^{**} signal makes it however necessary to constrain the mass difference between the B^* meson and the B meson and the branching fraction of $B_2^{*0/+}$ mesons.

Mass Difference Between B^* and B mesons

The offset between the positions of the $B_2^* \to Bh$ and $B_2^* \to B^*h$ signal peaks is equal to the mass difference between B^* and B mesons. For B^+ mesons there exists an flavor-specific measurement by LHCb [2] resulting in an mass difference of

$$m_{B^{*+}} - m_{B^+} = 45.0 \pm 0.4 \text{ MeV/c}^2. \tag{6.8}$$

For B^0 mesons there exists no flavor-specific measurement and the isospin-averaged value of [2]

$$m_{B^*} - m_B = 45.8 \pm 0.35 \text{ MeV/c}^2 \tag{6.9}$$

is used. The limit of the isospin splitting given by [2]

$$|(m_{B^{*+}} - m_{B^+}) - (m_{B^{*0}} - m_{B^0})| < 6 \text{ MeV/c}^2 \tag{6.10}$$

at 95 % C.L. is used to estimate the uncertainty. The flavor-specific value is within 1.5 MeV/c^2 of the isospin-averaged measurement at 68 % C.L. and the used input for B^0 mesons is given by

$$m_{B^{*0}} - m_{B^0} = 45.8 \pm 1.5 \text{ MeV/c}^2. \tag{6.11}$$

These values and uncertainties enter the fit as a Gaussian constraint. This means that the likelihood function is extended by a Gaussian term introducing a penalty for a difference between the measured parameter and external input for this parameter.

Branching Fraction of $B_2^{*0/+}$ Mesons

The relative branching fraction of $B_2^{*0/+}$ mesons is calculated by writing it as the fraction of the partial widths taking into account the D-wave decay using Eq. 6.5

$$\frac{\mathcal{B}(B_2^* \to B\pi)}{\mathcal{B}(B_2^* \to B^*\pi)} = \frac{\Gamma^{B_2^* \to B\pi}}{\Gamma^{B_2^* \to B^*\pi}} = F_b \frac{9 + 3r^2 \left(q^{B^*}\right)^2 + r^4 \left(q^{B^*}\right)^4}{9 + 3r^2 \left(q^B\right)^2 + r^4 \left(q^B\right)^4} \left(\frac{q^B}{q^{B^*}}\right)^5 \tag{6.12}$$

where $q^{B^{(*)}}$ denotes the momentum of the decay products in the rest frame of the resonance for the the decay to $B\pi$ ($B^*\pi$). The terms containing $q^{B^{(*)}}$ can be calculated from the masses of the involved particles. They quantify the effect that the phase space of the decay is smaller when the daughter particles are heavier. The ratio of the form factors F_b is given by the ratio of the mass-independent widths Γ in Eq. 6.5 and does not depend on the phase space. In heavy quark symmetry F_b is equal to the corresponding quantity F_c in D^{**} mesons. There the relative branching fraction of the D_2^{*0} state has been measured [2] to be

$$\frac{\mathcal{B}(D_2^{*0} \to D^+\pi^-)}{\mathcal{B}(D_2^{*0} \to D^{*+}\pi^-)} = 1.54 \pm 0.15 \tag{6.13}$$

and F_c can be extracted by applying Eq. 6.12 analogically. Due to heavy quark symmetry, $F_b = F_c$ is assumed and inserted into Eq. 6.12 and the result for the relative branching fraction of the $B_2^{*0/+}$ state is obtained. For the radius parameter a value of $r = 3.5$ GeV/c^2 is used. As an estimate for the uncertainty of this calculation r is varied to zero, which corresponds to omitting the Blatt-Weisskopf form factor. The uncertainty of the calculation is then given by the difference between both results and the final result

$$\frac{\mathcal{B}(B_2^* \to B\pi)}{\mathcal{B}(B_2^* \to B^*\pi)} = 1.02 \pm 0.24 \tag{6.14}$$

enters the B^{**0} and B^{**+} fits as a Gaussian constraint.

As a test for this method, the relative branching fraction of B_{s2}^{*0} mesons is calculated in the same way:

$$\frac{\mathcal{B}(B_{s2}^* \to B\pi)}{\mathcal{B}(B_{s2}^* \to B^*\pi)} = 0.08 \pm 0.02. \tag{6.15}$$

The quantitative difference of this result from Eq. 6.14 is due to the difference in phase space of the final states. It is later compared to the result measured on data.

Reflections of B_s^{**0} Mesons

In the fit to the spectrum of excited B^0-meson candidates, a component for reflections of B_s^{**0} mesons is used. The shape and the yield of this component is

determined from simulated events. Both quantities enter the fit as fixed quantities. They are determined as described in section 6.1.3.

In terms of the implementation of the RooGamma function, the shape of the cross feed is given by the parameters $\gamma = 1.71$, $\beta = 0.061$ and $\mu = -0.286$. The distribution is mirrored by replacing Q by $-Q$. The yield of the cross feed corresponds to about 8 % of the yield of the $B_2^{*0} \to B^+\pi^-$ decay.

6.2.2. Detector Resolution

The limited precision of the momentum measurement of the detector causes a statistical fluctuation in the measured masses of intermediate resonances around their true mass. This means that the peaks of resonances are broader than their natural shape. To measure the natural width of a particle it is therefore necessary to take into account the shape of the detector resolution.

The shape of the detector resolution is determined from signal simulations because there both the measured and the true mass of the resonance are known. The shape of the detector resolution depends on the Q value so it is determined separately for each signal peak. The full reconstruction and selection process is performed to the simulated events. Then the following six regions in Q value are considered:

- 270 ± 10 MeV/c^2 for B^{**}-meson decays including a B^* meson,
- 315 ± 10 MeV/c^2 for B^{**}-meson decays including a B meson,
- 10 ± 5 MeV/c^2 for B_{s1}^0-meson decays,
- 21 ± 5 MeV/c^2 for B_{s2}^{0*}-meson decays including a B^* meson,
- 67 ± 5 MeV/c^2 for B_{s2}^{0*}-meson decays including a B meson and
- 550 ± 10 MeV/c^2 for $B(5970)$-meson decays.

The distribution of the deviation of the measured and the true Q value corresponds to the detector resolution. Examples for the shape of the detector resolution and the used analytical model are shown in Fig. 6.3 to 6.4. An analytical function to describe this distribution is found by fitting it with different types of functions. A single Gaussian function does not properly describe the data due to long tails of the distribution. The sum of two Gaussians provides a good description. The mean values of the Gaussian functions are set to zero because no systematic shift of the Q value is observed. The shape is determined by a set of three parameters, describing the two widths σ_1 and σ_2 and the relative yield of the narrower Gaussian r_1. The parameters describing the detector resolution are shown in Table 6.2 to 6.4.

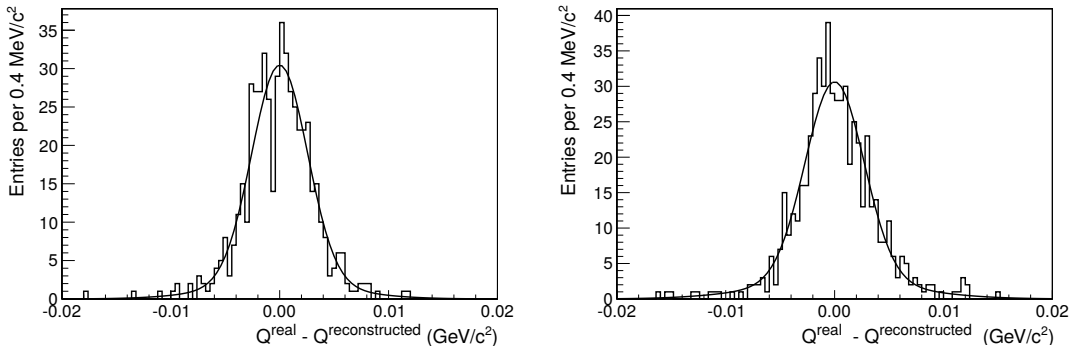

Figure 6.3.: Q-value resolution of the CDF II detector and fit of an analytical model. Left: B_1^0 or B_2^{*0} mesons decaying to $B^{*+}\pi^-$, right: B_2^{*0} mesons decaying to $B^+\pi^-$. [3]

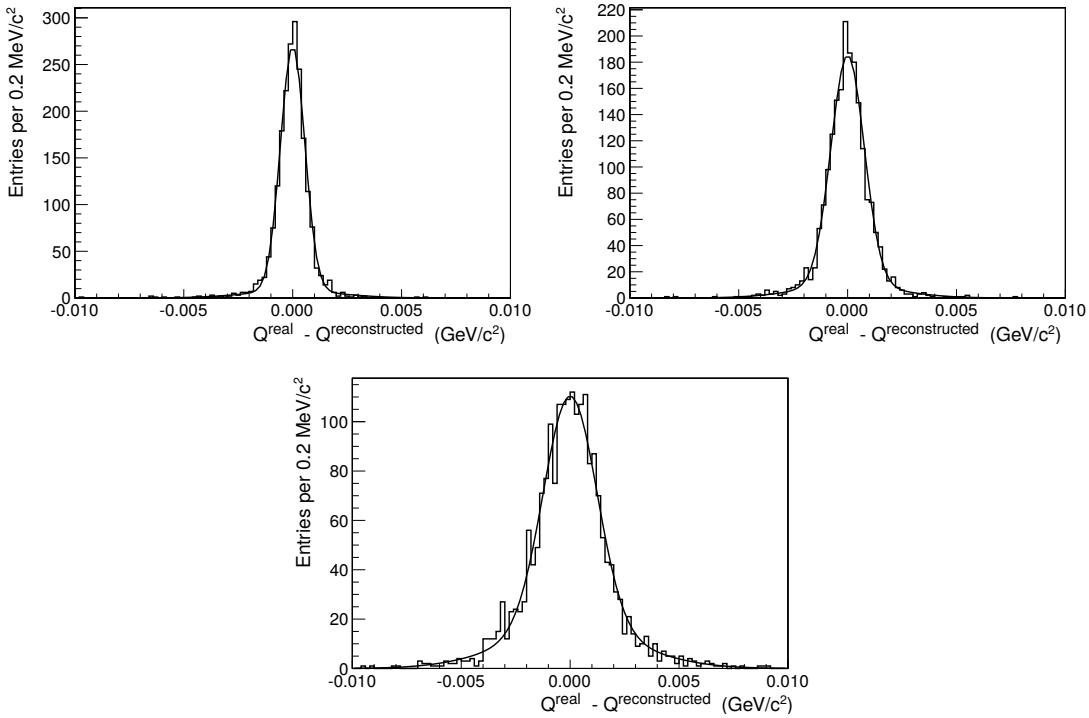

Figure 6.4.: Q-value resolution of the CDF II detector and fit of an analytical model. Top left: B_{s1}^0 mesons decaying to $B^{*+}K^-$, top right: B_{s2}^{*0} mesons decaying to $B^{*+}K^-$, bottom: B_{s2}^{*0} mesons decaying to B^+K^-. [3]

Table 6.2.: Parameters and statistical uncertainty of the B^{**0}-meson resolution model. Top: decays of B_1^0 and B_2^{*0} mesons to $B^{*+}\pi^-$ combinations, bottom: decays of B_2^{*0} mesons to $B^+\pi^-$ combinations. [3]

B decay channel	r_1 [%]	σ_1 [MeV/c^2]	σ_2 [MeV/c^2]
$B^+ \to \overline{D}^0\pi^+$	90 ± 4	2.56 ± 0.13	5.7 ± 0.6
$B^+ \to \overline{D}^0\pi^+\pi^+\pi^-$	95 ± 2	2.93 ± 0.14	9.1 ± 1.8
$B^+ \to J/\psi K^+$	92.6 ± 1.6	2.52 ± 0.08	6.6 ± 0.4

B decay channel	r_1 [%]	σ_1 [MeV/c^2]	σ_2 [MeV/c^2]
$B^+ \to \overline{D}^0\pi^+$	91 ± 4	2.78 ± 0.15	6.4 ± 0.7
$B^+ \to \overline{D}^0\pi^+\pi^+\pi^-$	97 ± 2	3.18 ± 0.19	10 ± 4
$B^+ \to J/\psi K^+$	91 ± 2	2.76 ± 0.09	6.5 ± 0.4

Table 6.3.: Parameters and statistical uncertainty of the B^{**+}-meson resolution model. Top: decays of B_1^+ and B_2^{*+} mesons to $B^{*0}\pi^+$ combinations, bottom: decays of B_2^{*+} mesons to $B^0\pi^+$ combinations. [3]

B decay channel	r_1 [%]	σ_1 [MeV/c^2]	σ_2 [MeV/c^2]
$B^0 \to D^-\pi^+$	91 ± 3	2.44 ± 0.11	5.7 ± 0.5
$B^0 \to D^-\pi^+\pi^+\pi^-$	83 ± 16	2.2 ± 0.6	5.4 ± 1.4
$B^0 \to J/\psi K^{*0}$	91 ± 2	2.96 ± 0.13	8.4 ± 0.8
$B^0 \to J/\psi K_s^0$	91 ± 2	2.97 ± 0.10	7.6 ± 0.6

B decay channel	r_1 [%]	σ_1 [MeV/c^2]	σ_2 [MeV/c^2]
$B^0 \to D^-\pi^+$	96.0 ± 1.6	2.76 ± 0.10	7.9 ± 1.1
$B^0 \to D^-\pi^+\pi^+\pi^-$	90 ± 8	2.3 ± 0.5	7.2 ± 1.9
$B^0 \to J/\psi K^{*0}$	90 ± 2	3.00 ± 0.12	8.0 ± 0.7
$B^0 \to J/\psi K_s^0$	88 ± 3	3.10 ± 0.13	7.7 ± 0.6

Table 6.4.: Parameters and statistical uncertainty of the B_s^{**0}-meson resolution model. Top: decays of B_{s1}^0 mesons to $B^{*+}K^-$ combinations, middle: decays of B_{s2}^{*0} mesons to $B^{*+}K^-$ combinations, bottom: decays of B_{s2}^{*0} mesons to B^+K^- combinations. [3]

B decay channel	r_1 [%]	σ_1 [MeV/c^2]	σ_2 [MeV/c^2]
$B^+ \to \overline{D}^0\pi^+$	97.3 ± 0.6	0.556 ± 0.015	2.16 ± 0.16
$B^+ \to \overline{D}^0\pi^+\pi^+\pi^-$	95.7 ± 1.4	0.52± 0.02	1.17 ± 0.19
$B^+ \to J/\psi K^+$	96.2 ± 0.4	0.5788 ± 0.009	3.01 ± 0.07

B decay channel	r_1 [%]	σ_1 [MeV/c^2]	σ_2 [MeV/c^2]
$B^+ \to \overline{D}^0\pi^+$	95.7 ± 1.0	0.76 ± 0.02	2.28 ± 0.18
$B^+ \to \overline{D}^0\pi^+\pi^+\pi^-$	96 ± 2	0.73 ± 0.04	2.2 ± 0.3
$B^+ \to J/\psi K^+$	95.8 ± 0.5	0.838 ± 0.012	2.74 ± 0.10

B decay channel	r_1 [%]	σ_1 [MeV/c^2]	σ_2 [MeV/c^2]
$B^+ \to \overline{D}^0\pi^+$	86 ± 3	1.23 ± 0.06	3.03 ± 0.18
$B^+ \to \overline{D}^0\pi^+\pi^+\pi^-$	90 ± 5	1.27 ± 0.10	3.1 ± 0.4
$B^+ \to J/\psi K^+$	91.3 ± 1.2	1.43 ± 0.03	3.56 ± 0.15

The simulations provide an incomplete description of the resolution because in real events many more tracks are present in the detector than in the simulations. The additional tracks degrade the detector resolution. This effect was studied in [31] in the decays $D^{*+} \to D^0\pi^+$ and $\psi(2S) \to J/\psi\pi^+\pi^-$ having the Q values 6 MeV/c^2 and 310 MeV/c^2. The resolution in measured data and simulations was compared and the resolution was found to be underestimated in the simulations by 12 % at $Q = 6$ MeV/c^2 and by 5 % at $Q = 310$ MeV/c^2. The dependence of this discrepancy on the transverse momentum was studied. It varies by 5 % in both investigated decays.

For this analysis a linear extrapolation between the given Q values is performed. Based on this, the resolution is found to be underestimated by 10 % for B_s^{**0} and by 5 % for B^{**} mesons. The width of the detector resolution determined from simulations is scaled accordingly. Motivated by the dependence on the transverse momentum, the uncertainty on the scale factor is assumed to be 5 %.

The resolution for the $B(5970)$ state is shown in Fig. 6.5. It is modeled with a single Gaussian and a width of 4.5 MeV/c^2 is found.

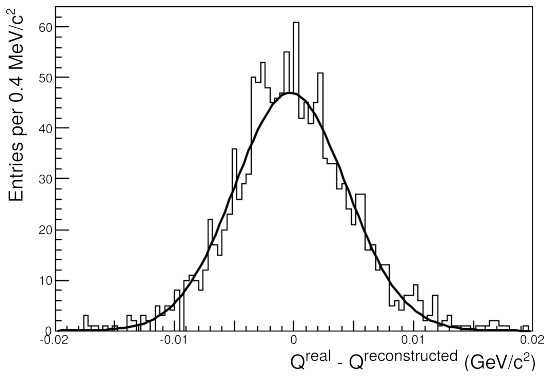

Figure 6.5.: Q-value resolution of the CDF II detector and fit of an analytical model for $B(5970)^0$ mesons decaying to $B^+\pi^-$.

6.2.3. Relative Acceptance

The probability of a $B^{**}_{(s)}$-meson candidate to be reconstructed and selected depends on the topology of its decay. This probability is referred to as selection efficiency or acceptance. Tracks of particles with very low transverse momentum are removed because their momentum is not measured precisely enough by the CDF II detector. Because the event topology and the Q value are related to each other, the selection efficiency depends on the Q value.

This has an effect on the relative yield measurements in this analysis, so it has to be taken into account. The relative efficiency is determined from signal simulations. These were generated with the $B^{**}_{(s)}$-meson mass distributed flatly over a broad range in Q value, as described in section 4.2.1. The full reconstruction and selection process is applied to the simulations. The resulting distributions are shown for a decay chain of each B^{**0} and B^{**0}_s mesons in Fig. 6.6. For B^{**0} mesons, the distribution shows a steep rise at the threshold and a flattening shape towards higher Q values. For B^{**0}_s it is flat.

The yield of simulated events is determined in the signal regions defined in section 6.2.2. They are expressed relative to the yield in the region of the $B^{**}_{(s)}$ state with the highest Q value. Table 6.5 and 6.6 shows the results of the measurement.

In the fit model the yield of all signal components is given by the relative yield with respect to the $B^*_2 \to B\pi$ or $B^*_{s2} \to BK$ decay multiplied with the determined relative acceptance. Thus the measured yield parameter is already corrected for the non-flat relative acceptance. This procedure assumes that the reconstruction efficiency is sufficiently flat inside each signal region.

To measure the production rate of B^{**} mesons relative to B mesons at the Tevatron, the efficiency to reconstruct a B^{**} meson under the condition that the B meson from its decay has been reconstructed needs to be known. This efficiency is studied for the decays $B^{**0} \to B^+\pi^-$ with the further decay $B^+ \to \overline{D}^0\pi^+$. On

simulations of this decay, the reconstruction of both B mesons and B^{**0} mesons is run. Each simulated event includes one B^{**0}-meson decay. After the full selection, 51 652 B mesons and 16 014 B^{**0} mesons are obtained, so the B^{**0} meson is reconstructed in 31 % of the cases.

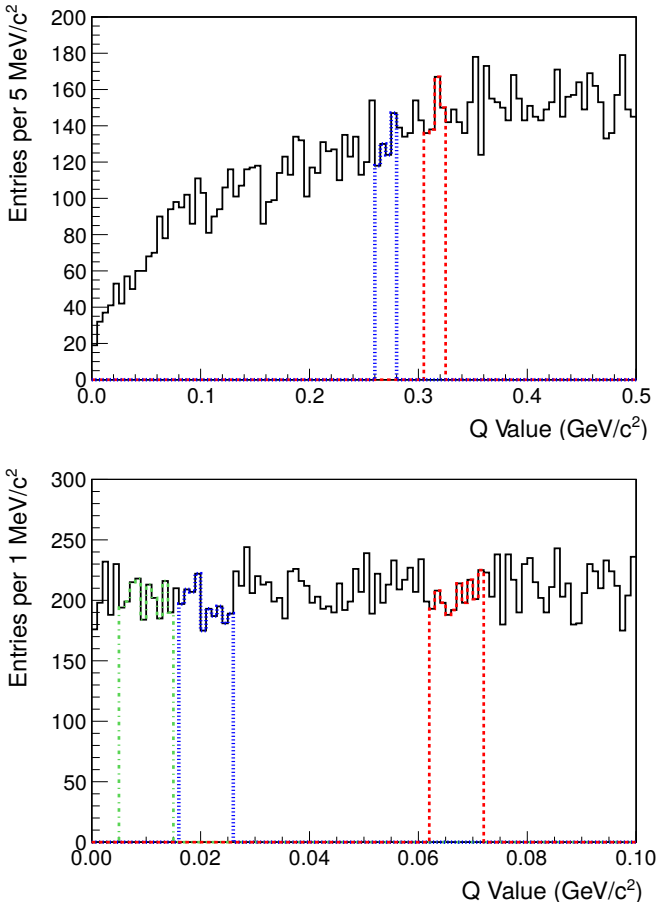

Figure 6.6.: Relative acceptance of the reconstruction and selection depending on the Q value determined from flat-mass simulations of B^{**0} mesons decaying to $B^+\pi^-$ (top) and B_s^{**0} mesons decaying to B^+K^- (bottom) with the further decay chain $B^+ \to \overline{D}^0\pi^+$. The acceptance is given by the deviation of the distribution from a flat distribution. The indicated regions are defined in section 6.2.2. [3]

Table 6.5.: Number of simulated events after the selection within the different signal regions. The relative acceptance is given with respect to the yield of the highest B^{**} signal region in Q value. The uncertainty is given by the Poisson error.[3]

	Decay mode	270 ± 10 MeV/c^2	315 ± 10 MeV/c^2
B^{**0}	$B^+ \to \overline{D}^0\pi^+$	$402 \,\widehat{\approx}\, (88 \pm 6)\,\%$	458
	$B^+ \to \overline{D}^0\pi^+\pi^+\pi^-$	$314 \,\widehat{\approx}\, (91 \pm 7)\,\%$	344
	$B^+ \to J/\psi K^+$	$1\,999 \,\widehat{\approx}\, (99 \pm 3)\,\%$	2 026
B^{**+}	$B^0 \to D^-\pi^+$	$560 \,\widehat{\approx}\, (110 \pm 7)\,\%$	510
	$B^0 \to D^-\pi^+\pi^+\pi^-$	$314 \,\widehat{\approx}\, (106 \pm 9)\,\%$	295
	$B^0 \to J/\psi K^{*0}$	$1\,022 \,\widehat{\approx}\, (100 \pm 4)\,\%$	1 026
	$B^0 \to J/\psi K^0_s$	$1\,355 \,\widehat{\approx}\, (98 \pm 4)\,\%$	1 382

	Decay mode	10 ± 5 MeV/c^2	21 ± 5 MeV/c^2
B^{**}_s	$B^+ \to \overline{D}^0\pi^+$	$2\,816 \,\widehat{\approx}\, (94 \pm 2)\,\%$	$2\,766 \,\widehat{\approx}\, (93 \pm 2)\,\%$
	$B^+ \to \overline{D}^0\pi^+\pi^+\pi^-$	$908 \,\widehat{\approx}\, (99 \pm 5)\,\%$	$971 \,\widehat{\approx}\, (106 \pm 5)\,\%$
	$B^+ \to J/\psi K^+$	$8\,135 \,\widehat{\approx}\, (104.9 \pm 1.7)\,\%$	$7\,993 \,\widehat{\approx}\, (103.1 \pm 1.6)\,\%$

	Decay mode	67 ± 5 MeV/c^2
B^{**}_s	$B^+ \to \overline{D}^0\pi^+$	2 973
	$B^+ \to \overline{D}^0\pi^+\pi^+\pi^-$	917
	$B^+ \to J/\psi K^+$	7 756

Table 6.6.: Relative acceptance in the Q-value region of the $B(5970)$ state, given separately for each B-meson decay channel relative to the region 315 ± 10 MeV/c^2.

	Decay mode	550 ± 10 MeV/c^2
B^{**0}	$B^+ \to \overline{D}^0\pi^+$	113 %
	$B^+ \to \overline{D}^0\pi^+\pi^+\pi^-$	100 %
	$B^+ \to J/\psi K^+$	109 %
B^{**+}	$B^0 \to D^-\pi^+$	110 %
	$B^0 \to D^-\pi^+\pi^+\pi^-$	96 %
	$B^0 \to J/\psi K^{*0}$	103 %
	$B^0 \to J/\psi K^0_s$	102 %

6.3. Description of the Fit Procedure

In this analysis, several fits to different data sets are performed. Besides the model to measure the properties of all excited B-meson states, described in section 6.3.1, alternative models to estimated systematic uncertainties described in chapter 7 are used. There is a dedicated model to determine the significance of the $B(5970)$ resonance described in section 6.3.2.

6.3.1. Measurement of the Properties of Excited $B_{(s)}$ Mesons

The properties of excited $B_{(s)}$ mesons are determined in three separate fits. One fit is performed for excited B^0 mesons, one for B^+ mesons and one for B_s^0 mesons. In each fit several Q-value spectra of $B\pi$ or BK combinations are fit simultaneously in the range [0, 0.7] GeV/c^2 or [0.0025, 0.1] GeV/c^2 with an unbinned maximum likelihood fit using the RooFit package [61]. The different spectra are given by data from different B-meson decay chains. For excited B^0 and B^+ mesons different spectra also originate from splitting the sample into events with only one B^{**}-meson candidate and events with multiple candidates. The latter may occur because B^{**}-meson candidates are formed from tracks in the recorded data. As there are multiple tracks in one event there may be multiple candidates per event. At most one of these candidates can be a true candidate so multi-candidate events have a lower signal purity that single-candidate events. An overview of the used spectra and the fit model is shown in Fig. 6.8 to 6.10.

Each spectrum is fit with a model containing three signal peaks for the $B_{(s)}^{**}$ resonances as described in section 6.1.2. For the spectra of excited B^0 and B^+ mesons, a Voigtian component for the $B(5970)$ state is added as motivated in section 6.1.2. The background in each spectrum is described by a gamma distribution or a polynomial (see section 6.1.4). The fit of excited B^0 mesons contains a component for wrongly reconstructed B_s^{**0} mesons which is described in section 6.1.3.

Within one fit the parameters describing the components of the model can be either floating, constrained to a value within an uncertainty, or fixed to a constant value. Independently from this, the parameters can be individual for a spectrum which means different in different spectra, or they can be shared by several spectra having the same value in each of the sharing spectra.

The parameters describing the shape of the background are floating. As the background can have a different shape in each spectrum, each spectrum has its own set of individual parameters describing the background shape. The yield and the shape of B_s^{**0}-meson reflections are fixed in the fit. Physical parameters like Q values, widths and relative yields are independent from the considered decay chain. Consequently the corresponding fit parameters are shared by all spectra within a fit and they are floating. An exception is the relative yield of the $B_2^{*0/+}$ state, which is not floating, but constrained. It is physically clearly motivated that the

two components representing the two decays of the B_2^* state have the same width. Detector effects comprising the Q-value resolution (section 6.2.2) and the relative acceptance (section 6.2.3) are quantified in advance using simulations for each B-meson decay chain individually. These quantities are fixed in the fit. The absolute yield of $B_{(s)}^{**}$ mesons in each decay channel is a floating and individual parameter. The mass difference between the two components describing the B_2^* state and their relative yield is constrained as described in section 6.2.1.

The minimization is performed with the MINUIT algorithm [62] in the RooFit package [61], which is based on the ROOT software package [63].

Yield of B^{**} Mesons Relative to B-Mesons

The combined yield of B_1^0 and B_2^{*0} mesons is compared to the yield of B^+ mesons. This study is performed on a smaller data set corresponding to an integrated luminosity of about 7 fb^{-1}, because the B^+-meson data were only available on this sample.

The yield of B^+ mesons in the decay mode $B^+ \to \overline{D}^0\pi^+$ in this sample is determined in the fit shown in Fig. 5.2 and amounts to 88 700 B^+ mesons. The yield of B^{**0} mesons in the same sample is determined from a fit with the default fit model and amounts to $3\,520 \pm 270$ B^{**0} mesons. B^{**0} mesons do not only decay to $B^+\pi^-$ combinations, but also to $B^0\pi^0$ combinations. The latter are not reconstructed in this analysis, but considering isospin, their yield is estimated to be 1/3 of all B^{**0}-mesons decays. The efficiency to reconstruct a B^{**} meson under the condition that the B meson from its decay has been reconstructed is found to be $\epsilon = 31\,\%$ in this analysis, as explained in section 6.2.3.

The ratio of B^{**0} meson produced per B^+ meson is given by the ratio of the yields corrected for the efficiency and decays to $B^0\pi^0$ combinations:

$$\frac{N_{B^{**0}}}{N_{B^+}}\frac{1}{\epsilon} = \frac{3\,520 \cdot \frac{3}{2}}{88\,700 \cdot 0.31} \approx (19 \pm 2)\,\%. \tag{6.16}$$

The statistical uncertainty comes from the yield of B^{**0} mesons only, as the uncertainty on the number of B^+ mesons is negligible.

6.3.2. Significance of the $B(5970)$ State

The significance of the $B(5970)$ state is determined using a p-value test (section 4.1.3). For this the fit has to be performed several million times in an automated way. Therefore a simplified model is used, described in section 6.1.6. It combines the data of excited B^0 and B^+ mesons in a combined fit because in both data sets an excess has been observed with a similar mass and width. The data are split by B-meson decay chain and candidate multiplicity in the same way as

described in section 6.3.1. The spectra are fit simultaneously with a binned maximum likelihood fit with a bin width of 5 MeV/c^2. This corresponds to the width of the detector resolution. The fit is performed in the Q-value range [0.4, 0.7] GeV/c^2. An overview of the spectra and the fit model is shown in Fig. 6.11.

The background model is given by a linear function. The slope is floating and individual for each spectrum in the fit. The signal PDF is given by a Voigt profile with the Gaussian width fixed to 4.5 MeV/c^2 (cf. section 6.2.2). The width and the mean value of the Breit-Wigner are floating and shared by all spectra. The width is limited to be in the interval [10, 100] MeV/c^2. The lower limit is motivated by not fitting fluctuations in single bins. Setting an upper boundary for the width parameter is motivated because very wide resonances cannot be distinguished from the background. The mean value of the Voigt profile is limited to be in the interval [0.45, 0.65] GeV/c^2 to keep the signal peak inside the fit range. The parameter for the yield of the $B(5970)$ state is floating and shared by all spectra. It is expressed relative to the yield of the B^{**}, which is known from the fit to the full Q-value spectrum. This allows to use a single yield parameter in the simultaneous fit. The boundaries of the yield parameters are chosen so loose that it is practically free in the fit. It is allowed to become negative.

Using this fit model, two fits to measured data are performed. In one fit, the yield on the $B(5970)$ state is floating (signal hypothesis), in the other fit it is set to zero (null hypothesis). The first fit is expected to describe data better and a better fit quality is expected. The latter is given by the value of the log-likelihood function nll after the minimization. For the signal hypothesis $nll = -480306$ is found, for the null hypothesis $nll = -480288$, which is an improvement by $\Delta nll = 18$.

To interpret this number, a Toy Monte Carlo study is performed. From the PDF fit to data, random data sets are generated assuming zero signal yield. To each of the random data set, two fits are performed, one with the signal hypothesis and one with the null hypothesis, and Δnll is considered. In total, 12 356 863 random data sets are evaluated. The distribution of Δnll is shown in Fig. 6.7.

In 128 of these fits, an improvement $\Delta nll > 18$ is observed. This means that assuming the absence of a $B(5970)$ signal, the probability to observe a signal at least as strong as in data is given by $\frac{128}{12\,356\,863} \approx 1.0 \cdot 10^{-5}$. This translates into a significance of 4.4σ.

Alternative Method

The choice of the background shape has an influence on the obtained significance, so an alternative model is used to verify the result. To have a stable background description with a more complex model, a wide range in Q value needs to be considered, so the default fit model is used. To cope with computing time, the parameters of the B^{**}-meson signals are fixed and only the parameters of the background PDF and the $B(5970)$ component are floating.

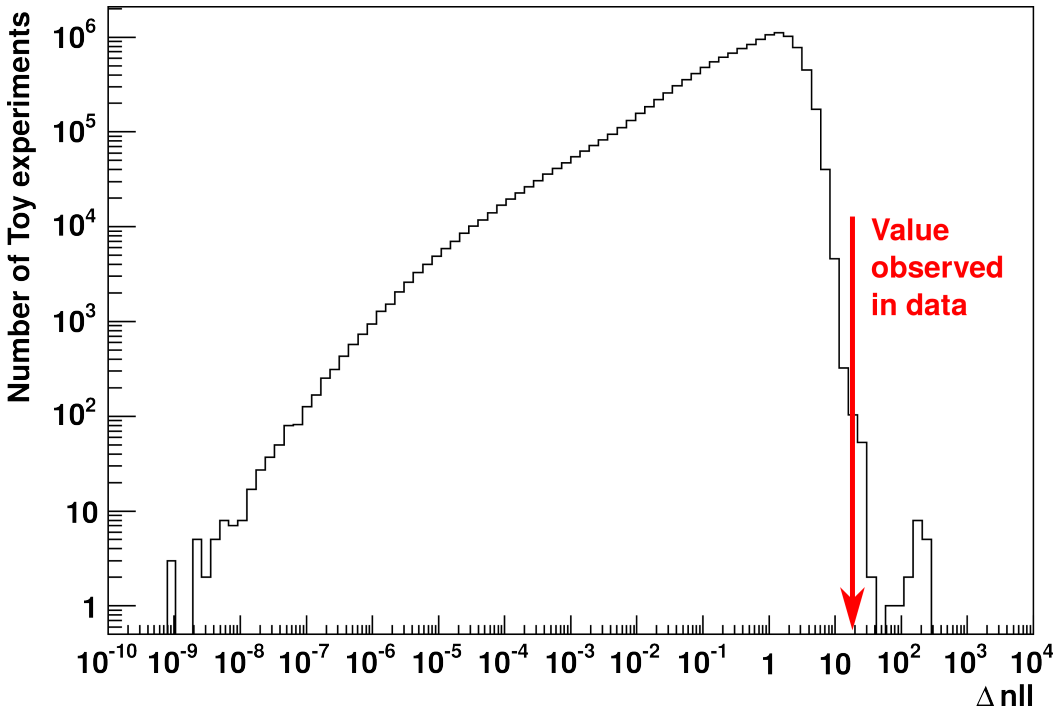

Figure 6.7.: Distribution of Δnll in the Toy Monte Carlo study.

A p-value test is performed in the same way as described before, but separately for either $B(5970)^0$ or $B(5970)^+$ candidates. On measured data $\Delta nll^{\text{neutral}} = 22$ and $\Delta nll^{\text{charged}} = 15$ is observed.

Assuming the null hypothesis, a larger signal than on data is observed in a fraction of $3.0 \cdot 10^{-5}$ Toy data sets for $B(5970)^0$ mesons and in $2.4 \cdot 10^{-4}$ Toy data sets for $B(5970)^+$ mesons. This corresponds to significances of 4.2σ or 3.7σ. Adding both value in quadrature gives a combined significance of 5.6σ.

Alternative Selection

To verify that the observed excess around 550 MeV/c^2 is not an artifact of the selection, an alternative selection is performed replacing the NeuroBayes classifier for B^{**} candidates by a small number of cuts. It is explained in section 5.4.2. The selected data are shown in Fig. 6.12. Besides the B^{**} signal, a clear peak around 550 MeV/c^2 is visible.

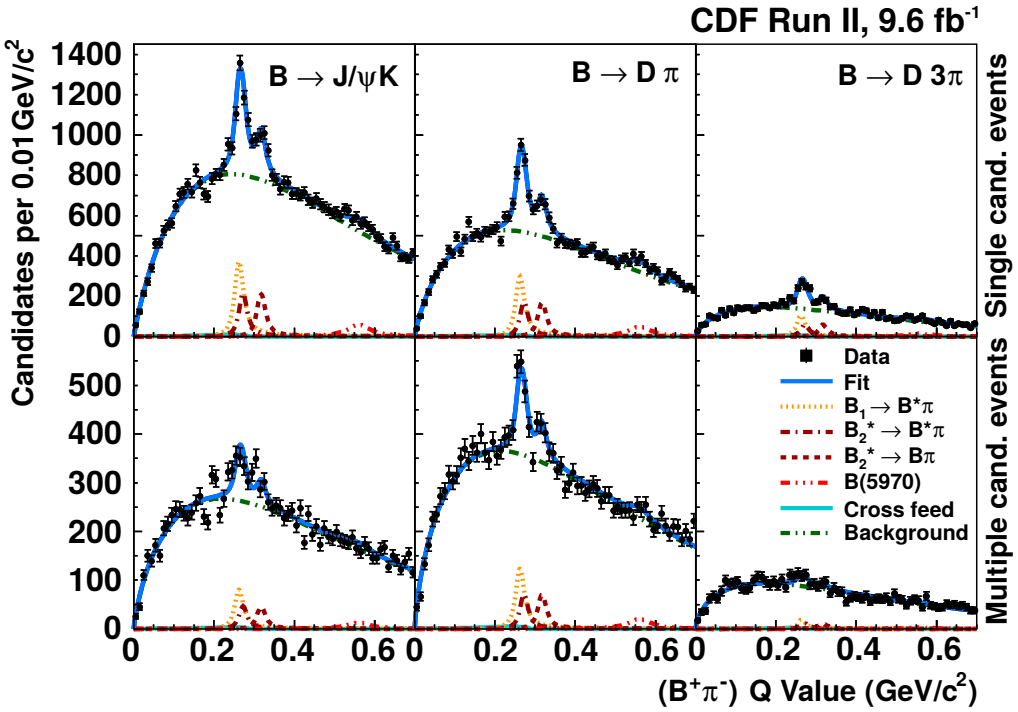

Figure 6.8.: Q-value spectra of B^{**0} candidates and $B^+\pi^+$ combinations with the fit model overlaid.

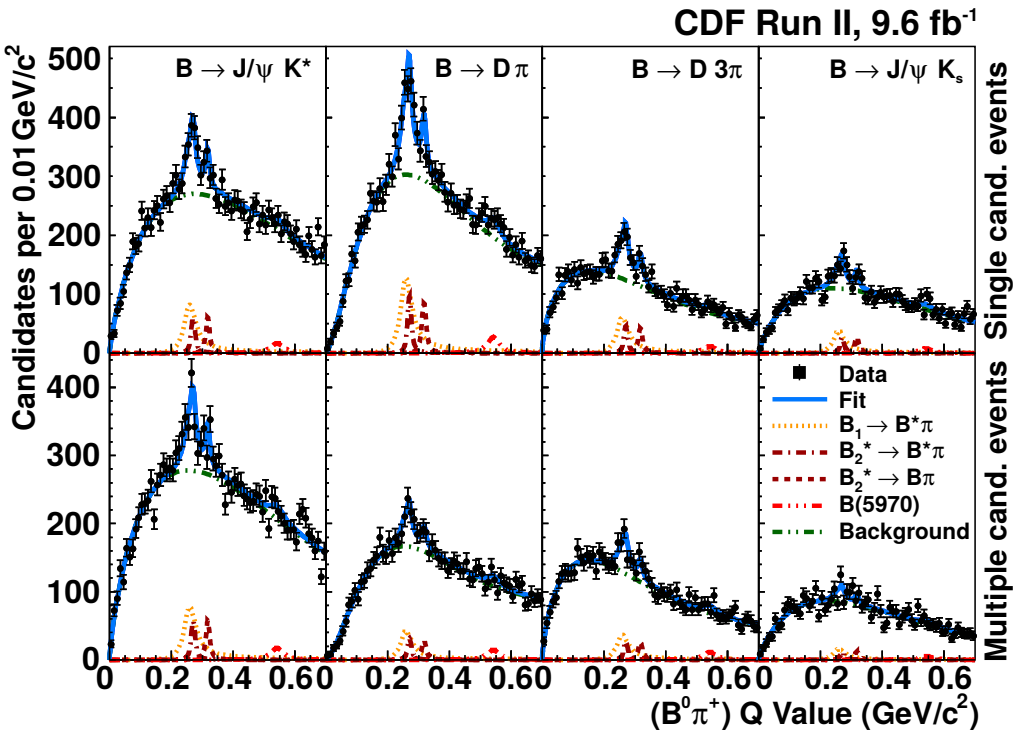

Figure 6.9.: Q-value spectra of B^{**+} candidates with the fit model overlaid.

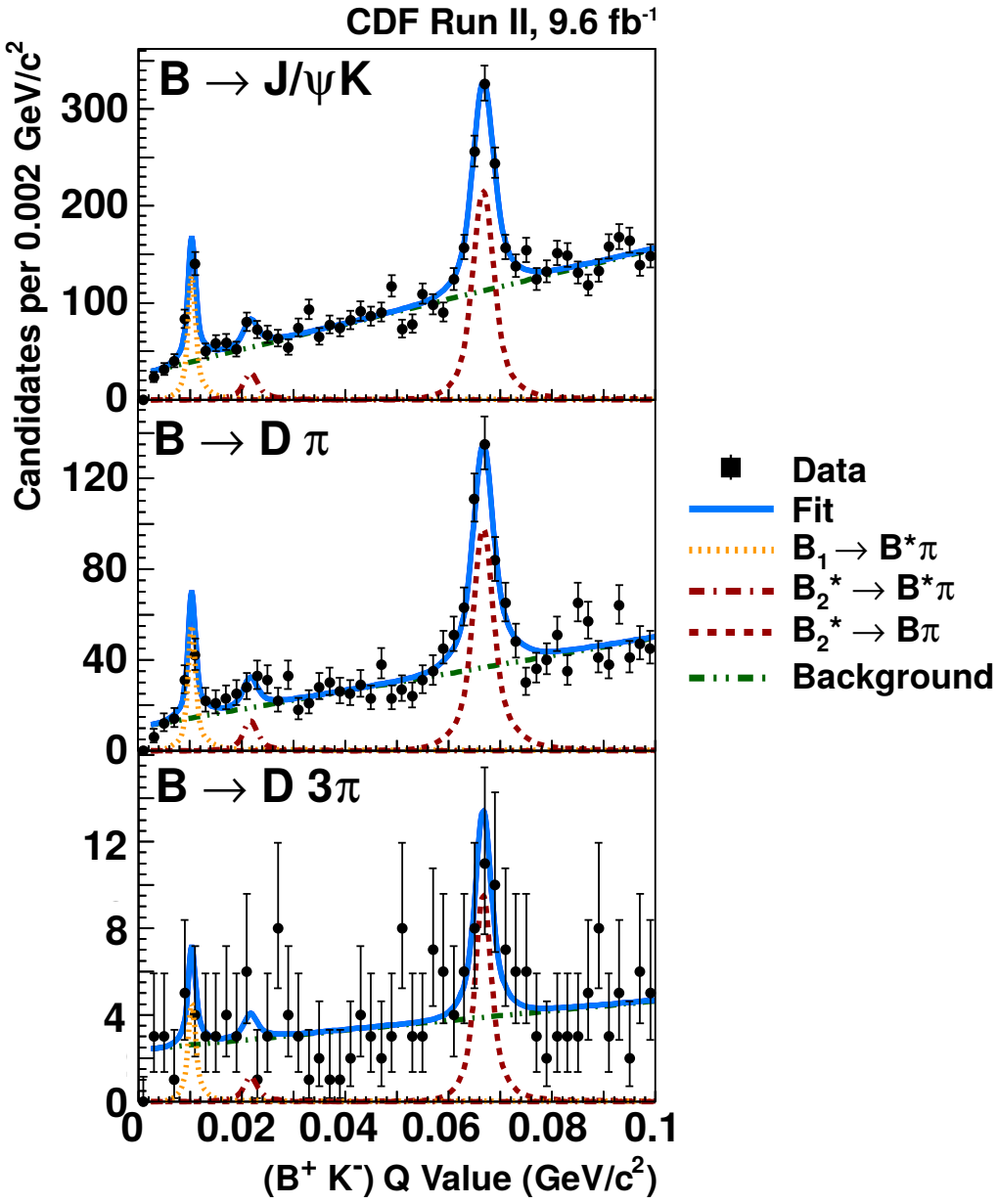

Figure 6.10.: Q-value spectra of B_s^{**0} candidates with the fit model overlaid.

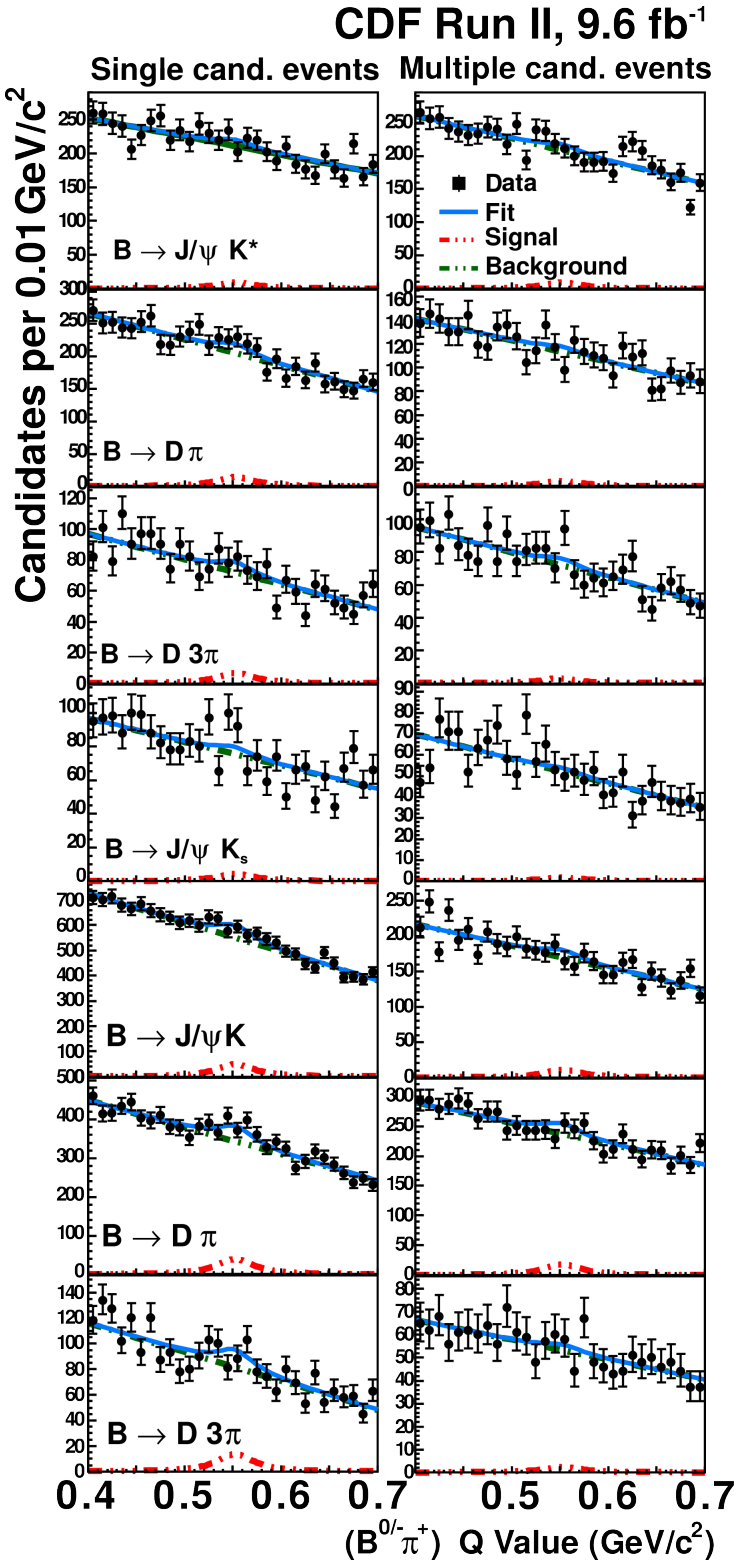

Figure 6.11.: Q-value spectra of B^{**0} and B^{**+} candidates with the simplified fit model overlaid.

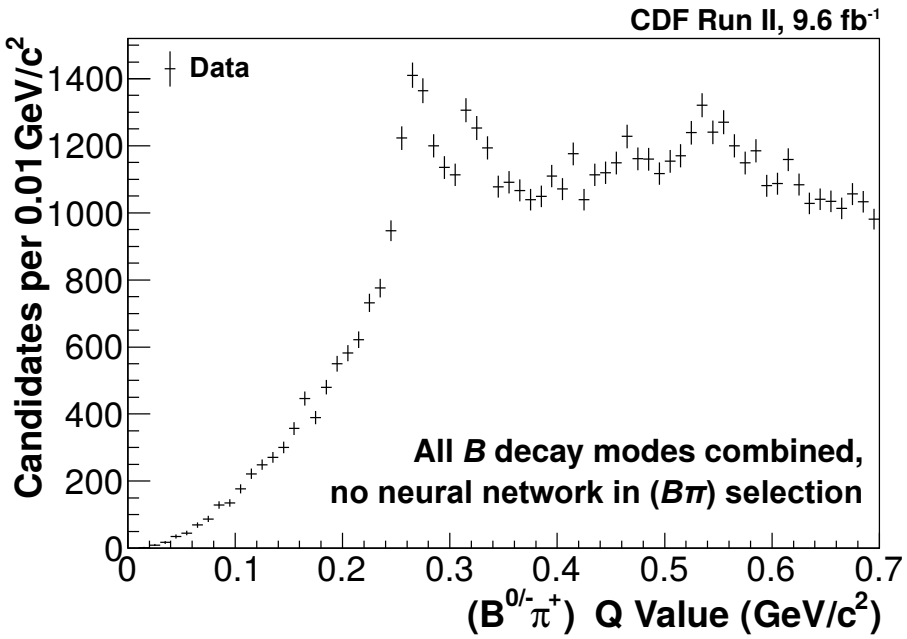

Figure 6.12.: Q-value spectrum of $B^-\pi^+$ candidates with the alternative selection.

7. Systematic Uncertainties

Systematic uncertainties on the measured quantities originate from the imperfect simulation of the detector, from the choice of the fit model and from uncertainties of constraints made in the fit. The systematic uncertainties are summarized in Table 7.1 to 7.4 and explained in the text.

7.1. Uncertainties due to Detection and Selection

Mass Scale of the CDF II Detector

The mass measurement in this analysis depends on the knowledge of the magnetic field inside the CDF II detector and the quality of the detector-material description in simulations. Both introduce an uncertainty, which was studied in previous analyses at the CDF experiment. The uncertainty was estimated to be 0.2 MeV/c^2 for B^{**0} mesons [25] and 0.14 MeV/c^2 for B_s^{**} mesons [27]. The same uncertainties are assumed in this analysis. For the $B(5970)$ state, this uncertainty is negligible in comparison to other systematic uncertainties.

Detector Resolution Model

The shape of the detector resolution is determined from simulations. As described in section 6.2.2, the width of the detector resolution is estimated to have a relative uncertainty of 5 %. Therefore fits to data are repeated with the detector resolution scaled to 95 % or 105 %. For each measured quantity the larger deviation from the default fit is assumed as systematic uncertainty. For the $B(5970)$ state, this uncertainty is negligible in comparison to other systematic uncertainties.

Non-Flat Relative Acceptance

The influence of the non-flat relative acceptance in Q value on the measurement of the signal properties is estimated with a Toy Monte Carlo study. Several hundred random data sets are generated in accordance with the fit model with a modified signal component. Using a parameterization of the acceptance depending on the Q value, the yield of the signal PDF is reweighted depending on Q value. The acceptance function is given by the fit of a second order polynomial to the relative

Table 7.1.: Absolute systematic uncertainties in the B^{**0} measurements.

	Q (MeV/c^2)		Γ (MeV/c^2)		Δm	r_{prod}
	B_1	B_2^*	B_1	B_2^*	(MeV/c^2)	
Mass scale	0.2	0.2	-	-	0.0	-
Resolution	0.0	0.0	0.3	0.2	0.0	0.0
Rel. acceptance	-	$^{+0.0}_{-0.3}$	$^{+0.6}_{-0.0}$	-	$^{+0.3}_{-0.0}$	$^{+0.1}_{-0.2}$
Fit bias	-	-	-	0.3	-	$^{+0.0}_{-0.1}$
Signal model	0.0	0.1	0.7	0.7	0.1	0.1
Background model	0.0	0.7	3.2	3.6	0.7	0.3
Broad B^{**0} states	$^{+0.1}_{-0.3}$	$^{+0.0}_{-0.4}$	$^{+0.1}_{-2.1}$	$^{+0.0}_{-3.9}$	$^{+0.3}_{-0.4}$	$^{+0.3}_{-0.0}$
Fit constraints	1.1	$^{+0.3}_{-0.2}$	$^{+1.5}_{-1.6}$	0.4	0.9	$^{+0.2}_{-0.3}$
Total systematic	$^{+1.1}_{-1.2}$	$^{+0.8}_{-0.9}$	4	$^{+4}_{-5}$	1.2	0.5

Table 7.2.: Absolute systematic uncertainties in the B^{**+} measurements.

	Q (MeV/c^2)		Γ (MeV/c^2)		Δm	r_{prod}
	B_1	B_2^*	B_1	B_2^*	(MeV/c^2)	
Mass scale	0.2	0.2	-	-	0.0	-
Resolution	0.0	0.0	0.1	0.2	0.0	0.0
Rel. acceptance	-	0.0	$^{+0.0}_{-3.8}$	$^{+1.0}_{-0.0}$	0.0	$^{+0.3}_{-0.5}$
Fit bias	-	-	$^{+0.0}_{-1.9}$	-	-	$^{+0.0}_{-0.4}$
Signal model	0.3	0.0	1.0	0.7	0.3	0.2
Background model	0.4	0.1	2.1	1.6	0.5	0.5
Broad B^{**+} states	$^{+0.2}_{-1.3}$	$^{+0.1}_{-0.0}$	$^{+0.0}_{-9.9}$	$^{+0.0}_{-3.2}$	$^{+1.3}_{-0.0}$	$^{+0.5}_{-0.2}$
Fit constraints	$^{+1.0}_{-2.2}$	$^{+0.2}_{-0.9}$	$^{+0.0}_{-7.4}$	$^{+2.8}_{-1.4}$	$^{+1.5}_{-0.8}$	$^{+0.5}_{-0.8}$
Total systematic	$^{+1}_{-3}$	$^{+0.3}_{-0.9}$	$^{+2}_{-13}$	$^{+3}_{-4}$	$^{+2}_{-1}$	$^{+0.9}_{-1.2}$

Table 7.3.: Absolute systematic uncertainties in the B_s^{**0} measurements.

	Q (MeV/c^2)		Γ (MeV/c^2)		Δm	r_{prod}	r_{dec}
	B_{s1}	B_{s2}^*	B_{s1}	B_{s2}^*	(MeV/c^2)		
Mass scale	0.14	0.14	-	-	0.01	-	-
Resolution	0.00	0.00	0.06	0.19	0.00	0.00	0.00
Rel. accept.	-	-	-	-	-	0.01	0.01
Fit bias	-	-	0.02	0.02	-	$^{+0.00}_{-0.01}$	-
Signal model	0.00	0.00	0.00	0.00	0.00	0.00	0.00
Bkg. model	0.00	0.01	0.02	0.05	0.01	0.00	0.01
Fit range	0.04	0.01	0.26	0.02	0.03	0.04	0.01
Fit constr.	0.00	0.02	0.01	0.04	0.02	0.00	0.00
Total syst.	0.15	0.14	0.3	0.2	0.04	0.04	0.02

Table 7.4.: Absolute systematic uncertainties in the neutral and charged $B(5970)$ measurements.

	Q (MeV/c^2)		Γ (MeV/c^2)		r'_{prod}	
	Neutr.	Char.	Neutr.	Char.	Neutr.	Char.
Rel. acceptance	-	$^{+1}_{-0}$	3	-	$^{+0.2}_{-0.1}$	$^{+0.2}_{-0.1}$
Fit bias	-	-	$^{+0}_{-10}$	$^{+0}_{-10}$	-	-
Background model	12	12	30	40	0.3	0.8
Total systematic	12	12	30	40	$^{+0.4}_{-0.3}$	0.8

acceptance determined from simulations. The fits are shown in Fig. 7.1. The background shape is not modified because the background model is phenomenological and its systematic influence is studied separately.

Each generated Q-value spectrum is fit with the default model, which means that the parameters and their uncertainties are estimated. The deviation of the measured from the generated value should follow a Gaussian distribution with the width given by the statistical uncertainty. Therefore the pull, defined as the difference between generated and estimated value, divided by the estimated uncertainty, is determined. It should follow a standard normal distribution.

For each measured quantity, the distribution of the pull over all random experiments is fit with a Gaussian distribution to test for a fit bias and check whether the uncertainty is correctly estimated. When a bias is present, the mean value of the Gaussian is different from zero. When the uncertainty is not estimated correctly, the width is different from one. In some measured quantities a bias is found, but in most cases this bias is found to be present in the default fit model as described in section 7.2. Therefore, it is not introduced by the non-flat acceptance, but by the fit model itself. Therefore only the additional bias found in this study is accounted for as a systematic uncertainty. Because the sign of the bias is defined by the shift of the mean value in the pull distribution, the uncertainty is asymmetric.

B^{**}-Meson Reconstruction Efficiency Relative to B Mesons

The efficiency to reconstruct a B^{**} meson when the B meson has been reconstructed is determined from simulations. For a correct result it is important that the momentum spectrum of the B^{**} mesons is well described in simulations. Therefore the agreement of simulations and data is tested.

Using the default fit, the yield of B^{**0} mesons with the further decay $B^+ \to \overline{D}^0\pi^+$ is determined in six equally populated bins of transverse momentum, so the transverse momentum spectrum in data is known. It is compared to the spectrum in simulations and the result is shown in Fig. 7.2. The yields in all bins are found to be consistent between data and simulations, so no correction is applied.

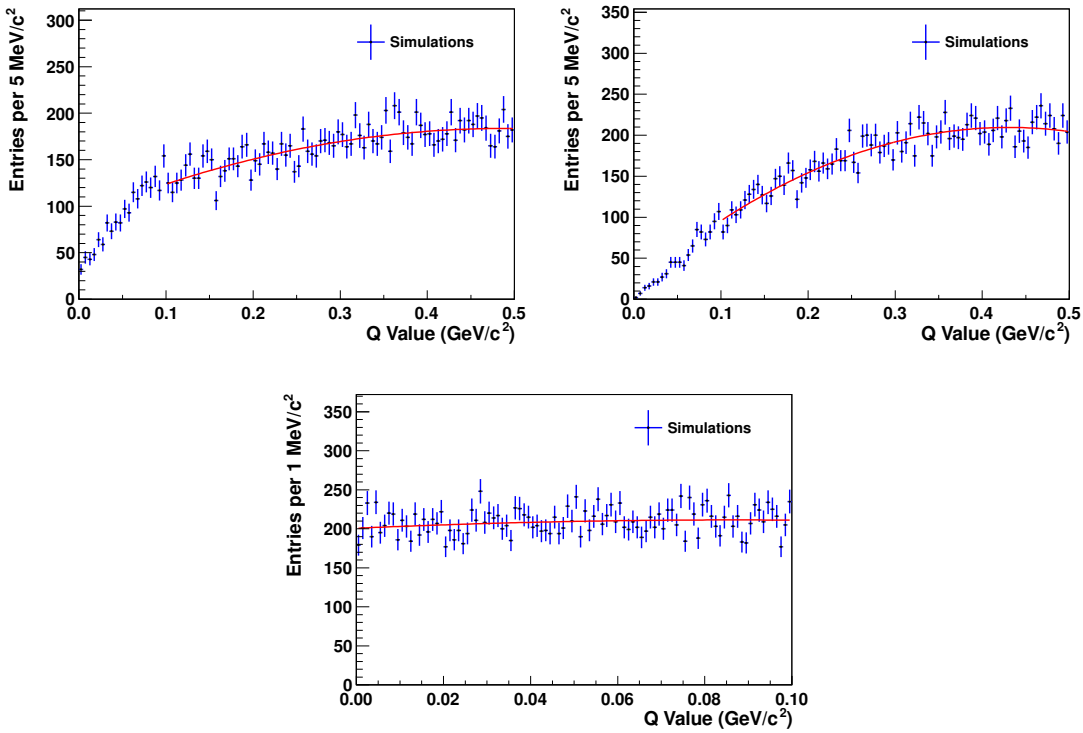

Figure 7.1.: Fit of a second order polynomial, describing the relative acceptance, to selected events of the flat-mass simulation for B^{**0} (top left), B^{**+} (top right) and B_s^{**0} (bottom) mesons.

However, in the ratio of the yields of data and simulations, a trend is observed. A straight line is fit to the ratio and is used to reweight the transverse momentum spectrum of B^{**0} mesons in simulations. After the reweighting, the yield of simulated events passing the selection increases by 22 %. The reason for this large effect is that about half of the B^{**0} mesons at the Tevatron are produced with a transverse momentum below 6 GeV/c, while CDF only allows to reconstruct B^{**0} mesons above 6 GeV/c. Therefore selected events always have weights greater than one in the reweighting. A relative uncertainty of 22 % is assumed as systematic uncertainty on the B^{**0}-meson reconstruction efficiency relative to B^+ mesons.

7.2. Fit Model Uncertainties

Fit Model Validation

The fit model is checked for a possible bias in the measured quantities and the correct estimation of the systematic uncertainties is tested using a Toy Monte Carlo study. From the PDF of the fit model, multiple random data sets are generated and

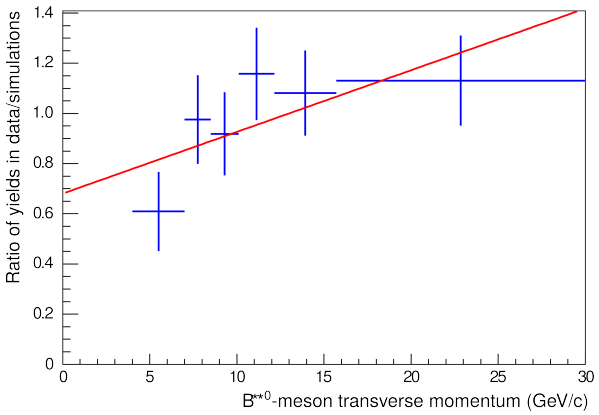

Figure 7.2.: Comparison of the B^{**0}-meson transverse momentum distribution in data and simulations. Data points show the yield in measured data divided by the yield in simulations. A linear function is fit to the distribution.

fit again. The generated and estimated parameters are compared by calculating the pull. The distributions of the pull are fit with a Gaussian distribution.

When a bias is found, the measured value is corrected for it and the amount is accounted for as a systematic uncertainty in addition. Because the sign of the bias is defined by the shift of the mean value in the pull distribution, the uncertainty is asymmetric. In Table 7.1 to 7.4, this uncertainty is referred to as fit bias.

Signal Model

The uncertainty related to the signal model is given by the choice of the radius parameter $r = 3.5$ GeV^{-1} in the Blatt-Weisskopf form factor for $B^{**}_{(s)}$ mesons. This parameter is varied in two additional fits to either 0 or 4 GeV^{-1}. The larger deviation to the default fit is assumed as a systematic uncertainty.

Background Model

The background model was chosen from a set of several phenomenological models. The uncertainty related to this choice is estimated by performing a fit with an alternative background model, described in section 6.1.6. For each measured quantity, the difference between the fit and the alternative fit is assumed as the systematic uncertainty.

Fit Range

The lower bound of the B^{**0}_s-meson fit range is given by $Q = 2.5$ MeV/c^2. This value is varied to both 0 or 5 MeV/c^2 in two alternative fits and the larger difference to the default fit results is assumed as the systematic uncertainty.

7.3. Uncertainties due to Physics Inputs

Broad B^{**} States

As described in section 2.2, the spectrum of $B^{**}_{(s)}$ mesons includes two broad states. Their exact masses and widths are unknown. These resonances can influence the shape of the background in the signal region, which is studied for B^{**} mesons.

In several additional fits, two broad Breit-Wigner components are added to the fit model. The yield of the structures is free in the fit. Within a single fit, the mean value and width of the broad structures is fixed. 100 fits are performed and the mean values and widths are varied in several combinations of mean values between 200 and 400 MeV/c^2 and widths either 100 or 200 MeV/c^2.

The largest upwards and downwards deviation of a parameter from the value in the default fit is assumed as the asymmetric systematic uncertainty.

Fit Constraints

In section 6.2.1, the values and the uncertainties of the constraints on the mass difference between B^* and B mesons, and the relative branching fraction of the B^*_2 state are explained. Both quantities are varied within their uncertainty in alternative fits and the largest upwards and downwards deviation for each measured quantity are assumed as the asymmetric systematic uncertainty.

8. Results

Orbitally Excited $B_{(s)}$ Mesons

Individual fits to the Q-value distributions of $B^+\pi^-$, $B^0\pi^+$ and B^+K^- combinations are performed and the results are shown in Fig. 8.1 to 8.3. The selected samples contain about 10 800 B^{**0} decays, 5 800 B^{**+} decays, and 1 390 B_s^{**0} decays. The Q values and widths of the narrow $B_{(s)}^{**}$-meson states are measured and the results are presented in Table 8.1.

Furthermore the production rate of the B_1 state relative to the B_2^* state multiplied by the branching fraction of both states into the analyzed decays

$$r_{\text{prod}} = \frac{\sigma(B_1)}{\sigma(B_2^*)} \cdot \frac{\mathcal{B}(B_1 \to B^* h)}{\mathcal{B}(B_2^* \to Bh) + \mathcal{B}(B_2^* \to B^* h)} \tag{8.1}$$

with the production cross-section σ at the Tevatron in the selected kinematic regime, is determined, where h identifies a pion for B^{**} and a kaon for B_s^{**0} decays. The relative branching fraction of the B_2^* state

$$r_{\text{dec}} = \frac{\mathcal{B}(B_2^* \to B^* h)}{\mathcal{B}(B_2^* \to Bh)} \tag{8.2}$$

is measured for B_s^{**0} mesons, while it is constrained in the fits of B^{**}-meson spectra. The results are shown in Table 8.2.

The production rate of narrow B^{**0} states, that is the B_1^0 and B_2^{*0} states, relative to the B^+ meson is determined. In the kinematic range of B^+ mesons with a transverse momentum larger than 5 GeV/c, this fraction is $19 \pm 2(\text{stat}) \pm 4(\text{syst})\,\%$.

The New $B(5970)$ Resonance

A broad structure is found in samples of $B^+\pi^-$ and $B^0\pi^+$ candidates. Combining both samples to the data set shown in Fig. 8.4, the significance is determined as described in section 6.3.2 and evidence for the signal is established at a statistical significance of 4.4σ. As the existence of excited B mesons at higher Q values is expected from theory and observations for D mesons, the structure is interpreted as a resonance decaying to $B\pi$ combinations. As no substructure could be resolved, it is interpreted as a single state and given the name $B(5970)$.

The samples of $B^+\pi^-$ and $B^0\pi^+$ combinations contain 2 600 $B(5970)^0$ and 1 400 $B(5970)^+$ decays. The Q values and widths of these states are measured and the results are summarized in Table 8.3.

Table 8.1.: Measured masses and widths of $B^{**}_{(s)}$ mesons. The first contribution to the uncertainties is statistical, the second is systematic.

	Q (MeV/c^2)	Γ (MeV/c^2)
B^0_1	$262.7 \pm 0.9\ ^{+1.1}_{-1.2}$	$23 \pm 3 \pm 4$
B^{*0}_2	$317.9 \pm 1.2\ ^{+0.8}_{-0.9}$	$22\ ^{+\ 3}_{-\ 2}\ ^{+\ 4}_{-\ 5}$
B^+_1	$262\ \ \pm 3\ \ ^{+1}_{-3}$	$49\ ^{+12}_{-10}\ ^{+\ 2}_{-13}$
B^{*+}_2	$317.7 \pm 1.2\ ^{+0.3}_{-0.9}$	$11\ ^{+\ 4}_{-\ 3}\ ^{+\ 3}_{-\ 4}$
B^0_{s1}	$10.35 \pm 0.12 \pm 0.15$	$0.5 \pm 0.3 \pm 0.3$
B^{*0}_{s2}	$66.73 \pm 0.13 \pm 0.14$	$1.4 \pm 0.4 \pm 0.2$

Table 8.2.: Measured relative production rates r_{prod} of $B^{**}_{(s)}$ mesons as defined in Eq. 8.1 and branching fraction of the B^*_{s2} state r_{dec} as defined in Eq. 8.2 in the visible range $p_T > 5$ GeV/c. The first contribution to the uncertainties is statistical, the second is systematic.

	r_{prod}	r_{dec}
B^{**0}	$1.0\ ^{+0.2}_{-0.4} \pm 0.5$	-
B^{**+}	$2.7\ ^{+1.6}_{-1.0}\ ^{+0.9}_{-1.2}$	-
B^{**0}_s	$0.25^{+0.07}_{-0.04} \pm 0.05$	$0.10\ ^{+0.03}_{-0.02} \pm 0.02$

The production rate of the $B(5970)$ state relative to the $B^*_2 \to B\pi$ decay multiplied by the branching fraction into the analyzed decays

$$r'_{\text{prod}} = \frac{\sigma(B(5970))}{\sigma(B^*_2)} \frac{\mathcal{B}(B(5970) \to B^{(*)}\pi)}{\mathcal{B}(B^*_2 \to B\pi)} \tag{8.3}$$

is determined, the results are presented in Table 8.4.

The masses of the excited $B_{(s)}$-meson states are calculated from the measured Q values using Eq. 5.1 and the world-average masses of their daughter particles [2] and the mass difference $m_{B^*} - m_B$, as described in section 6.2.1. The $B(5970)$ signal is assumed to decay to $B\pi$. If it decayed to $B^*\pi$, the mass would increase by $m_{B^*} - m_B$. Also the mass splitting $\Delta m = m(B^*_2) - m(B_1)$ is calculated. The results are summarized in Table 8.5.

Interpretation

The results are consistent with and more precise than previous analyses of CDF data [25, 27]. The properties of exclusively reconstructed B^{**+} mesons, the width of the B^0_1 state and the properties of the $B(5970)$ resonance are measured for the first time.

A comparison to results of the DØ [24, 28] and LHCb [26, 29] collaborations is shown in Fig. 8.5 to 8.8. The results are generally compatible, except for a

Table 8.3.: Observed properties of the broad structure. The first contribution to the uncertainties is statistical, the second is systematic.

	Q (MeV/c^2)	Γ (MeV/c^2)
$B(5970)^0$	$558 \pm 5 \pm 12$	$70\,^{+30}_{-20} \pm 30$
$B(5970)^+$	$541 \pm 5 \pm 12$	$60\,^{+30}_{-20} \pm 40$

Table 8.4.: Measured relative production rates r'_{prod} of the $B(5970)$ state as defined in Eq. 8.3 in the visible range $p_T > 5$ GeV/c. The first contribution to the uncertainties is statistical, the second is systematic.

	r'_{prod}
$B(5970)^0$	$0.5\,^{+0.2}_{-0.1}\,^{+0.4}_{-0.3}$
$B(5970)^+$	$0.7\,^{+0.3}_{-0.2} \pm 0.8$

Table 8.5.: Calculated masses and mass differences of the observed states. The first contribution to the uncertainties is statistical, the second is systematic, the third is the uncertainty on the masses of the daughter particles.

	m (MeV/c^2)
B_1^0	$5726.6 \pm 0.9\,^{+1.1}_{-1.2} \pm 0.4$
B_2^{*0}	$5736.7 \pm 1.2\,^{+0.8}_{-0.9} \pm 0.2$
B_1^+	$5727 \pm 3\,^{+1}_{-3} \pm 2$
B_2^{*+}	$5736.9 \pm 1.2\,^{+0.3}_{-0.9} \pm 0.2$
B_{s1}^0	$5828.3 \pm 0.1 \pm 0.2 \pm 0.4$
B_{s2}^{*0}	$5839.7 \pm 0.1 \pm 0.1 \pm 0.2$
$B(5970)^0$	$5978 \pm 5 \pm 12$
$B(5970)^+$	$5961 \pm 5 \pm 12$

	Δm (MeV/c^2)
B^0	$10.2 \pm 1.7 \pm 1.2 \pm 0.4$
B^+	$10 \pm 3\,^{+2}_{-1} \pm 2$
B_s^0	$11.4 \pm 0.2 \pm 0.0 \pm 0.4$

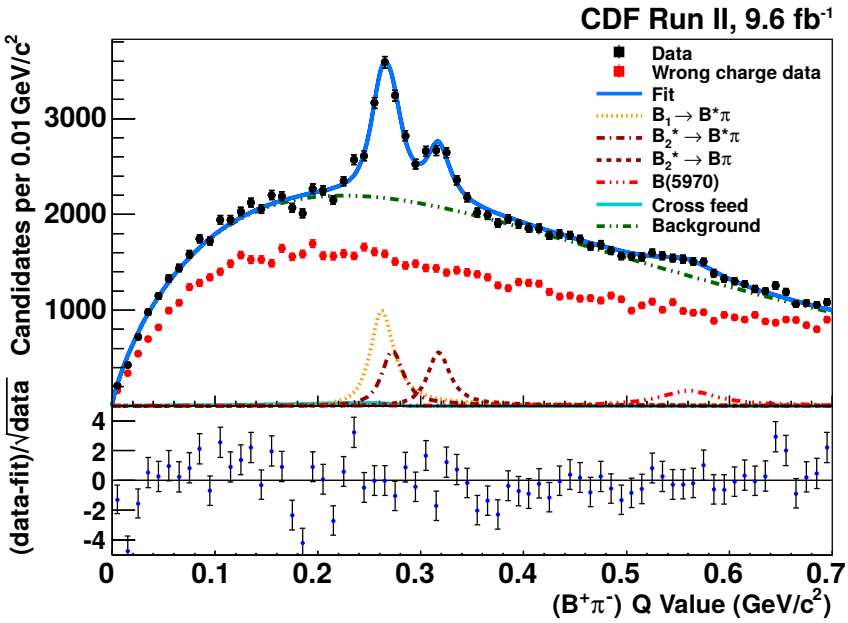

Figure 8.1.: Distribution of Q value of $B^+\pi^-$ and $B^+\pi^+$ combinations with fit results overlaid summed over all decay channels. The lower part shows the deviation of the $B^+\pi^-$ yields from the fit function normalized to the Poisson uncertainty of the data.

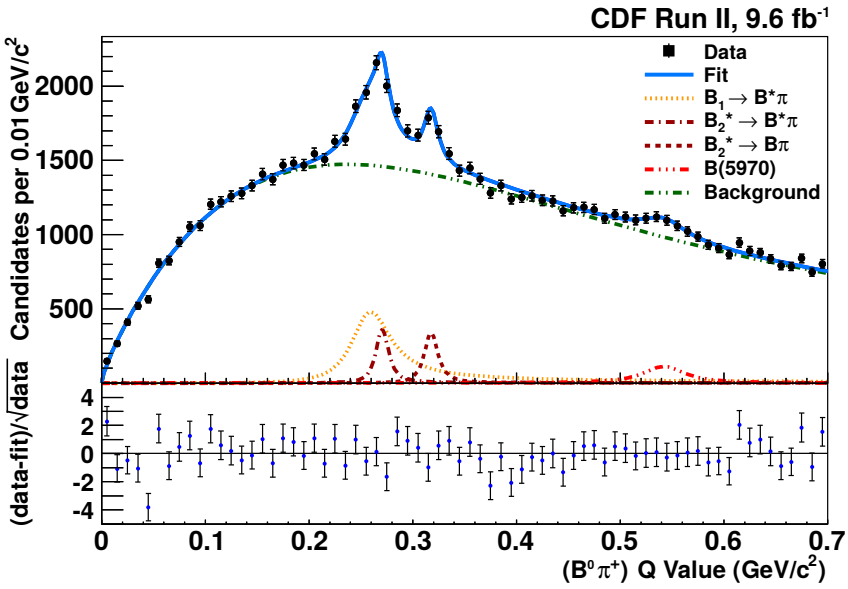

Figure 8.2.: Distribution of Q value of $B^0\pi^+$ combinations with fit results overlaid summed over all decay channels. The lower part shows the deviation of the yields from the fit function normalized to the Poisson uncertainty of the data.

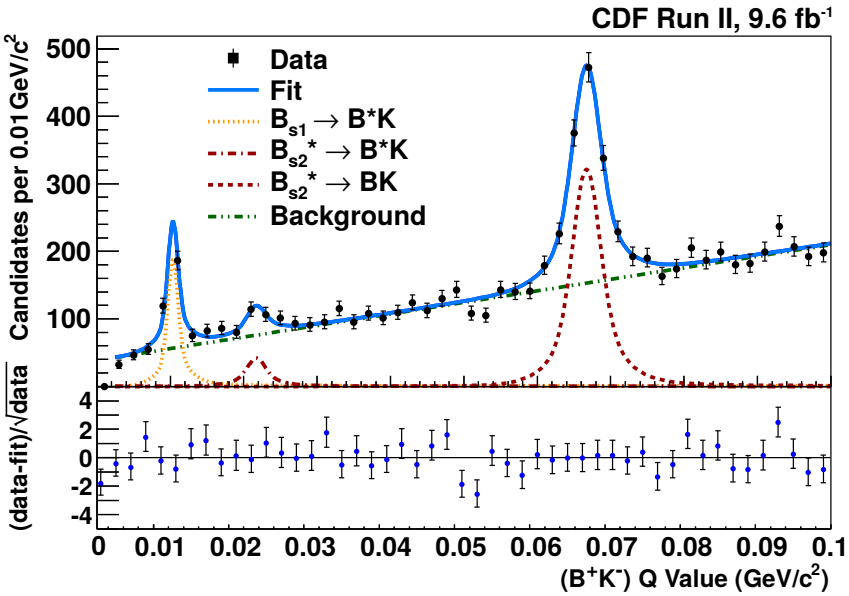

Figure 8.3.: Distribution of Q value of B^+K^- combinations with fit results overlaid summed over all decay channels. The lower part shows the deviation of the yields from the fit function normalized to the Poisson uncertainty of the data.

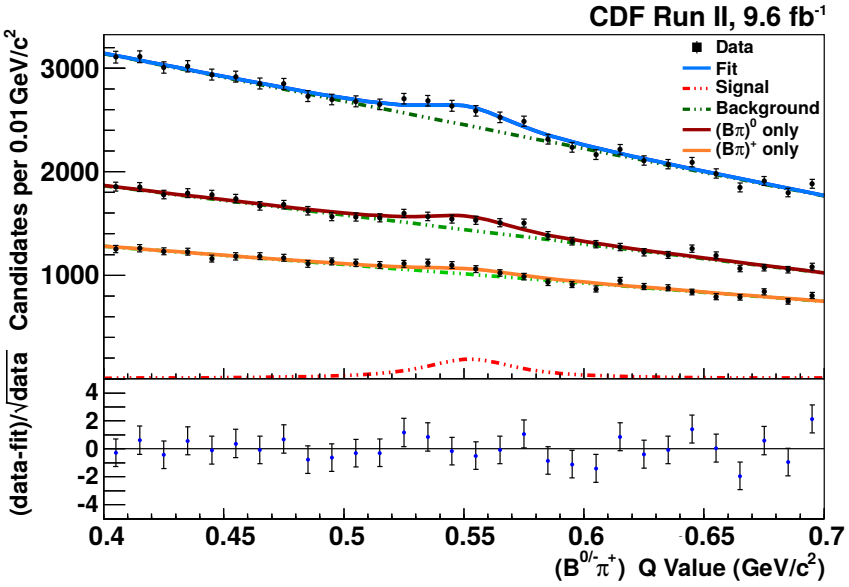

Figure 8.4.: Combined Q-value spectrum of $B^+\pi^-$ and $B^0\pi^+$ combinations with fit results overlaid summed over all decay channels. The lower part shows the deviation of the yields from the fit function normalized to the Poisson uncertainty of the data.

Table 8.6.: Comparison of the measured quantities of excited B^0 and B^+ mesons. The statistical and systematic uncertainties are assumed to be uncorrelated. This is only an approximation in case of the systematic uncertainties, so that the numbers give a rough estimate.

Quantity	Significance of Isospin Splitting
$Q(B_1)$	0.2σ
$Q(B_2^*)$	0.1σ
$\Gamma(B_1)$	1.5σ
$\Gamma(B_2^*)$	1.5σ
r_{prod}	1.0σ
$Q(\text{B}(5970))$	0.9σ
$\Gamma(\text{B}(5970))$	0.2σ
r'_{prod}	0.2σ

discrepancy with the DØ experiment in the measurement of the B^{**0} masses. The discrepancy in the measurement of the mass difference between the B_1^0 and B_2^{*0} state increases to 4.2σ. The analysis of B_s^{**0} mesons by LHCb, which was performed at the same time as this analysis, achieves a higher precision, because it benefits from a larger data set at the LHC with a signal yield three times as high as in this analysis.

Comparing the properties of B^{**0} and B^{**+} states, isospin symmetry can be tested. As can be seen in Table 8.6, all measured quantities are consistent within 2σ.

The observation of the $B_{s2}^{*0} \to B^{*+}K^-$ transition supports the interpretation of the three signal peaks, because its offset in Q value from the $B_{s2}^{*0} \to B^+K^-$ peak matches the expected amount of 45 MeV/c^2. Theory suggests that the $B(5970)$ resonance is a radial or orbital excitation of B mesons.

As a cross check for the constraint on the relative branching fraction r_{dec} made in the B^{**}-meson fits, the calculated value of the relative branching fraction of the B_{s2}^{*0} state $r_{\text{dec}} = 0.08 \pm 0.02$ (section 6.2.1) is compared to the measured value in Table 8.2. Both values are in good agreement, which supports the model used to calculate r_{dec}.

A comparison of the theoretical predictions in section 2.3 with the measured $B_{(s)}^{**}$-meson masses is presented in Fig. 8.9 and 8.10. A comparison of the widths is shown in Fig. 8.11 and 8.12.

The measured B^{**} masses are well described by the HQET calculations in Ref. [11] and [12] within a deviation of 5 MeV/c^2. The QCD string predictions in Ref. [19] describe data up to a deviation of about 10 MeV/c^2. The lattice calculation in Ref. [13] predicts the B_1 mass within the given uncertainty, while the predicted B_2^* mass deviates from the measured value by 1.2 times the theoretical uncertainty.

The predictions of the other models deviate by at least 25 MeV/c^2 from the measurement.

The measured B_s^{**0} masses are described by HQET [11, 12] and HQS [17] within 6 MeV/c^2 or less. The results of lattice calculations in Ref. [13] are consistent with this measurement within the theoretical uncertainty. Other predictions do not describe the measurement within at least 20 MeV/c^2.

Due to the different results in the width measurements of the B_1^0 and B_1^+ state, no theoretical models can be excluded. The B_2^* width is well described by two HQET models [9, 10] and the potential model [16].

The width of the two measured orbitally excited B_s^0 states are overestimated by all models except for the potential model [16].

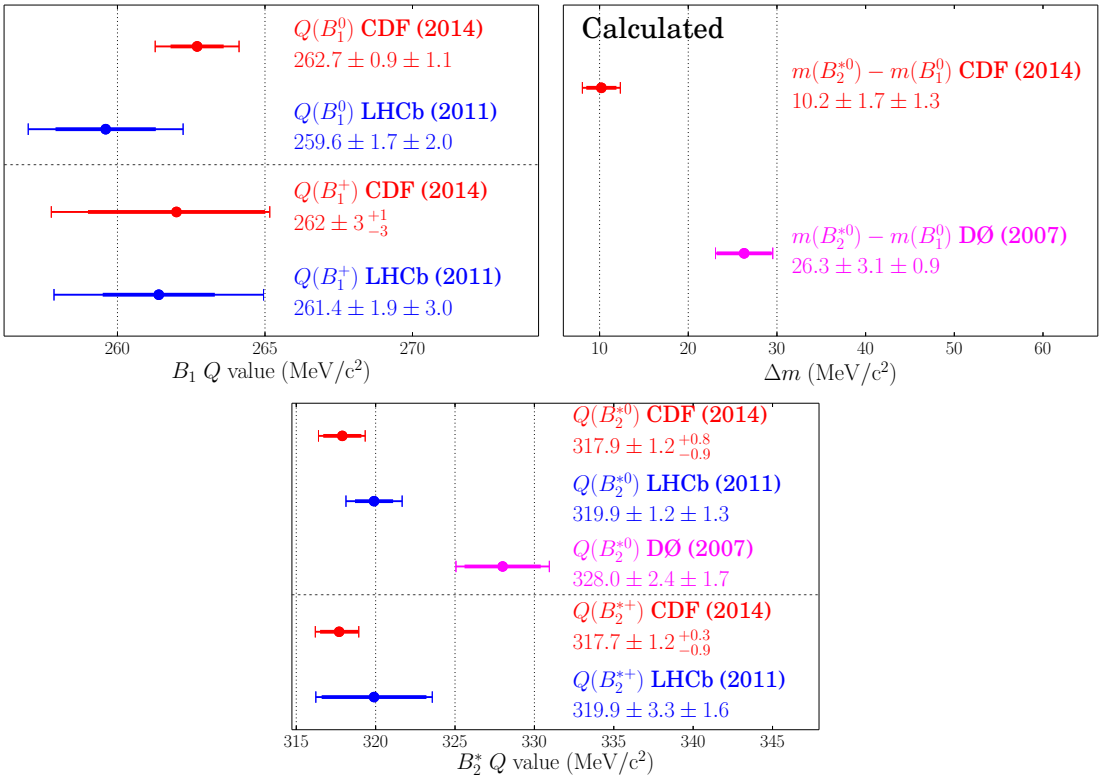

Figure 8.5.: Comparison of the measurement of B^{**} Q-meson values to results by DØ and preliminary results by LHCb.

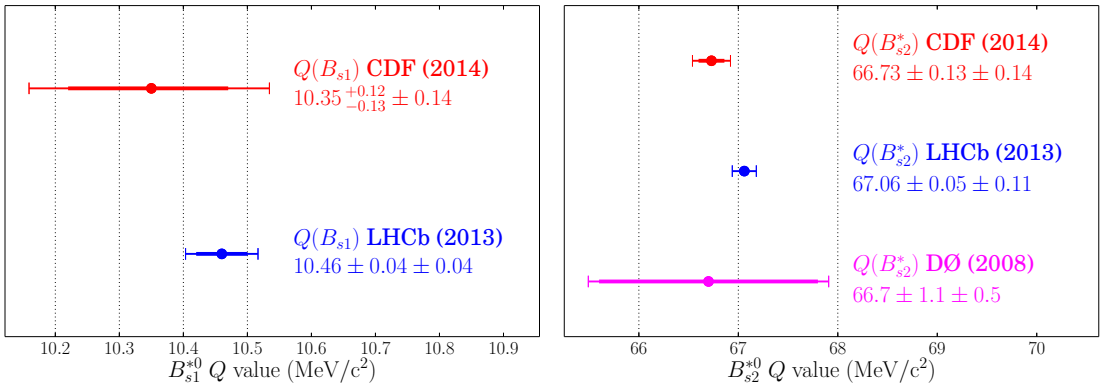

Figure 8.6.: Comparison of the measurement of B_s^{**0} Q-meson values to results by DØ and preliminary results by LHCb.

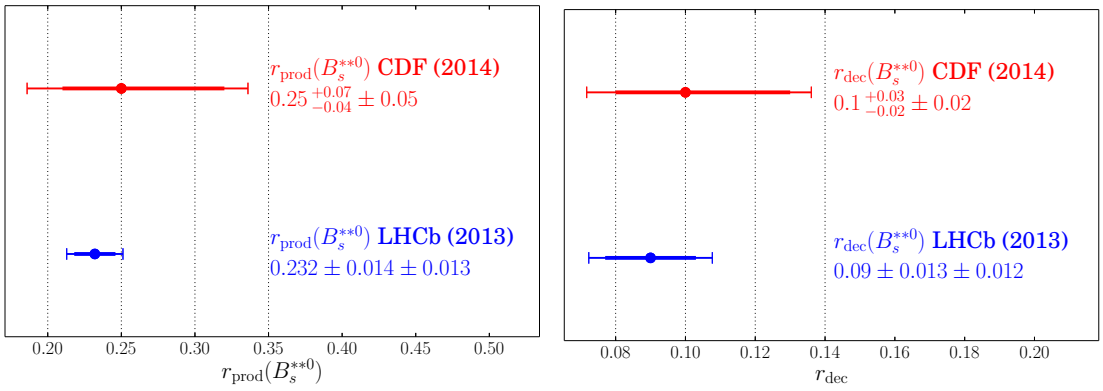

Figure 8.7.: Comparison of the measurement of relative production rates and branching fractions of B_s^{**0} mesons to recent results by LHCb.

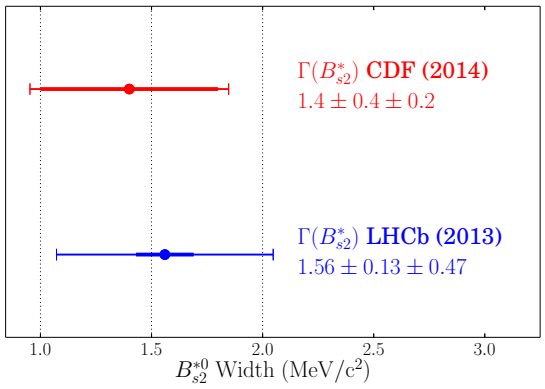

Figure 8.8.: Comparison of the B_{s2}^{*0}-meson width measurement to recent results by LHCb.

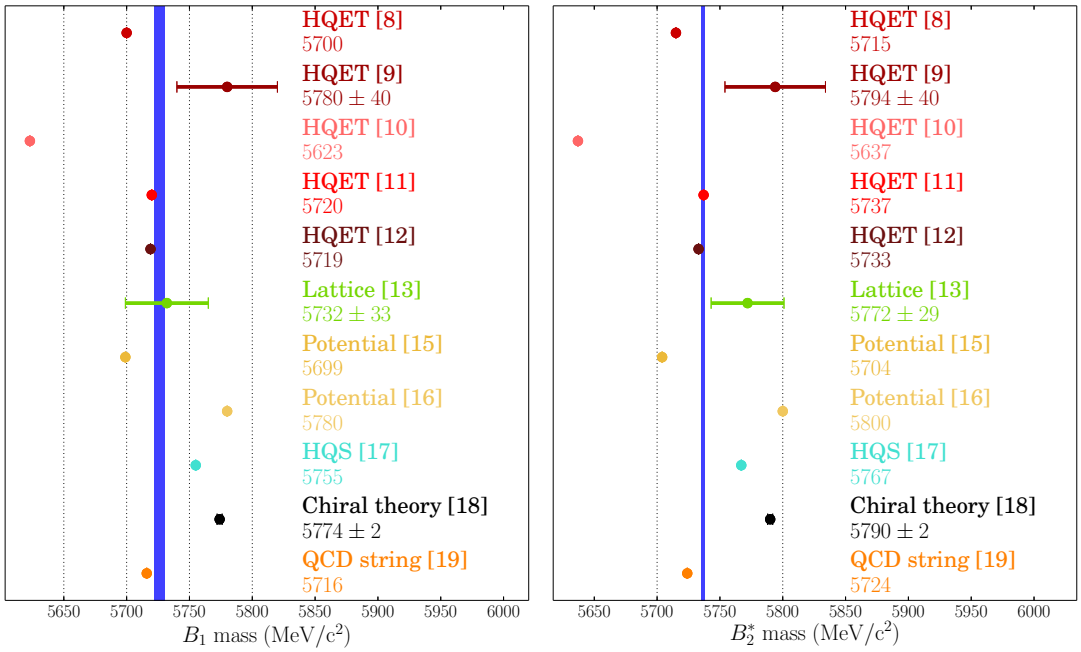

Figure 8.9.: Comparison of theoretical predictions to the measured mass of B_1 and B_2^* mesons. Measured results for both neutral and charged states are shown as blue bands together with their uncertainties, but cannot be distinguished at this scale.

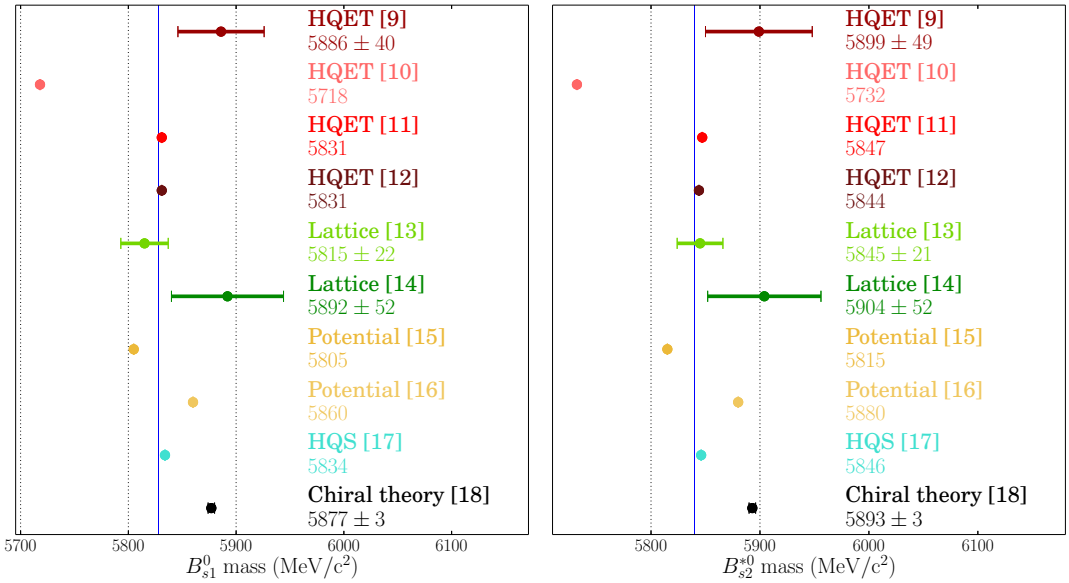

Figure 8.10.: Comparison of theoretical predictions to the measured mass of B_{s1}^0 and B_{s2}^{*0} mesons. The uncertainty of the measurement shown as blue bands is hardly visible at this scale.

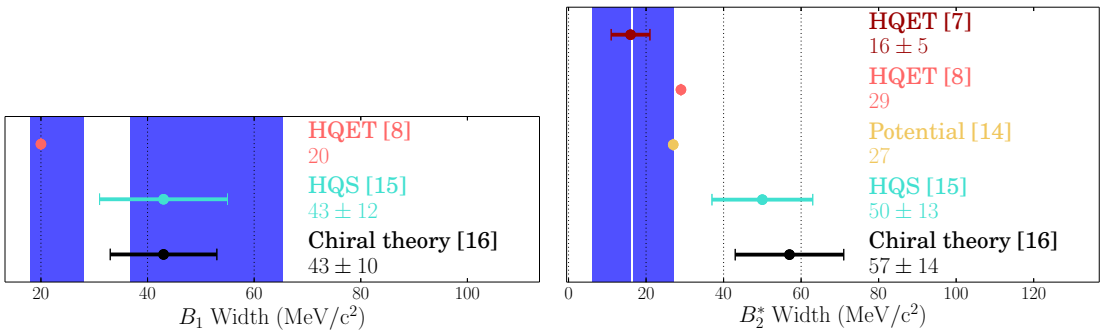

Figure 8.11.: Comparison of theoretical predictions to the measured widths of B_1 and B_2^* mesons. Measured results for both neutral and charged states are shown as blue bands together with their uncertainties.

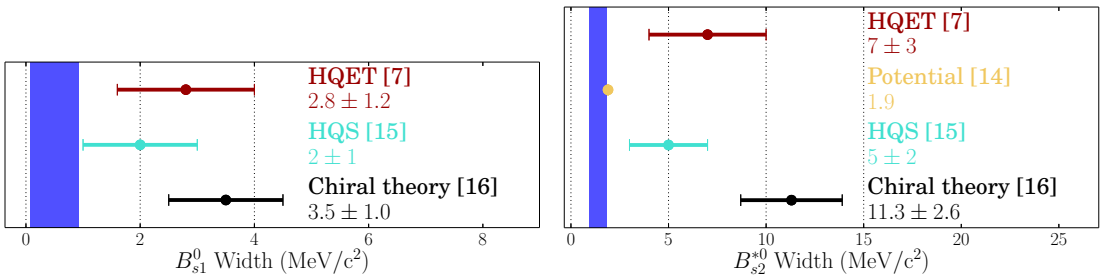

Figure 8.12.: Comparison of theoretical predictions to the measured mass of B_{s1}^0 and B_{s2}^{*0} mesons. Measured results are shown as blue bands together with their uncertainties.

9. Summary and Conclusion

In this thesis, the study of excited B^0, B^+ and B_s^0 mesons is presented, providing a test for predictions made by quantum chromodynamics. Data corresponding to an integrated luminosity of 9.6 fb^{-1} of proton-antiproton collisions at the Tevatron recorded by the CDF II detector are analyzed. Excited B^0 mesons are reconstructed in the decays to $B^{*+}\pi^-$ and $B^+\pi^-$ combinations, B^+ mesons in the decays to $B^{*0}\pi^+$ and $B^0\pi^+$ combinations, and B_s^0 mesons in the decays to $B^{*+}K^-$ and B^+K^- combinations.

The Q-value spectrum of candidates for excited B_s^0 mesons shows three peaks, interpreted as the three allowed transitions of the two narrow orbitally excited states B_{s1}^0 and B_{s2}^{*0}. The same structure is assumed for the signal in the Q-value spectra of B^0 and B^+-mesons candidates, where at higher masses an excess over the expected background is observed for the first time. It is interpreted as a new $B\pi$ resonance, which could be a radial or orbital excitation of a B meson. It is therefore called $B(5970)$.

The presented results include the most precise determination of the properties of the narrow orbitally excited B^0-meson states, the first measurement of orbitally excited B^{**+} mesons and first evidence for the $B(5970)$ resonance, as well as the measurement of its properties.

For each of the three investigated flavors of $B_{(s)}$ mesons, the mass and width is determined for the orbitally excited B_1 and B_2^* state, as well as the relative production rate r_{prod} of the B_1 state to the B_2^* state. For excited B^0 and B^+ mesons, first evidence with 4.4σ is found for the new $B(5970)$ resonance, its mass and width are measured and the relative production rate r'_{prod} to the reaction $B_2^* \to B\pi$ is determined. The results are summarized in Table 9.1. The relative branching fraction of the two B_{s2}^{*0} decays is measured to be

$$\frac{\mathcal{B}(B_{s2}^{*0} \to B^{*+}K^-)}{\mathcal{B}(B_{s2}^{*0} \to B^+K^-)} = 0.10\ ^{+0.03}_{-0.02}(\text{stat}) \pm 0.02(\text{syst}).$$

The combined production rate of the B_1^0 and B_2^{*0} states relative to the B^+ meson is determined to be $19 \pm 2\,(\text{stat}) \pm 4\,(\text{syst})\,\%$. The presented results have been published in the article:

T. Aaltonen *et al.* (CDF-Kollaboration),
"Study of orbitally excited B mesons and evidence for a new $B\pi$ resonance",
Physical Review D **90**, 012013 (2014).

Table 9.1.: Measured masses, widths and relative production rates $r^{(\prime)}_{\text{prod}}$. The first contribution to the uncertainties is statistical, the second is systematic. If indicated, the third uncertainty is the uncertainty on the masses of the daughter particles.

	m (MeV/c^2)	Γ (MeV/c^2)	$r^{(\prime)}_{\text{prod}}$
B_1^0	$5726.6 \pm 0.9\ ^{+1.1}_{-1.2} \pm 0.4$	$23 \pm 3 \pm 4$	$1.0\ ^{+0.2}_{-0.4} \pm 0.5$
B_2^{*0}	$5736.7 \pm 1.2\ ^{+0.8}_{-0.9} \pm 0.2$	$22\ ^{+\ 3}_{-\ 2}\ ^{+\ 4}_{-\ 5}$	
B_1^+	$5727\ \ \pm 3\ \ ^{+1}_{-3}\ \pm 2$	$49\ ^{+12}_{-10}\ ^{+\ 2}_{-13}$	$2.7\ ^{+1.6}_{-1.0}\ ^{+0.9}_{-1.2}$
B_2^{*+}	$5736.9 \pm 1.2\ ^{+0.3}_{-0.9} \pm 0.2$	$11\ ^{+\ 4}_{-\ 3}\ ^{+\ 3}_{-\ 4}$	
B_{s1}^0	$5828.3 \pm 0.1 \pm 0.2 \pm 0.4$	$0.5 \pm 0.3 \pm 0.3$	$0.25^{+0.07}_{-0.04} \pm 0.05$
B_{s2}^{*0}	$5839.7 \pm 0.1 \pm 0.1 \pm 0.2$	$1.4 \pm 0.4 \pm 0.2$	
$B(5970)^0$	$5978 \pm 5 \pm 12$	$70\ ^{+30}_{-20} \pm 30$	$0.5\ ^{+0.2}_{-0.1}\ ^{+\ 0.4}_{-\ 0.3}$
$B(5970)^+$	$5961 \pm 5 \pm 12$	$60\ ^{+30}_{-20} \pm 40$	$0.7\ ^{+0.3}_{-0.2} \pm 0.8$

Theoretical predictions, using several different models, of masses and widths of the orbitally excited states are compared to the measured quantities. Approaches with a good performance include Heavy Quark Effective Theory or lattice-gauge calculations. The measurement is compatible with isospin symmetry. A more detailed interpretation if the results is given in chapter 8 of this thesis.

In the last ten years, the CDF II experiment generated substantial progress in the field of $B_{(s)}$-meson spectroscopy. With this analysis of its full data set, its potential on this topic is fully exploited. To complete the picture of the lowest orbital excitations of $B_{(s)}$ mesons, the two expected broad states need to be observed. Further investigation of the new $B(5970)$ resonance is in order to reveal its quantum numbers and possible substructure. This can be done at the experiments at the LHC, where much larger data sets will be available in the future.

A. EvtGen Decay Tables [3]

Table for Decays of B^{**0} Mesons with $B^+ \to \overline{D}^0\pi^+$

```
Decay B_s2*0
.2      B+  pi-                          PHSP;
Enddecay
Decay anti-B_s2*0
.2      B-  pi+                          PHSP;
Enddecay
#------------------------------------------------------------------
Decay B+
 1.0000       anti-D0    pi+           PHSP;
Enddecay
Decay B-
1.0000        D0         pi-           PHSP;
Enddecay
#------------------------------------------------------------------
Decay anti-D0
 1.0000   K+  pi-                      PHSP;
Enddecay
Decay D0
 1.0000   K-  pi+                      PHSP;
Enddecay
#------------------------------------------------------------------
End
```

Table for Decays of B^{**0} Mesons with $B^+ \to \overline{D}^0\pi^+\pi^+\pi^-$

```
Decay B_2*0
 .2      B+  pi-                          PHSP;
Enddecay
Decay anti-B_2*0
 .2      B-  pi+                          PHSP;
Enddecay
#------------------------------------------------------------------
Decay B+
```

```
 0.1000       anti-D0    pi+ pi+ pi-   PHSP;
 0.9000       a_1+      anti-D0        SVS;
Enddecay
Decay B-
 0.1000        D0         pi+ pi- pi-   PHSP;
 0.9000        a_1-       D0            SVS;
Enddecay
#-------------------------------------------------------------------
Decay anti-D0
 1.0000   K+  pi-                      PHSP;
Enddecay
Decay D0
 1.0000   K-  pi+                      PHSP;
Enddecay
#-------------------------------------------------------------------
Decay a_1+
 1.0000   rho0  pi+  VVS_PWAVE  0.9091 0.0 0.0 0.0 -0.0909 0.0;
Enddecay
#-------------------------------------------------------------------
Decay a_1-
 1.0000   rho0  pi-  VVS_PWAVE  0.9091 0.0 0.0 0.0 -0.0909 0.0;
Enddecay
#-------------------------------------------------------------------
Decay rho0
 1.0000   pi+ pi-  VSS;
Enddecay
#-------------------------------------------------------------------
End
```

Table for Decays of B^{**0} Mesons with $B^+ \to J/\psi K^+$

```
Decay B_2*0
1.0000      B+  pi-                         PHSP;
Enddecay
Decay anti-B_2*0
1.0000      B-  pi+                         PHSP;
Enddecay
#-------------------------------------------------------------------
Decay B+
 1.0000       J/psi         K+           PHSP;
Enddecay
Decay B-
```

```
1.0000        J/psi         K-            PHSP;
Enddecay
#-------------------------------------------------------------------
Decay J/psi
 1.000    mu+  mu-               PHOTOS  VLL;
Enddecay
#-------------------------------------------------------------------
End
```

Table for Decays of B^{**+} Mesons with $B^0 \to D^-\pi^+$

```
Decay B_2*+
.2      B0  pi+                          PHSP;
Enddecay
Decay B_2*-
.2      anti-B0  pi-                          PHSP;
Enddecay
#-------------------------------------------------------------------
Decay B0
 1.0000        D-      pi+              PHSP;
Enddecay
Decay anti-B0
 1.0000        D+      pi-              PHSP;
Enddecay
#-------------------------------------------------------------------
Decay D-
 1.0000   K+  pi-  pi-                  D_DALITZ;
Enddecay
Decay D+
 1.0000   K-  pi+  pi+                  D_DALITZ;
Enddecay
#-------------------------------------------------------------------
End
```

Table for Decays of B^{**+} Mesons with $B^0 \to D^-\pi^+\pi^+\pi^-$

```
Decay B_2*+
 0.75      B0   pi+                        PHSP;
 0.25      B*0  pi+                        PHSP;
Enddecay
Decay B_2*-
 0.75      anti-B0   pi-                         PHSP;
```

```
 0.25      anti-B*0  pi-                          PHSP;
Enddecay
#-------------------------------------------------------------------
#Decay B*+
#1.0000    B+  gamma                          VSP_PWAVE;
#Enddecay
#Decay B*-
#1.0000    B-  gamma                          VSP_PWAVE;
#Enddecay
Decay B*0
1.0000    B0  gamma                         VSP_PWAVE;
Enddecay
Decay anti-B*0
1.0000    anti-B0 gamma                        VSP_PWAVE;
Enddecay
#-------------------------------------------------------------------
Decay B0
 1.0000        D-      pi+ pi+ pi-             PHSP;
Enddecay
Decay anti-B0
 1.0000        D+      pi- pi+ pi-             PHSP;
Enddecay
#-------------------------------------------------------------------
Decay D-
 1.0000   K+  pi-  pi-                  D_DALITZ;
Enddecay
Decay D+
 1.0000   K-  pi+  pi+                  D_DALITZ;
Enddecay
#-------------------------------------------------------------------
End
```

Table for Decays of B^{**+} Mesons with $B^0 \to J/\psi K^{*0}$

```
Decay B_2*+
 0.75      B0   pi+                          PHSP;
 0.25      B*0  pi+                          PHSP;
Enddecay
Decay B_2*-
 0.75      anti-B0   pi-                          PHSP;
 0.25      anti-B*0  pi-                          PHSP;
Enddecay
```

```
#-----------------------------------------------------------------
Decay B*0
1.0000    B0  gamma                          VSP_PWAVE;
Enddecay
Decay anti-B*0
1.0000    anti-B0 gamma                          VSP_PWAVE;
Enddecay
#-----------------------------------------------------------------
Decay B0
 1.0000       J/psi         K*0          PHSP;
Enddecay
Decay anti-B0
 1.0000       J/psi         anti-K*0     PHSP;
Enddecay
#-----------------------------------------------------------------
Decay J/psi
 1.000    mu+  mu-               PHOTOS  VLL;
Enddecay
#-----------------------------------------------------------------
Decay K*0
 1.000       K+         pi-          PHSP;
Enddecay
Decay anti-K*0
 1.000       K-         pi+          PHSP;
Enddecay
End
```

Table for Decays of B^{**+} Mesons with $B^0 \to J/\psi K^{*0}$

```
Decay B_2*+
 0.75      B0   pi+                          PHSP;
 0.25      B*0  pi+                          PHSP;
Enddecay
Decay B_2*-
 0.75      anti-B0   pi-                          PHSP;
 0.25      anti-B*0  pi-                          PHSP;
Enddecay
#-----------------------------------------------------------------
Decay B*0
1.0000    B0  gamma                          VSP_PWAVE;
Enddecay
Decay anti-B*0
```

```
1.0000    anti-B0 gamma                        VSP_PWAVE;
Enddecay
#------------------------------------------------------------------
Decay B0
 1.0000       J/psi         K_S0          PHSP;
Enddecay
Decay anti-B0
 1.0000       J/psi         K_S0     PHSP;
Enddecay
#------------------------------------------------------------------
Decay J/psi
 1.000    mu+  mu-               PHOTOS  VLL;
Enddecay
#------------------------------------------------------------------
Decay K_S0
 1.000       pi+         pi-          PHSP;
Enddecay
End
```

Table for Decays of B_s^{**} Mesons with $B^+ \to \overline{D}^0 \pi^+$

```
Decay B_s2*0
.2      B+  K-                          PHSP;
Enddecay
Decay anti-B_s2*0
.2      B-  K+                          PHSP;
Enddecay
#------------------------------------------------------------------
Decay B+
 1.0000       anti-D0    pi+           PHSP;
Enddecay
Decay B-
1.0000        D0         pi-           PHSP;
Enddecay
#------------------------------------------------------------------
Decay anti-D0
 1.0000   K+  pi-                      PHSP;
Enddecay
Decay D0
 1.0000   K-  pi+                      PHSP;
Enddecay
End
```

Table for Decays of B_s^{**} Mesons with $B^+ \to \overline{D}^0\pi^+\pi^+\pi^-$

```
Decay B_s2*0
 .2      B+  K-                          PHSP;
Enddecay
Decay anti-B_s2*0
 .2      B-  K+                          PHSP;
Enddecay
#-------------------------------------------------------------------
Decay B+
 0.1000       anti-D0    pi+ pi+ pi-    PHSP;
 0.9000       a_1+      anti-D0         SVS;
Enddecay
Decay B-
 0.1000        D0         pi+ pi- pi-    PHSP;
 0.9000        a_1-       D0             SVS;
Enddecay
#-------------------------------------------------------------------
Decay anti-D0
 1.0000   K+  pi-                        PHSP;
Enddecay
Decay D0
 1.0000   K-  pi+                        PHSP;
Enddecay
#-------------------------------------------------------------------
Decay a_1+
 1.0000   rho0  pi+  VVS_PWAVE  0.9091 0.0 0.0 0.0 -0.0909 0.0;
Enddecay
#-------------------------------------------------------------------
Decay a_1-
 1.0000   rho0  pi-  VVS_PWAVE  0.9091 0.0 0.0 0.0 -0.0909 0.0;
Enddecay
#-------------------------------------------------------------------
Decay rho0
 1.0000   pi+ pi-  VSS;
Enddecay
#-------------------------------------------------------------------
End
```

Table for Decays of B_s^{**} Mesons with $B^+ \to J/\psi K^+$

```
Decay B_s2*0
1.0000      B+  K-                          PHSP;
Enddecay
Decay anti-B_s2*0
1.0000      B-  K+                          PHSP;
Enddecay
#-------------------------------------------------------------------
Decay B+
 1.0000       J/psi         K+           PHSP;
Enddecay
Decay B-
1.0000        J/psi         K-           PHSP;
Enddecay
#-------------------------------------------------------------------
Decay J/psi
 1.000    mu+  mu-               PHOTOS  VLL;
Enddecay
#-------------------------------------------------------------------
End
```

B. B-Candidate Mass Fits

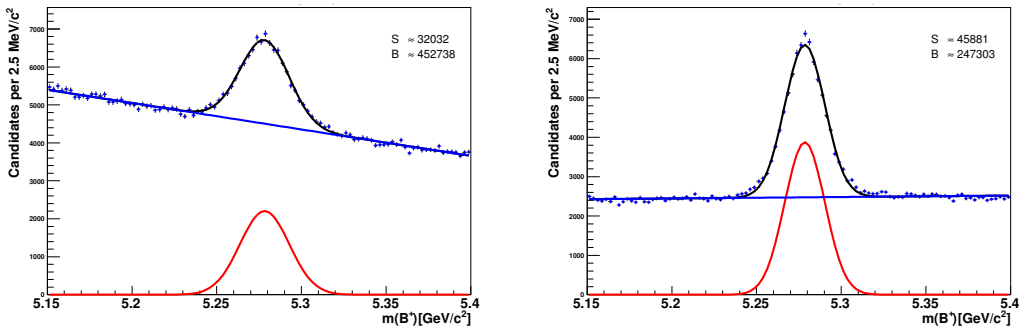

Figure B.1.: Fit to the reconstructed B^+-candidate mass spectrum in the decay channels $B^+ \to \overline{D}^0\pi^+\pi^+\pi^-$(left) and $B^+ \to J/\psi K^+$(right). [3]

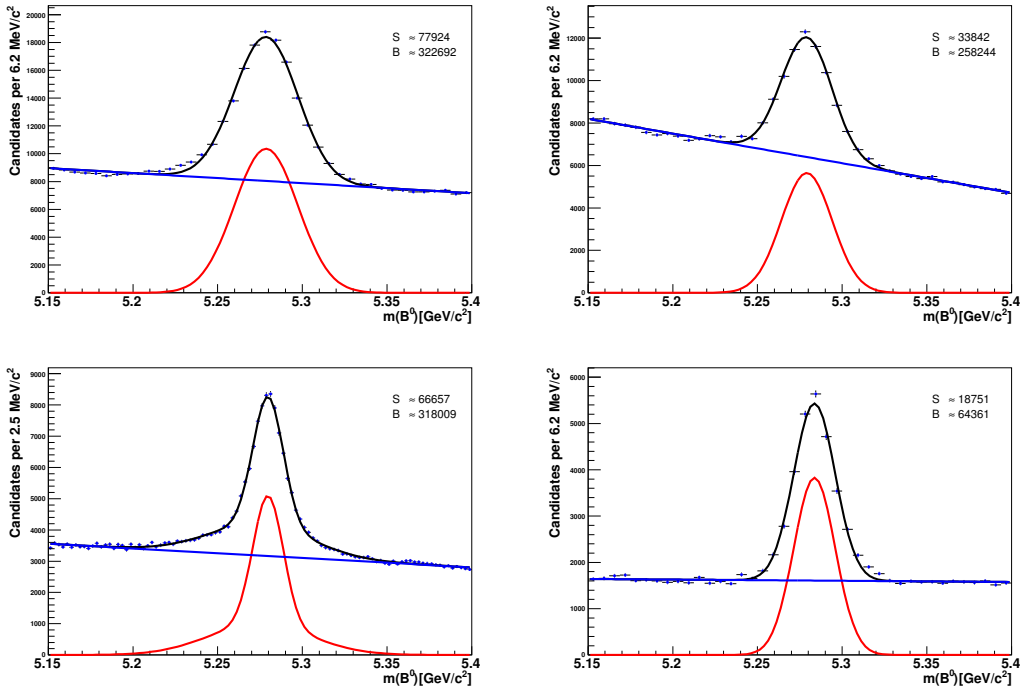

Figure B.2.: Fit to the reconstructed B^0-candidate mass spectrum in the decay channels $B^0 \to D^-\pi^+$(top left), $B^0 \to D^-\pi^+\pi^+\pi^-$(top right), $B^0 \to J/\psi K^{*0}$(bottom left) and $B^0 \to J/\psi K_s^0$(bottom right). [3]

C. NeuroBayes-Training Variables

B-Meson NeuroBayes Trainings

Table C.1.: List of variables in the $B^+ \to \overline{D}^0\pi^+\pi^+\pi^-$ NeuroBayes training. [3]

	Name	No.	Add. Signi.	Used
1.	B.Chi23D	16	214.05	yes
2.	3Pi.Mass	25	186.28	yes
3.	BPi3.psD0Signi	23	95.78	yes
4.	BPi1.psD0Signi	18	89.33	yes
5.	DKPID.ratioKaon	3	84.11	yes
6.	B.D0	15	74.78	yes
7.	DPC.lxyWrtP	13	68.11	yes
8.	BPi2.psD0Signi	21	67.79	yes
9.	BPi3PC.helA	24	55.42	yes
10.	DPC.cmsAWrtP	12	44.15	yes
11.	D.Pt	8	47.26	yes
12.	D.LxySigni	9	38.56	yes
13.	BPi3.Pt	22	34.84	yes
14.	BPi1PC.helA	19	26.29	yes
15.	DKPC.helA	6	25.78	yes
16.	DK.Pt	2	15.36	yes
17.	D.Mass	10	15.36	yes
18.	BPi2.Pt	20	15.06	yes
19.	B.Pt	14	6.27	yes
20.	BPi1.Pt	26	14.70	yes
21.	DPi.Pt	7	14.36	yes
22.	DKPID.ratioKaon	4	12.05	yes
23.	DKPID.pullTofKa	5	11.40	yes
24.	B.LxySigni	17	5.90	yes
25.	D.D0	11	2.20	yes

Table C.2.: List of variables in the $B^+ \to J/\psi K^+$ NeuroBayes training. [3]

	Name	No.	Add. Signi.	Used
1.	K.psD0Signi	9	297.92	yes
2.	K.Pt	8	185.87	yes
3.	B.Chi23D	15	117.55	yes
4.	KPID.ratioKaon	10	75.89	yes
5.	B.LxySigni	16	55.02	yes
6.	B.D0	13	49.15	yes
7.	KPID.pullTofKa	12	45.60	yes
8.	JPsiPC.cmsAWrtP	7	38.79	yes
9.	KPID.ratioKaon	11	19.97	yes
10.	JPsi.Chi23D	5	18.72	yes
11.	B.Pt	14	2.52	yes
12.	JPsi.Pt	3	12.58	yes
13.	JPsi.D0	4	9.19	yes
14.	Mu1.D0	2	7.61	yes
15.	JPsi.Mass	6	1.21	no

Table C.3.: List of variables in the $B^0 \to D^-\pi^+$ NeuroBayes training. [3]

	Name	No.	Add. Signi.	Used
1.	B.Chi23D	17	248.12	yes
2.	B.LxySigni	19	211.03	yes
3.	B.D0	18	126.27	yes
4.	BPi.Pt	16	106.42	yes
5.	DKPID.ratioKaon	4	95.69	yes
6.	DPi2.psD0Signi	8	79.66	yes
7.	DPC.lzWrtP	15	63.35	yes
8.	D.Mass	13	44.88	yes
9.	DK.Pt	2	43.09	yes
10.	D.LxySigni	12	33.43	yes
11.	DPi2.Pt	7	24.96	yes
12.	DPi1.Pt	6	19.36	yes
13.	B.Pt	20	25.95	yes
14.	D.Chi23D	10	21.66	yes
15.	D.D0	11	13.49	yes
16.	D.Pt	9	14.24	yes
17.	DPC.lxyWrtP	14	6.50	yes
18.	DK.Pt	3	3.38	yes
19.	DKPID.ratioKaon	5	2.26	yes

Table C.4.: List of variables in the $B^0 \to D^-\pi^+\pi^+\pi^-$ NeuroBayes training. [3]

	Name	No.	Add. Signi.	Used
1.	Pi3Vtx.Mass	22	210.87	yes
2.	B.Chi23D	26	168.37	yes
3.	DPi2.psD0Signi	9	122.36	yes
4.	DPC.lxyWrtP	14	80.41	yes
5.	DPC.cmsAWrtP	13	62.82	yes
6.	BPi3.psD0Signi	21	66.86	yes
7.	DKPID.ratioKaon	4	54.36	yes
8.	BPi2.psD0Signi	19	47.89	yes
9.	B.D0	25	46.19	yes
10.	BPi1.psD0Signi	16	39.28	yes
11.	D.Mass	12	28.28	yes
12.	BPi1PC.helA	17	26.17	yes
13.	DK.Pt	2	20.52	yes
14.	BPi3.Pt	20	21.44	yes
15.	BPi1.Pt	15	17.03	yes
16.	DPi2.Pt	8	15.47	yes
17.	DPi1.Pt	6	11.81	yes
18.	B.Pt	24	15.21	yes
19.	BPi2.Pt	18	16.03	yes
20.	DK.psD0Signi	3	15.84	yes
21.	DPi1.psD0Signi	7	13.73	yes
22.	D.Pt	10	9.13	yes
23.	DKPID.ratioKaon	5	5.76	yes
24.	D.D0	11	2.58	yes
25.	B.LxySigni	27	1.11	no
26.	Pi3VtxPC.lxyWrtP	23	0.90	no

Table C.5.: List of variables in the $B^0 \to J/\psi K^{*0}$ NeuroBayes training. [3]

	Name	No.	Add. Signi.	Used
1.	KS.Pt	26	324.88	yes
2.	Pi.psD0Signi	25	225.40	yes
3.	B.Chi23D	36	148.38	yes
4.	KS.Mass	31	121.01	yes
5.	K.psD0Signi	21	103.04	yes
6.	KPID.ratioKaon	22	84.58	yes
7.	B.LxySigni	37	50.76	yes
8.	B.D0	35	39.35	yes
9.	Pi.Pt	24	38.45	yes
10.	KSPC.lxyWrtP	33	23.12	yes
11.	Jpsi.LxySigni	14	22.08	yes
12.	JpsiPC.cmsAWrtP	16	19.74	yes
13.	Jpsi.Chi23D	13	18.76	yes
14.	KSPC.dxyWrtP	32	17.46	yes
15.	Jpsi.D0	12	16.78	yes
16.	KPID.ratioKaon	23	15.54	yes
17.	JpsiPC.lxyWrtP	18	13.15	yes
18.	JpsiPC.lzWrtP	19	12.52	yes
19.	K.Pt	20	9.68	yes
20.	Mu1.D0	3	4.19	yes
21.	Mu1.psD0Signi	4	8.46	yes
22.	Mu2.psD0Signi	9	7.18	yes
23.	Mu2.D0	8	7.15	yes
24.	KS.LxySigni	30	6.40	yes
25.	Mu1.Pt	2	4.92	yes
26.	B.Pt	34	5.67	yes
27.	Mu2PID.ratioMuon	11	5.33	yes
28.	Mu2.Pt	7	4.96	yes
29.	KS.D0	27	3.72	yes
30.	Mu2PID.ratioMuon	10	3.39	yes
31.	Mu1PID.ratioMuon	5	3.28	yes
32.	Jpsi.Mass	15	2.15	yes
33.	JpsiPC.dxyWrtP	17	2.05	yes
34.	KS.Chi23D	29	1.81	no
35.	Mu1PID.ratioMuon	6	1.31	no
36.	KS.Chi2RPhi	28	0.20	no

Table C.6.: List of variables in the $B^0 \to J/\psi K_s^0$ NeuroBayes training. [3]

	Name	No.	Add. Signi.	Used
1.	JpsiPC.lxyWrtP	8	96.42	yes
2.	B.D0	15	121.67	yes
3.	Ks.Pt	11	79.86	yes
4.	B.Chi23D	16	65.90	yes
5.	Mu2.psD0Signi	4	43.71	yes
6.	Mu1PC.helA	3	34.13	yes
7.	JpsiPC.dxyWrtP	7	30.56	yes
8.	Ks.Mass	13	24.41	yes
9.	Mu1.psD0Signi	2	19.31	yes
10.	Ks.LxySigni	12	15.87	yes
11.	Jpsi.Mass	6	11.35	yes
12.	KsPC.cmsAWrtP	14	10.96	yes
13.	Pi2PC.helA	10	10.81	yes
14.	Pi1.Pt	20	11.28	yes
15.	Pi1PC.helA	9	9.05	yes
16.	B.LxySigni	17	7.59	yes
17.	Pi2.Pt	21	7.14	yes
18.	Jpsi.D0	5	5.65	yes
19.	Jpsi.LxySigni	19	4.66	yes
20.	B.Pt	18	3.23	yes

$B^{**}_{(s)}$-Meson NeuroBayes Trainings

Table C.7.: List of variables in the B^{**0}-meson NeuroBayes training with the further decay $B^+ \to \overline{D}^0 \pi^+ \pi^+ \pi^-$.

	Name	No.	Add. Signi.	Used
1.	BSPi.D0Signi	5	117.72	yes
2.	BNN.nbout	11	56.04	yes
3.	BSPi.Pt	4	46.45	yes
4.	B.Mass	2	36.77	yes
5.	BSPiPID.pullTofPi	7	31.09	yes
6.	BPC.cmsAWrtP	3	14.73	yes
7.	BSPiPID.ratioPion	8	8.45	yes
8.	BS.Pt	10	8.10	yes
9.	BSPiPID.ratioPion	9	7.60	yes
10.	BSPi.Eta	6	6.45	yes

Table C.8.: List of variables in the B^{**0}-meson NeuroBayes training with the further decay $B^+ \to J/\psi K^+$.

	Name	No.	Add. Signi.	Used
1.	BSPi.psD0Signi	5	296.11	yes
2.	BSPiPID.pullTofPi	6	126.83	yes
3.	BSPi.Pt	4	106.74	yes
4.	B.Mass	2	80.65	yes
5.	BNN.nbout	10	54.19	yes
6.	BPC.cmsAWrtP	3	42.68	yes
7.	BSPiPID.ratioPion	8	39.98	yes
8.	BSPiPID.ratioPion	7	21.02	yes
9.	BS.Pt	9	8.09	yes

Table C.9.: List of variables in the B^{**+}-meson NeuroBayes training with the further decay $B^0 \to D^-\pi^+$.

	Name	No.	Add. Signi.	Used
1.	BSPi.D0Signi	5	166.17	yes
2.	BNN.nbout	11	69.28	yes
3.	BSPi.Pt	4	58.86	yes
4.	BSPiPID.pullTofPi	7	53.00	yes
5.	B.Mass	2	49.42	yes
6.	BPC.cmsAWrtP	3	24.48	yes
7.	BSPiPID.ratioPion	8	18.45	yes
8.	BSPi.Eta	6	10.52	yes
9.	BS.Pt	10	1.74	no
10.	BSPiPID.ratioPion	9	1.62	no

Table C.10.: List of variables in the B^{**+}-meson NeuroBayes training with the further decay $B^0 \to D^-\pi^+\pi^+\pi^-$.

	Name	No.	Add. Signi.	Used
1.	BSPi.D0Signi	5	22.29	yes
2.	BSPi.Pt	4	10.83	yes
3.	B.Mass	2	8.70	yes
4.	BSPiPID.pullTofPi	7	6.67	yes
5.	BPC.cmsAWrtP	3	2.99	yes
6.	BS.Pt	10	1.83	no
7.	BSPiPID.ratioPion	9	1.81	no
8.	BSPi.Eta	6	1.47	no
9.	BNN.nbout	11	0.93	no
10.	BSPiPID.ratioPion	8	0.61	no

Table C.11.: List of variables in the B^{**+}-meson NeuroBayes training with the further decay $B^0 \to J/\psi K^{*0}$.

	Name	No.	Add. Signi.	Used
1.	BSPi.D0Signi	5	239.97	yes
2.	BSPi.Pt	4	114.98	yes
3.	B.Mass	2	98.19	yes
4.	BSPiPID.pullTofPi	7	76.00	yes
5.	BNN.nbout	11	45.44	yes
6.	BSPi.Eta	6	31.30	yes
7.	BSPiPID.ratioPion	9	30.84	yes
8.	BS.Pt	10	24.03	yes
9.	BPC.cmsAWrtP	3	28.04	yes
10.	BSPiPID.ratioPion	8	6.90	yes

Table C.12.: List of variables in the B^{**+}-meson NeuroBayes training with the further decay $B^0 \to J/\psi K^0_s$.

	Name	No.	Add. Signi.	Used
1.	BSPi.D0Signi	5	252.04	yes
2.	BSPi.Pt	4	116.75	yes
3.	BSPiPID.pullTofPi	6	91.35	yes
4.	B.Mass	2	54.96	yes
5.	BSPiPID.ratioPion	8	31.35	yes
6.	BNN.nbout	10	28.24	yes
7.	BPC.cmsAWrtP	3	28.94	yes
8.	BS.Pt	9	23.16	yes
9.	BSPiPID.ratioPion	7	13.06	yes

Table C.13.: List of variables in the B_s^{**0}-meson NeuroBayes training with the further decay $B^+ \to \overline{D}^0 \pi^+$.

	Name	No.	Add. Signi.	Used
1.	BSKPID.ratioKaon	7	181.38	yes
2.	BSK.psD0Signi	5	146.28	yes
3.	BSK.Pt	4	63.34	yes
4.	BNN.nbout	10	43.05	yes
5.	B.Mass	2	33.06	yes
6.	BSKPID.pullTofKa	6	30.42	yes
7.	BSKPID.ratioKaon	8	10.98	yes
8.	BPC.cmsAWrtP	3	7.61	yes
9.	BS.Pt	9	1.95	no

Table C.14.: List of variables in the B_s^{**0}-meson NeuroBayes training with the further decay $B^+ \to \overline{D}^0 \pi^+ \pi^+ \pi^-$.

	Name	No.	Add. Signi.	Used
1.	BSK.psD0Signi	5	83.72	yes
2.	BSKPID.ratioKaon	7	61.62	yes
3.	BNN.nbout	10	36.39	yes
4.	B.Mass	2	26.33	yes
5.	BSK.Pt	4	17.73	yes
6.	BS.Pt	9	7.95	yes
7.	BSKPID.pullTofKa	6	7.04	yes
8.	BPC.cmsAWrtP	3	1.43	no
9.	BSKPID.ratioKaon	8	0.82	no

Table C.15.: List of variables in the B_s^{**0}-meson NeuroBayes training with the further decay $B^+ \to J/\psi K^+$.

	Name	No.	Add. Signi.	Used
1.	BSK.psD0Signi	5	340.57	yes
2.	BSKPID.ratioKaon	7	269.11	yes
3.	BSK.Pt	4	132.74	yes
4.	BNN.nbout	10	101.05	yes
5.	BSKPID.pullTofKa	6	73.57	yes
6.	B.Mass	2	53.23	yes
7.	BSKPID.ratioKaon	8	43.23	yes
8.	BPC.cmsAWrtP	3	6.73	yes
9.	BS.Pt	9	12.05	yes

Bibliography

[1] T. Aaltonen *et al.* (CDF-Kollaboration), "Study of orbitally excited B mesons and evidence for a new $B\pi$ resonance", Physical Review D **90**, 012013 (2014).

[2] K.A. Olive *et al.* (Particle Data Group), Chin. Phys. C, **38**, 090001 (2014).

[3] Manuel Kambeitz, "Spectroscopy of Orbitally Excited B Mesons with the CDF II Detector", Diploma thesis, IEKP-KA/2011-38.

[4] Wikimedia Commons: `http://en.wikipedia.org/wiki/File:Standard_Model_of_Elementary_Particles.svg`, accessed August 5, 2014 and modified.

[5] Andreas Gessler, "Search for Orbitally Excited B Mesons with the CDF II Detector", PhD thesis, IEKP-KA/2009-21.

[6] Martin Heck, "Spectroscopy of Orbitally Excited B_s Mesons with the CDF II Detector", PhD thesis, IEKP-KA/2009-28.

[7] Benjamin Grinstein, "The static quark effective theory",Nucl. Phys. B **339**, 253, (1990).

[8] N. Isgur, "Spin-orbit inversion of excited heavy quark mesons", Phys. Rev. D **57**, 4041 (1998).

[9] A. F. Falk and T. Mehen, "Excited heavy mesons beyond leading order in the heavy quark expansion", Phys. Rev. D **53**, 231 (1996).

[10] A. H. Orsland and H. Hogaasen, "Strong and electromagnetic decays of excited heavy mesons", Eur. Phys. J. C **9**, 503 (1999).

[11] K. Sudoh, T. Matsuki, and T. Morii, "New heavy-light mesons Q anti-q", Prog. Theor. Phys. **117**, 1077 (2007).

[12] R. N. Faustov, V. O. Galkin, and D. Ebert, "Mass spectrum of orbitally and radially excited heavy-light mesons in the relativistic quark model", Phys. Rev. D **57**, 5663 (1998).

[13] R. Lewis and R. M. Woloshyn, "S- and P-wave heavy-light mesons in lattice nonrelativistic QCD", Phys. Rev. D **62**, 114507 (2000).

[14] A. M. Green, J. Koponen, C. Michael, C. McNeile, and G. Thompson (UKQCD Collaboration), "Excited B mesons from the lattice", Phys. Rev. D **69**, 094505 (2004).

[15] C. J. Nyfält, T. A. Lähde, and D. O. Riska, "Spectra and M1 Decay Widths of Heavy-Light Mesons", Nucl. Phys. A **674**, 141 (2000).

[16] S. Godfrey and R. Kokoski, "Properties of P-wave mesons with one heavy quark", Phys. Rev. D **43**, 1679 (1991).

[17] E. J. Eichten, C. T. Hill, and C. Quigg, "Properties of orbitally excited heavy-light (Qq^-) mesons", Phys. Rev. Lett **71**, 4116 (1993).

[18] R. Ferrandes, F. De Fazio, and P. Colangelo, Nucl. Phys. (Proc. Suppl.) **163**, 177 (2007).

[19] Yu. S. Kalashnikova and A. V. Nefediev, "Orbitally excited D and B mesons in the approach of the QCD string with quarks at the ends", Phys. Lett. B **530**, 117 (2002).

[20] P. Abreu *et al.* (DELPHI Collaboration), "Observation of orbitally excited B mesons", Phys. Lett. B **345**, 598 (1995).

[21] R. Akers *et al.* (OPAL Collaboration), Z. Phys. C **66**, 19 (1995).

[22] D. Buskulic *et al.* (ALEPH Collaboration), Z. Phys. C **69**, 393 (1996).

[23] Z. Albrecht *et al.*, "A Study of Excited b-Hadron States with the DELPHI Detector at LEP", DELPHI 2004–025 CONF 700 (2004).

[24] V. M. Abazov *et al.* (D0 Collaboration), "Properties of $L = 1$ B_1 and B_2^* Mesons", Phys. Rev. Lett. **99**, 172001 (2007).

[25] T. Aaltonen *et al.* (CDF Collaboration), "Measurement of Resonance Parameters of Orbitally Excited Narrow B^0 Mesons", Phys. Rev. Lett. **102**, 102003 (2009).

[26] R. Aaij *et al.* (LHCb Collaboration), "Observations of Orbitally Excited $B^{**}_{(s)}$ Mesons", LHCb-CONF-2011-053.

[27] T. Aaltonen *et al.* (CDF Collaboration), Phys. Rev. Lett. **100**, 082001 (2008).

[28] V. M. Abazov *et al.* (D0 Collaboration), "Observation of Orbitally Excited B_s Mesons", Phys. Rev. Lett. **100**, 082002 (2008).

[29] R. Aaij *et al.* (LHCb Collaboration), "First Observation of the Decay $B^*_{s2}(5840)^0 \to B^{*+}K^-$ and Studies of Excited B^0_s Mesons", Phys. Rev. Lett. **110**, 151803 (2013).

[30] `http://www-visualmedia.fnal.gov/VMS_Site/gallery/stillphotos/2003/0300/03-0390-13D.hr.jpg`.

[31] Felix Wick, Phd Thesis, "Charmed Baryon Spectroscopy and Search for CP Violation in $D^0 \to K^0_S\pi^+\pi^-$", IEKP-KA/2011-32.

[32] `http://www-cdf.fnal.gov/events/pic/acc.gif`.

[33] `http://www-bd.fnal.gov/pplot/FY11/01Oct11/PeakLuminosity.png`.

[34] `http://www-bd.fnal.gov/pplot/FY11/01Oct11/IntegratedLuminosity.png`.

[35] CDF Collaboration, "The CDF II Detector Technical Design Report", FERMILAB-Pub-96/390-E (1996).

[36] `http://www-cdf.fnal.gov/upgrades/tdr/doc/cdfelev.ps`.

[37] `http://www-cdf.fnal.gov/upgrades/silicon/img6.gif`.

[38] `http://www-cdf.fnal.gov/events/detpic/COT_Install_2.jpg`.

[39] `http://www-cdf.fnal.gov/events/pic/decay_chart.gif`.

[40] C. S. Hill *et al.*, "Operational experience and performance of the CDFII silicon detector", Nucl. Instrum. Meth. A **530**, 1 (2004).

[41] A. Sill, "CDF Run II silicon tracking projects", Nucl. Instrum. Meth. A **447**, 1 (2000).

[42] A. A. Affolder *et al.*, "CDF Central Outer Tracker", Nucl. Instrum. Meth. A **526**, 249 (2004).

[43] D. Acosta *et al.*, "A time-of-flight detector in CDF-II", Nucl. Instrum. Meth. A **518**, 605 (2004).

[44] D. Acosta *et al.*, "A time-of-flight detector in CDF-II", Nucl. Instrum. Meth. A **518**, 605 (2004).

[45] Ref. [31], Figure 3.9.

[46] S. Kuhlmann *et al.*, "The CDF calorimeter upgrade for Run IIb", Nucl. Instrum. Meth. A **518**, 39 (2004).

[47] A. Artikov *et al.*, "Design and construction of new central and forward muon counters for CDF II", Nucl. Instrum. Meth. A **538**, 358 (2005).

[48] H. Frisch *et al.*, "Conceptual Design of a Deadtimeless Trigger for the CDF Trigger Upgrade", CDF/DOC/TRIGGER/CDFR/2038 (1994).

[49] E. J. Thomson et al., "Online track processor for the CDF upgrade", IEEE Trans. Nucl. Sci., 49:1063-1070 (2002).

[50] B. Ashmanskas et al., "The CDF Silicon Vertex Trigger", Nucl. Instrum. Methods A, **518**, 532 (2004).

[51] `http://www-cdf.fnal.gov/upgrades/tdr/doc/electronics/cdf_dataflow.eps`.

[52] D. Acosta *et al.* (CDF Collaboration), "Measurement of the J/ψ meson and b-hadron production cross sections in $p\overline{p}$ collisions at $\sqrt{s} = 1960$ GeV", Phys. Rev. D **71**, 032001 (2005).

[53] C. Paus, "MC Generators: BGENERATOR", `http://www-cdf.fnal.gov/cdfsim/generators/bgen.html`.

[54] D. J. Lange, "The EvtGen particle decay simulation package", Nucl. Instrum. Methods A **462**, 152 (2001).

[55] R. Brun *et al.*, CERN Report No. CERN-DD-78-2-REV (unpublished).

[56] M. Feindt and U. Kerzel, "The NeuroBayes neural network package", Nucl. Instrum. Methods A, **559**, 190, 2006.

[57] M. Pivk and F. R. Le Diberder, "sPlot: A statistical tool to unfold data distributions", Nucl. Instrum. Methods A, **55**, 356, 2005.

[58] "Dalitz plot analysis formalism". Part of the online version of [2].

[59] R. V. Hogg and A. T. Craig, "Introduction to Mathematical Statistics", 4th edition, New York: Macmillan, (1978). See Section 3.3.

[60] H. Albrecht *et al.* (ARGUS Collaboration), "Search for hadronic $b \to u$ decays", Phys. Lett. B **241**, 278 (1990).

[61] W. Verkerke and D. Kirkby, "The RooFit Toolkit for Data Modeling", Proceedings from the Computing in High Energy and Nuclear Physics 2003 conference, arXiv:physics/0306116, 2003.

[62] F. James *et al.* "MINUIT, Function Minimization and Error Analysis CERN Program Library".

[63] R. Brun and F. Rademakers, "ROOT - An Object Oriented Data Analysis Framework", Nucl. Instr. and Meth. A, **389**, 81 (1997).

Danksagung

Ich bedanke mich herzlich bei Prof. Dr. Michael Feindt für die Möglichkeit in seiner Arbeitsgruppe zu promovieren und für viele lehrreiche Diskussionen.

Ich danke Prof. Dr. Thomas Müller für die Übernahme des Korreferats.

Bei Priv.-Doz. Dr. Thomas Kuhr und Dr. Martin Heck bedanke ich mich für die sehr gute Betreuung und Unterstützung bei meiner Promotion und beim Publizieren der Analyse.

Für das Lektorat dieser Arbeit danke ich Dr. Martin Heck, Dr. Pablo Goldenzweig, Priv.-Doz. Dr. Thomas Kuhr, Matthias Huschle, Bastian Kronenbitter, Manuel Heider, Michael Ziegler, Johannes Grygier und Moritz Gelb.

Für die sehr gute und kollegiale Atmosphäre und für zahlreiche technische Hilfestellungen danke ich allen, die mit mir das Büro 9-2 geteilt haben, den Mitgliedern meiner Arbeitsgruppe und dem ganzen EKP. Besonders hervorzuheben sind das großartige Engagement des Admin-Teams und die organisatorische Unterstützung durch Frau Bräunling.

Für die Finanzierung dieser Arbeit und zahlreicher damit verbundener spannender Dienstreisen danke ich dem Graduiertenkolleg „Elementarteilchenphysik bei höchster Energie und höchster Präzision" der Deutschen Forschungsgemeinschaft.

Meiner Familie und dabei ganz besonders meiner Frau Olga danke ich sehr herzlich für die großartige Unterstützung und Motivation, die maßgeblich zum Erfolg dieser Promotion beigetragen hat.